Department of Physics and Astronomy
Heidelberg University

Master Thesis in Physics
submitted by

Johannes Reiter

born in Hall i.T. (Austria)

2023

Collective excitations in a mesoscopic Fermi system

This Master thesis has been carried out by
Johannes Reiter
at the
Physikalisches Institut Heidelberg
under the supervision of
Prof. Dr. Selim Jochim

Abstract

Understanding the emergence of collective behaviour in strongly-interacting mesoscopic systems has been a long-standing goal in nuclear, atomic and solid-state physics [1, 2, 3]. In our ultracold quantum gas experiment we investigate the excitation of a collective mode in a few-Fermion system with very low entropy by means of atom-loss spectroscopy.

Observing spectroscopic signatures of collective modes requires the precise control of the optical potential which can only be achieved through a novel aberration correction scheme. For this purpose, we developed and implemented a refined version of phase shift interferometry [4, 5] to measure wavefront aberrations directly on the atoms and compensate for them using a spatial light modulator. Using this technique we are able to reconstruct wavefront errors with a root-mean-square accuracy of $\sigma_{rms} \leq \lambda/13$ and a precision of $\sigma_{rms} \leq \lambda/25$.

The aberration reduced setup enables us to observe the radial quadrupole mode in a mesoscopic sample confined in an axisymmetric trap across the BEC-BCS crossover between $-0.5 < 1/(k_{\mathrm{F}}a) < 1.0$. Towards the macroscopic limit we find significant deviations from previous experimental studies [6] and theoretical models [7] indicating that a beyond mean-field description is required, which entails the breakdown of the hydrodynamic theory. Starting in the few-body limit and deterministically adding particles to our sample we witness the emergence of the quadrupole mode as a separation of a collective branch from the confinement dominated excitation spectrum. Finally, we demonstrate the coherence of the quadrupole mode by its excitation and subsequent controlled de-excitation enabling insight into the rich quantum dynamics associated with collective behaviour.

Zusammenfassung

Das Verständnis der Emergenz kollektiven Verhaltens in stark wechselwirkenden mesoskopischen Systemen ist ein langjähriges Bestreben in der Kern-, Atom- und Festkörperphysik [1, 2, 3]. In unserem ultrakalten Quantengasexperiment untersuchen wir die Anregung einer kollektiven Mode in einem Wenig-Fermionen-System mit geringer Entropie mittels der Atomverlustspektroskopie.

Die Beobachtung von spektroskopischen Signaturen kollektiver Moden erfordert die präzise Kontrolle des optischen Potenzials, die nur durch ein neuartiges Aberrationskorrekturverfahren erreicht werden kann. Zu diesem Zweck entwickelten und implementierten wir eine angepasste Version der Phasenverschiebungsinterferometrie [4, 5], um Wellenfrontfehler direkt mit Hilfe der Atome zu messen und sie mit einem räumlichen Lichtmodulator zu kompensieren. Diese Technik ermöglicht es uns, Wellenfrontfehler mit einer mittleren quadratischen Genauigkeit von $\sigma_{rms} \leq \lambda/13$ und Präzision von $\sigma_{rms} \leq \lambda/25$ zu rekonstruieren.

Der aberrationsreduzierte Aufbau ermöglicht es uns, die radiale Quadrupolmode in einem axisymmetrisch gefangenen, mesoskopischen System über den BEC-BCS-Übergang zwischen $-0.5 < 1/(k_{\mathrm{F}}a) < 1.0$ zu messen. In Richtung des makroskopischen Limes finden wir signifikante Abweichungen von früheren experimentellen Studien [6] und theoretischen Modellen [7], die eine Beschreibung jenseits der Molekularfeldnäherung erfordern und den Zusammenbruch der hydrodynamischen Theorie nach sich ziehen. Ausgehend vom Wenig-Teilchen Limes und durch deterministische Hinzufügung von Teilchen zu unserem System beobachten wir die Entstehung der Quadrupolmode als Abspaltung eines kollektiven Zweigs aus dem, von der Falle dominierten, Anregungsspektrum. Schlussendlich demonstrieren wir die Kohärenz der Quadrupolmode durch ihre Anregung und darauffolgende kontrollierte Abregung, welche einen Einblick in die vielseitige Quantendynamik im Zusammenhang mit kollektivem Verhalten ermöglicht.

Contents

1 Introduction

1.1 Collective behaviour

Collective behaviour is certainly one of the most fascinating phenomena in nature and in fact omnipresent in our everyday world. Flocks of birds swoop and swirl in unison in the skies [8, 9, 10], crowds of pedestrians tend to synchronise during road crossings [11] and the spontaneous ordering of spins leads to the cohesion of fridge magnets. In all of these examples, the driving factor and crucial ingredient for the appearance of ordering phenomena and the subsequent emergence of common patterns are interactions [12]. Humanity's quest to understand collective behaviour as a manifestation of interwoven interactions has led scientists of the past to reduce the complex dynamics to its fundamental building blocks.

In physics, the study of nature's fundamental building blocks gave birth to microscopic theories such as quantum mechanics and the standard model. While these microscopic theories have been applied successfully to describe peculiar quantum phenomena on the smallest scales and predict new particles [13], it was understood that collective behaviour is not simply the manifestation of the individual constituents' properties but rather emerges [14] with new effective quantities entailing a macroscopic description.

One prominent example of such a macroscopic theory is hydrodynamics or more generally the concept of modelling complex dynamics in the framework of flowing fluids. Hydrodynamic theory is applied across a wide range of disciplines, from the aerodynamic properties of aeroplanes [15], via the collision and merger of galaxies [16, 17, 18] to the description of nuclear matter [19]. In fact, the Schrödinger equation itself, which lies at the core of non-relativistic quantum mechanics, can be reformulated in a hydrodynamic framework re-establishing a connection between the macroscopic and microscopic pictures.

The discovery that liquid helium exhibits resistance-free flow if cooled to below its critical temperature is a prime example for a collective quantum behaviour, commonly referred to as superfluidity, that can be described in the framework of quantum hydrodynamics. Understanding its emergence as a consequence of a phase transition has triggered numerous studies and led to its universal observation in many systems other than liquid helium. For instance, atomic nuclei exhibit a spectrum reminiscent of a BCS superfluid [20] and also Bose-Einstein condensates can feature superfluid behaviour [21].

Collective excitations are another striking phenomenon that emerges in interacting systems and can be found across different branches of physics, both in superfluid and non-superfluid systems. Phonons in a crystal, plasmons in metals, or collective oscillations in nuclei [22] are all examples for collective modes, whose universal appearance in different interacting systems renders them an excellent probe for the study of collectiveness, regardless of the exact system under investigation. Observing the emergence and properties of a well-controlled collective mode constitutes the main goal of this thesis. While the observation of collective modes in condensed matter or nuclear systems may be comparatively straight-forward, their controlled manipulation is far from trivial in these systems due to imperfections or inaccessibility of degrees of freedom. Moreover, the exponential scaling of the Hilbert space with the system size ultimately limits current quantum theoretical predictions and makes it computationally intractable as the number of constituents is increased.

Fortunately, in the field of cold atoms significant experimental progress has been made in the realisation of complex quantum many-body systems that act as toy models for a variety

of phenomena.Ultracold quantum gas experiments close to absolute zero have proven to be a versatile platform [23] to study novel collective phenomena of quantum many-body systems such as spin ordering [24] or cooper pairing [25]. Their ability to freely tune the interactions across a wide range in combination with the precise control of the potential landscape and the Hamiltonian renders them excellent toy models to explore universal phenomena much to Richard Feynman's idea of quantum simulators [26]. Also collective modes have been investigated intensively in ultracold quantum gas experiments mainly in the context of elementary excitations of Bose-Einstein condensates [27, 28], where analogies can be drawn to respective excitations in atomic nuclei [29]. Hydrodynamic theories have been successfully applied to theoretically describe the experimental observations in a mean-field and perturbative approach [30]. However, experimental results in strongly-interacting Fermi gases [6, 31] have provoked the breakdown of this approach and motivated further investigation of the underlying principles, as well as the study of the emergence and disappearance of collectiveness.

1.2 Macroscopic, microscopic, mesoscopic

Collective behaviour is usually considered a macroscopic phenomenon, where the individual constituents' properties become irrelevant over the dominating dynamics of the entire system. Removing a water molecule from a glass of water will not alter its macroscopic quantities. But what if the glass of water only contained a few molecules? As absurd as the question may seem for a glass of water containing $\sim 10^{25}$ molecules, atomic nuclei only consist of comparatively few nucleons but are still commonly described in the framework of hydrodynamics. [19] Obviously, macroscopic quantities loose their validity in the microscopic limit of few particles, which are better described in a quantum mechanical single-particle picture with mutual interactions. However, collective phenomena emerge in the intermediate, *mesoscopic*, regime where the dynamics and wavelength is in the order of the system size and changing the chemical potential by adding or removing a particle might dramatically influence the system's behaviour. Consequently, the mesoscopic regime is characterised by a continuous competition of energy and length scales entailing favourable *shell* configurations found in the periodic table or nuclear shell model.

Our experiment bridges the gap between the different regimes by allowing us to prepare highly degenerate quantum systems containing as few as one up to a few hundred atoms. Strong inter-particle interactions open the possibility to overcome the single-particle energy gap and explore the influence of quantum confinement on collective behaviour. Furthermore, it permits the realisation of strongly correlated quantum states, which promise to host novel phenomena.

1.3 Outline

The second chapter establishes the fundamental techniques required to prepare few-particle quantum systems. Moreover, it is described how the Hamiltonian of the system can be manipulated by shaping the optical potential and tuning the interactions via a Feshbach resonance. The third chapter is dedicated to the reduction of experimental imperfections, mainly in the form of optical aberrations. Particularly, we present and employ a refined technique for the correction of optical aberrations, which alter the potential landscape and discuss its limitations. After reducing the aberrations we report the observation of the radial quadrupole mode and its emergence in a mesoscopic sample of ultracold ^{6}Li atoms in the fourth chapter and demonstrate the controlled manipulation of this collective mode. The fifth and last chapter in this thesis is dedicated to the discussion of the results and their classification in a broader context.

2 Experimental platform

2.1 Preparing ultracold atoms - from many to few

Quantum effects usually arise when the deBroglie wavelength $\lambda \sim T^{-1/2}$ becomes comparable to and eventually exceeds the inter-particle spacing $d \sim n^{-1/3}$ of a system with temperature T and density n. The observation and precise control of these delicate quantum systems in a regime comparable to condensed matter or nuclear systems at significantly higher densities and temperatures consequently requires the decoupling from its environment, which may otherwise alter the internal state of the ensemble. Trapped neutral atoms have proven to be a superb platform as their interaction with stray electric and magnetic fields are comparatively small allowing for long coherence times [32]. Avoiding undesired interactions with the background gas raises the need for an ultra-high vacuum setup, which ultimately imposes an inevitable condition on the required temperatures given by the deBroglie wavelength. Due to the diluteness of the sample, the temperatures needed to immerse into the quantum regime are in fact many orders of magnitude smaller than in their much denser condensed matter counterparts. Reaching these nano Kelvin temperatures has only been possible due to the introduction of laser and evaporative cooling, which marked a necessary milestone to realise replicate systems with properties comparable to condensed matter systems.

In our experiment we use the lightest alkali species, Lithium-6. Its fermionic interparticle exchange statistics and light mass allows for a comparison with electrons under the right conditions and the pairing of constituents renders it capable of forming quasi-bosonic ensembles as discussed in section 2.2.2. Moreover, it offers a simple hydrogen-like electronic spectrum (see figure A.1) which facilitates the pathway to quantum degeneracy via laser cooling. At magnetic fields of several hundred Gauss, its electronic and nuclear spin decouple due to its small hyperfine interaction allowing for stable hyperfine mixtures. Lithium's properties, which are described in more detail in reference [33] and addressed in section 2.2.2, hence makes it a well-suited species for studying collective behaviour in quantum systems.

In our setup we utilise an all optical trapping scheme which allows the magnetic offset field to be used as a tool to freely tune the interactions between atoms as described in section 2.2.2. The combination of optical traps for trapping and cooling, magnetic fields for the control of internal degrees and a ultra-high vacuum setup ($p \sim 10^{-11}$mbar) constitutes the main experimental setup shown in figure 2.1.

2.1.1 Laser cooling

The Lithium-6 atoms evaporate from an oven when heated to a temperature 638K creating a vapour of atoms ten orders of magnitude hotter than what is required for quantum degeneracy.

Due to the atoms' high thermal velocities, the atomic resonance frequency is Doppler shifted with respect to the bare atomic resonance. A magnetic gradient field generated by the Zeeman slower coils tunes them into resonance and photons from the counter-propagating Zeeman beam can be absorbed transferring the momentum $\Delta p = h/\lambda$ carried by each absorbed photon. Since spontaneous emission is isotropic the average momentum transfer from the re-emission vanishes and the net transfer only occurs opposite to the propagation direction of the atomic beam [34]. The decrease in average momentum results

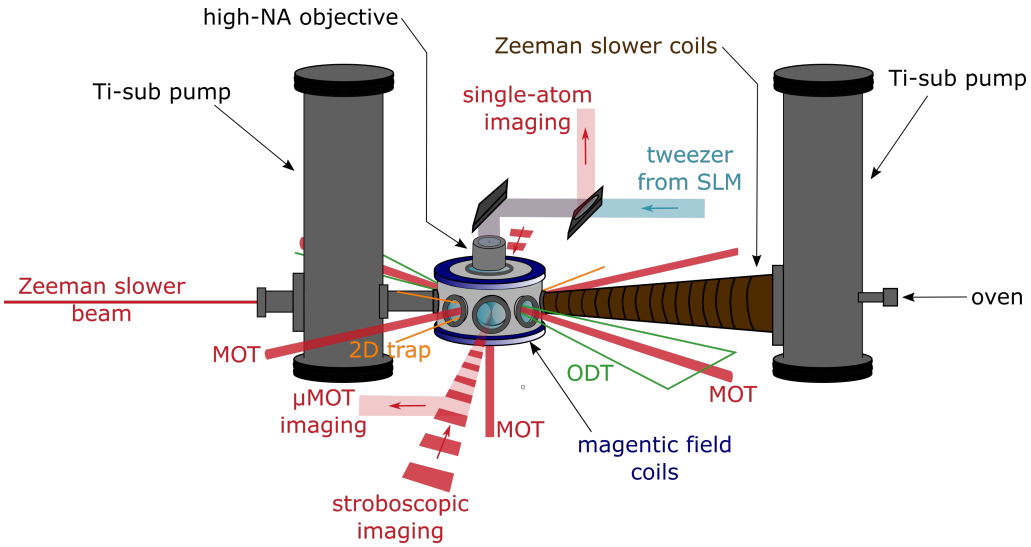

Figure 2.1: **Experimental setup** A combination of Ti sublimators and ion pumps ensures an ultra-high vacuum environment of $p \sim 10^{-11}$mbar. Lithium-6 atoms evaporating from the oven are slowed in the Zeeman slower and captured and cooled in the 3D-MOT (2.1.1). After establishing a degenerate Fermi gas using the optical dipole trap (ODT) (2.1.2), atoms are prepared in an optical tweezer (2.1.3) where the experiments are performed using tailor-made optical potentials (2.2.1). The magnetic field coils are used to tune the inter-particle interactions via a Feshbach resonance (2.2.2). Atoms can either be detected via a single atom imaging technique (2.3.2) through the high-NA objective or counted in the μMOT (2.3.1).

in reduced kinetic energy. The smaller velocity of the gas allows a sufficiently large fraction of the atoms to be captured in a magneto-optical trap (MOT) inside the main experimental chamber.

Three mutually-orthogonal beams, which are retro-reflected at opposite sites of the experimental chamber and have opposite circular polarisation form an optical molasses. This configuration generates a velocity dependent radiation pressure in intersection region of the beams. An additional magnetic gradient field generated by two magnetic field coils in anti-Helmholtz configuration is applied and introduces a position dependent restoring force due to the Zeeman shift experienced by the atoms. In combination they allow the atomic vapour to be both cooled by a decrease of net momentum and trapped in the intersection region.

Both the Zeeman and MOT beams are derived from the same tapered amplifier laser[1] which is beat-offset locked to the Lithium D_2 line at $\lambda \approx 671$nm via modulation transfer spectroscopy. Since the optical transitions in ^{6}Li are not closed and the hyperfine splitting of 228MHz of the $F = 3/2$ and $F = 1/2$ ground states is much larger than the linewidth of $\Gamma \approx 2\pi \times 5.9$MHz [33], atoms can decay into the dark ground state, which raises the necessity for a repumper laser in all beams. The repumper transition couples the $F = 1/2$ dark state back to the cooling transition between the $2^3S_{3/2}$ (F=3/2) and the $2^2P_{3/2}$ excited state and ensures an effective cooling of the atomic cloud down to the Doppler limit, which imposes the lower limit of this technique caused by the random walk due to the spontaneous emission. Since the Doppler limit at $T_{\text{Doppler}} = \hbar\Gamma/(2k_B) = 141\mu$K is more than two orders of magnitude larger than the temperatures required to reach quantum degeneracy aa additional cooling technique is required.

[1] Toptica TA100 tapered amplifier at 671nm

2.1.2 Evaporative cooling

After loading the MOT for two seconds the *repumper* is switched off before the *cooler*, thus transferring the 10^7 atoms that have been trapped into the dark $F = 1/2$ ground state. Afterwards the magnetic gradient is increased which compresses the MOT and atoms are transferred into the crossed optical dipole trap (ODT) formed by a 100W laser beam[2] operated at 1064nm in a non-interfering bow-tie configuration. The far red-detuned laser beams generate a potential U given by the AC stark shift

$$U(\mathbf{r}) = -\frac{\hbar\omega_R^2(\mathbf{r})}{4}\left(\frac{1}{\omega_0-\omega_L}+\frac{1}{\omega_0+\omega_L}\right) = -\frac{\hbar\Gamma^2}{8}\frac{I(\mathbf{r})}{I_{sat}}\left(\frac{1}{\omega_0-\omega_L}+\frac{1}{\omega_0+\omega_L}\right) \quad (2.1)$$

where ω_0 is the atomic resonance frequency, ω_L the frequency of the laser light and ω_R denotes the position dependent Rabi frequency characterising the strength of the atom-field coupling [32]. In the right equation we expressed the potential in terms of the intensity $I(\mathbf{r})$ by introducing the saturation intensity $I_{sat} = \hbar\omega_0^3\Gamma/(12\pi c^2)$. In the case of red detuning ($\omega_L < \omega_0$) atoms will be trapped in the intensity maximum at the centre of the experimental chamber, where both arms of the crossed ODT overlap.

Ramping on the magnetic offset field splits the hyperfine states yielding a spin-imbalanced mixture of states $|1\rangle$ and $|2\rangle$. After spin balance is achieved by a radio frequency pulse, state $|2\rangle$ is adiabatically transferred into state $|3\rangle$ in a Landau-Zener passage. To cool the remaining 10^6 atoms the optical potential is subsequently reduced allowing the highest energetic constituents to escape the trap by means of evaporation. The removal of atoms is aided by applying a magnetic field gradient of 40G/cm. In the presence of the magnetic offset field of 740G the spin-up and spin-down atoms interact via collisions and the sample consequently re-thermalises at a lower temperature. After the 200ms long evaporation ramp the sample reaches a final temperature, which is slightly above the Fermi temperature T_F and hence the sample is not yet in the degenerate regime. The remaining 10^5 atoms in the balanced $|1\rangle - |3\rangle$ mixture form a reservoir for all further experiments presented in this thesis.

2.1.3 Deterministic preparation of number states

Studying the fundamental building blocks of quantum many-body systems and the emergence of collective behaviour in the mesocopic limit requires a high degree of control of the individual constituents' quantum states. To deterministically prepare few-particle pure quantum number states with high fidelity, we exploit a technique developed in our group [35] to locally minimize the entropy and deterministically spill to a desired fermionic ground state.

To achieve this we superimpose the ODT with a tighly focused far-detuned Gaussian beam generating an optical tweezer as schematically depicted in figure 2.2a. With a wavelength of 1064nm the tweezer acts as a far-detuned optical dipole trap but with a much stronger confinement than the crossed ODT. This locally increases the chemical potential without altering the temperature of the entire sample resulting in a high density region. Due to the fermionic nature of ^{6}Li, the atoms occupy the available states of the Gaussian potential by each a spin-up ($|1\rangle$)[3] and a spin-down ($|3\rangle$) atom achieving close to unity filling of the lowest lying states in Gaussian potential. To avoid confusion we will denote the number of atoms as $N_\uparrow + N_\downarrow$ to account for the spin degree of freedom in the notation. After the ODT is switched off, the tweezer is fully loaded with approximately $\sim 10^3$ atoms with respective densities of 10^{15} atoms/cm^3. The high density in the tweezer and correspondingly high collision rates allow a second, much faster evaporative cooling

[2] The laser light is derived from a 200W Yb-doped fibre amplifier YLR-200-LP-WC from IPG Photonics.
[3] without loss of generality

step in the tweezer by ramping down the optical trap depth in 40ms and thereby evaporating the hottest atoms from the sample further increasing the phase space density. The roughly 150 atoms per spin state after evaporation in the tweezer equilibrate far in the degenerate regime where $T \ll T_F$. As the number of atoms is reduced the temperature as a macroscopic quantity looses its validity and may be replaced by the particle number fluctuations ΔN and corresponding entropy per particle S/N. While in microscopic systems the Von Neumann entropy $S = -k_B tr(\rho \ln \rho)$ can be calculated straight from the density matrix ρ, the latter is hard to extract in systems of larger size. [36] Since the fluctuations of the atom number $\Delta N \approx 5\%$ of the ~ 150 atom sample is comparable with the microscopic system, the entropy can still be extrapolated from the small system yielding $S/N \approx 0.1 k_B$. [37] The low-entropy sample forms the starting point for the deterministic preparation (Figure 2.2b) .

For low-lying states, the Gaussian potential is generally well approximated by a harmonic oscillator potential with a trapping frequency ω_r in the radial and ω_z in the axial direction. The Gaussian beam shape entails an aspect ratio of $\omega_r/\omega_z \approx 6$ rendering the situation quasi one-dimensional until the first radial level is filled for 6+6 atoms.

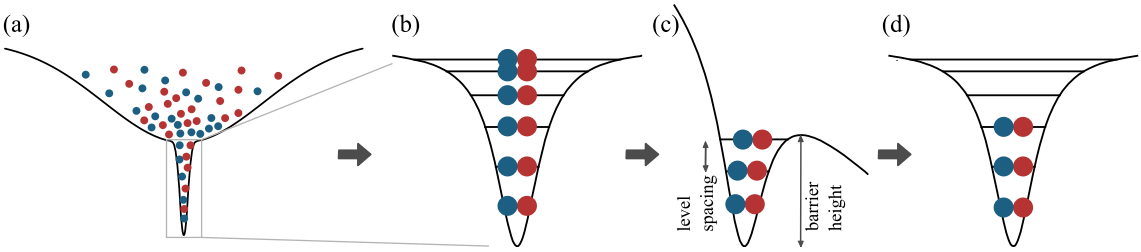

Figure 2.2: **Deterministic preparation scheme** (a) The crossed ODT acts as a reservoir for the superimposed tweezer locally enhancing the chemical potential. (b) Fully filled tweezer potential with one spin-up and one spin-down atom per level represented by the red and blue circles. (c) Spilling of the tweezer by simultaneously applying an axial gradient and lowering the spill depth. (d) Fermionic ground state configuration in the Gaussian potential after the tweezer has been restored. The figure is adapted from [38].

In order to prepare the desired number of atoms we apply an axial magnetic field gradient of 25G/cm and simultaneously ramp down the optical power (Fig. 2.2c). Previously bound states become unbound and are spilled out of the trap. Due to the tightness of the potential, the spacing between quantum states becomes favourably large and allows us to precisely tune the Fermi energy between two levels solely by changing the power of the Gaussian beam. After a holding time of 40ms at the desired spill depth corresponding to a well-defined atom number, the tweezer is ramped back up to a radial confinement of several tens of kilohertz (Fig. 2.2d). This spilling procedure allows us to prepare the fermionic ground state in a Gaussian potential with a well defined number of atoms which is forming the starting point for our experiments.

For small atom numbers the discrete filling of energy levels of the potential can be directly observed manifesting itself in the characteristic step-like behaviour shown in figure 2.3. As the spill depth is reduced the potential exhibits fewer bound states. Filled shell configurations are realised for even number of atoms resembling the spectrum of the one-dimensional harmonic oscillator which manifest themselves in a high detection probability. Odd atom numbers are strongly suppressed due to the preparation of closed shell systems. For filled levels the variance of the atom number decreases, whereas it is greater between two steps. The imaging technique used to count the number of atoms is described in more detail in section 2.3.1.

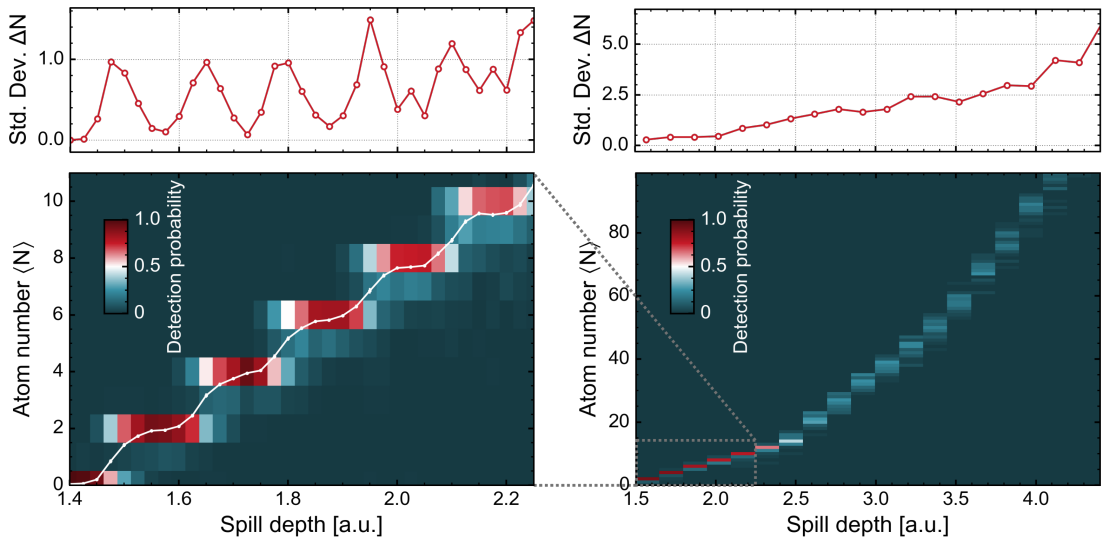

Figure 2.3: **Deterministic preparation of few Fermions** The left plot shows the full counting statistics for various spill depths and the interpolated mean atom number $\langle N \rangle$ (white curve). The standard deviation is minimised for closed shell configurations. The characteristic step-like behaviour emerges as the optical trap depth is increased, which effectively increases the number of bound states that can each be occupied by a spin-up and spin-down atom. The maximum preparation fidelity of 98(1)% is achieved for the ground state of $1 + 1$ atoms and decreases with higher atom numbers which is reflected in the increasing standard deviation. The right plot shows the full counting statistics for higher atom numbers.

Using this spilling technique we achieve ground state preparation fidelities of $(98 \pm 1)\%$ for 1+1 atoms, subsequently decreasing with higher fillings. For larger atom numbers the density of states increases due to the additional radial levels and reduced level spacing caused by the Gaussian as opposed to harmonic potential making the deterministic preparation increasingly difficult. However the technique still permits preparations of larger low entropy samples with for example $N = 50 \pm 2$ atoms, where the standard deviation is well below the Poissonian expectation $\sqrt{N} = 7$ (compare right plot in figure 2.3).

2.2 Engineering the Hamiltonian

2.2.1 Shaping optical potentials

The ability to shape the optical potential landscape is a key ingredient to realize the Hamiltonian of interest under which the deterministically prepared system is evolving. In our experiment we use a spatial light modulator[4] (SLM) to imprint a desired phase pattern on the trapping beam which dictates both shape and phase of the created potential experienced by the atoms inside the experimental chamber. Figure 2.4 shows the optical setup used to generate the trapping potential. The trapping light is generated by a 1064nm single-mode laser[5] and distributed to two individual beams, *Beam 1* and *Beam 2*, whose frequencies and powers can be tuned individually by two acousto-optical modulators (AOM). Both Gaussian beams are individually power-stabilized on a 400kHz PID

[4] Hamamatsu 10468-03 SLM
[5] Azur Light Systems ALS-IR-120

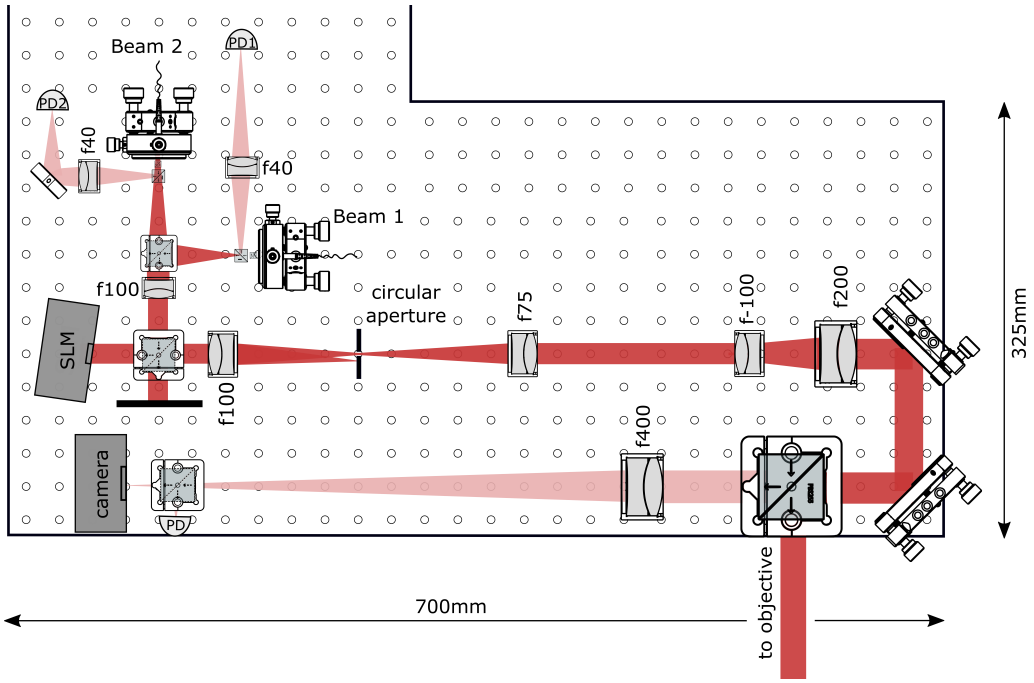

Figure 2.4: **Optical setup for freely engineering the potential landscape** We use a spatial light modulator (SLM) to imprint a phase pattern on the two 1064nm trapping beams shown in red. The dual-beam configuration in combination with the ability to tune the relative frequency and phase allows us to create dynamic optical trapping potentials through interference of the beams. The light field can be monitored on the camera which is also used for aberration detection (see section 3).

loop using two separate photodiodes, PD1 and PD2 respectively. The beams are combined on a non-polarising 50:50 beam splitter and collimated by the 100mm lens before they are split by another non-polarising 50:50 beam splitter. Half of the light is transmitted and dumped on the beam dump and hence lost, the other half is reflected and hits the SLM.

A phase-only SLM works by imprinting a phase field $\phi(x, y)$ on the incident Laguerre-Gauss LG_0^0 beam with an amplitude u_{in}, such that the reflected light field can be expressed as

$$u_{\text{out}}(x, y) = e^{i\phi(x,y)} u_{\text{in}}(x, y). \tag{2.2}$$

The used spatial light modulator consists of 792×600 pixels, whose refractive indices can be changed individually, which locally modulates the phase on the incident patch of light with a depth of 8 bits. Through an adroit choice of the individual pixels' phases, arbitrary light fields can be created by subsequent Fourier transformation. After the SLM the light field of a circular aperture with radius R is given by

$$u(r, \phi) = \sqrt{I_0}\Theta(R - r)e^{-r^2/w_0^2} e^{il\phi} \tag{2.3}$$

where I_0 is the beam's intensity. The introduction of phase windings give rise to beams with higher orbital angular momenta l. For a second-order phase vortex with $e^{2i\phi}$, the resulting light field is well approximated by a LG_0^2 beam.

Another important application is the generation of multiple beams from a single beam by displaying the phase pattern of the form

$$\phi(x, y) = \arg\left(e^{i\phi_1(x,y)} + e^{i\phi_2(x,y)}\right). \tag{2.4}$$

The incident light field transforms under equation 2.2 yielding

$$u_{out}(x,y) = \frac{1}{2} u_{in}(x,y) \frac{e^{i\phi_1(x,y)} + e^{i\phi_2(x,y)}}{1 + \cos(\phi_1 - \phi_2)}. \tag{2.5}$$

Indeed the phase pattern 2.4 leads to two outgoing beams, which we will refer to as beam A and beam B to differentiate them from the incident beams 1 and 2.

When the relative gradient Δg between beams A and B is matched to the relative incident angle θ between the incident beams 1 and 2 such that the condition $\theta = \lambda \Delta g$ is fulfilled, two of the four beams overlap. This is particularly useful since the overlapping beams interfere due to their common coherent source, providing an even greater variety of realisable potentials which can be changed dynamically using the AOMs.

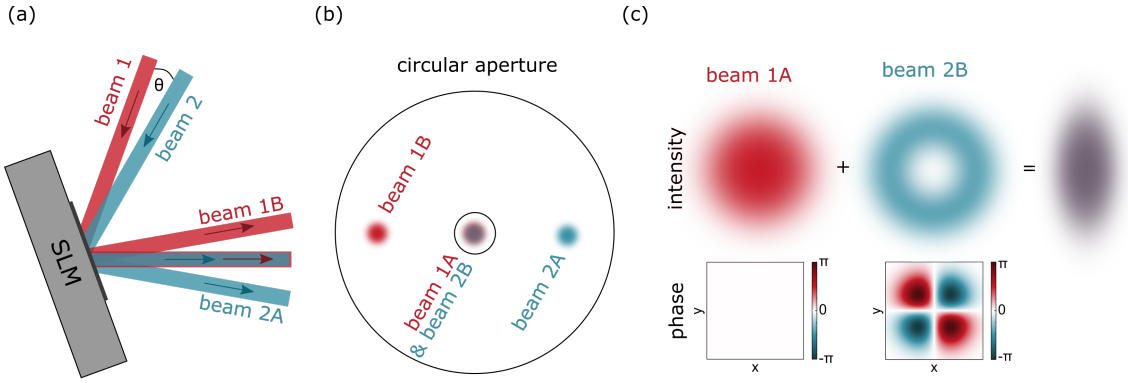

Figure 2.5: **Multiple beam generation with the SLM** The relative gradient Δg between beams A and B is matched to the incident angle θ such that two beams overlap. Observe that the beam angles are not to scale and real angles are much smaller. (b) The overlapping beams (1A & 2B) which are used to generate the trapping potential are spatially filtered on a circular aperture whereas the others are blocked. (c) The interference of a Gaussian LG_0^0 and Laguerre-Gaussian LG_0^2 beam yields an elliptical beam shape in the Fourier plane.

Only the overlapping beam A of beam 1 (1A) and beam B of beam 2 (2B) are used for the generation of optical potentials projected on the atoms. In addition to the two beams [6] which are not used, approximately 3% of the incident light is directly reflected from the space between the pixels which gives rise to a zeroth order peak. Additionally, the SLM also generates higher diffraction orders which cannot be used for our purpose. Both the unused beams as well as the zeroth and higher order order peak are spatially filtered out on a pupil aperture after the 100mm lens, which performs the required Fourier transform for spatial separation. The global gradient is chosen such that the overlapping beams A and B are well separated from the zeroth order peak, which due to its source cannot be altered by any gradient. Higher order beams and other parasitic effects due to the finite pixel number and phase resolution, as well as its consequences in the generation of phase patterns is discussed in detail in [39]. While the circular aperture in the first Fourier plane of the SLM removes unwanted beams, the two co-linearly aligned beams can propagate further along the optical beam path and are expanded in the Galilean telescope to match the aperture of the objective. A polarising beam splitter is used to direct the collimated beams to the objective and combine it with another setup not depicted in figure 2.4. Our custom objective with a numerical aperture of $NA = 0.55$ focuses the light to the position of the atoms in the experimental chamber and thereby performs the required Fourier transform to translate the shaped wavefront into the desired intensity profile.

[6] beam B of beam 1 (1B) and beam A of beam 2 (2A) (compare Fig. 2.5)

The small fraction of light which passes through the polarizing beam splitter is focused on a camera [7] in the Fourier plane using a 400mm lens. This allows us to monitor the projected light field on the atoms, take snapshots at well-defined times during the experimental sequence and use it for aberration determination as explained in the course of section 3. The same light can furthermore be used to stabilise the power of combined beams using a photodiode.

2.2.2 Tuning interactions via a Feshbach resonance

While the engineering of optical potentials renders the trivial quantum system of particles in a Gaussian trap into a more interesting problem of an arbitrary potential, interactions open up physics beyond a single particle picture. The mediation of forces between constituents and subsequent emergence of collective behaviour are omnipresent in our world, from the formation of solid matter to the generation of coherent laser beams. Interactions makes quantum mechanics interesting and transforms the well-understood single-particle scenario into a regime accompanied by the rich dynamics of a quantum many-body system.

Neutral atomic gases, such as ^{6}Li in our experiment, only[8] interact via the short-range Van-der-Waals interaction scaling with distance as $\sim r^{-6}$. Given the diluteness of the gas present in our experiment, the interaction range r_0 is much smaller than the inter-particle spacing $n^{-1/3}$ which simplifies the problem to that of a binary collision [32]. In the centre-of-mass system with distance $\mathbf{r} = \mathbf{r}_1 - \mathbf{r}_2$ between constituents and effective mass $\mu = m_1 m_2/(m_1 + m_2)$ the scattering problem reads

$$\left(\frac{\hbar^2}{2\mu}\nabla_r^2 + V_{int}(\mathbf{r})\right)\Psi_k(\mathbf{r}) = E_k\Psi_k(\mathbf{r}) \tag{2.6}$$

Beyond the short interaction range r_0 the interaction potential vanishes and the solution reduces to that of a free particle with energy $E = \frac{\hbar^2 k^2}{2\mu}$. For distances smaller than the interaction range, the interaction potential contributes significantly and the spherical symmetry of the Van-der-Waals interaction $V(\mathbf{r}) = V(r)$ allows the solution to be expressed as

$$\Psi_k(\mathbf{r}) = \Psi_{in}(\mathbf{r}) + \Psi_{out}(\mathbf{r}) \underset{r\to\infty}{\simeq} e^{ikz} + f(k,\theta)\frac{e^{ikr}}{r} \tag{2.7}$$

with θ being the angle between between the ingoing wave $\Psi_{in}(\mathbf{r})$ and outgoing wave $\Psi_{out}(\mathbf{r})$. Since the Van-der-Waals interaction is an elastic process only the phase contained in the scattering amplitude $f(k,\theta)$ of the outgoing wave $\Psi_{out}(\mathbf{r})$ will change whereas the modulus of the momentum is conserved. Using the azimuthal symmetry the solution can be expanded in partial waves

$$\Psi_k(r,\theta) = \sum_{l=0}^{\infty} A_l P_l(\cos\theta) R_{kl}(r) \tag{2.8}$$

with expansion coefficients A_l, Legendre polynomials $P_l(\cos\theta)$ and a radial part $R_{kl}(r)$ solving the radial equation:

$$\left[\frac{\partial^2}{\partial r^2} + \frac{2}{r}\frac{\partial}{\partial r} + k^2 - \frac{l(l+1)}{r^2} - \frac{2m}{\hbar^2}V_{int}(r)\right]R_{kl}(r) = 0. \tag{2.9}$$

The radial equation contains a rotational barrier term $V_b = \frac{l(l+1)}{r^2}$ which is the quantum analogue of a classical angular momentum blockade. In the low energy limit where $k \to 0$,

[7] Teledyne FLIR Chameleon 3

[8] In other species such as e.g. Erbium long-range dipolar interactions may also contribute or even dominate.

which is well satisfied for cold dilute gases, the wavefunction decays exponentially for $r < r_b = \frac{l(l+1)}{k^2}$. Consequently, for the short range Van-der-Waals interaction, where the interaction radius is small $r < r_b$, only the $l = 0$ term survives. This justifies neglecting higher order contributions and considering only isotropic s-wave scattering in ultracold atomic samples.

At large distances ($r \to \infty$)

$$R_{kl}(r) \simeq \frac{1}{kr} \sin(kr - l\frac{\pi}{2} + \delta_l) \tag{2.10}$$

satisfies the radial wave equation 2.9 and the phase shift δ dictates the qualitative scattering behaviour. Depending on the sign of δ the interaction can be either attractive ($\delta > 0$), effectively pulling the partial wave closer to the centre, or repulsive ($\delta < 0$), by effectively pushing it away from the centre.

Omitting the details of the derivation, the scattering amplitude $f(k, \theta)$ can be expanded similarly to the solution Ψ_k. Neglecting higher order terms in the angular momentum ($l > 0$) one finds [32]

$$f(k, \theta) = \frac{1}{2ik} \left(e^{i2\delta_0} - 1 \right) = \frac{1}{k \cot(\delta_0(k)) - ik} \tag{2.11}$$

for the scattering amplitude. At modest densities where the assumption of binary collisions holds and the interparticle spacing is much larger than the range of the interatomic potential, the interaction is consequently characterised by a single parameter, the s-wave scattering length

$$a = \lim_{k \to 0} -\frac{\tan \delta_0(k)}{k}. \tag{2.12}$$

Typical scattering lengths of alkali species lie in the order of the Van-der-Waals range of around 100 Bohr radii, which translates to very small interaction strengths in dilute gases[9], too weak for studying strong interaction phenomena of quantum many-body systems. Another problem arises when taking the indistinguishability of fermionic ^{6}Li particles into account. At low temperatures s-wave interactions are Pauli-blocked as fermions cannot occupy the same quantum state and the total wave function must be antisymmetric under particle exchange. To circumvent this peculiarity of quantum mechanics, we use a balanced two component spin-mixture of the lowest and third lowest hyperfine states of ^{6}Li which we denote with $|1\rangle$ and $|3\rangle$ respectively (compare figure A.1).

Fortunately, the existence of scattering resonances provides a unique tool to increase the interaction among constituents by a multiple. A Feshbach resonance occurs when the initial scattering energy is equal to that of an energetically forbidden bound state (compare figure 2.6 (a) and (b)). [32] A small coupling between the energetically allowed open channel and forbidden closed channel strongly shifts the phase and thereby resonantly couples the atomic Hilbert space to a vibrationally highly-excited molecular state. Because of the different magnetic moments of the two spin components the energy difference between the incoming and the bound state can be tuned into resonance by a magnetic offset field providing the required coupling. While in bosonic samples collisions lead to fast vibrational relaxations, the interplay between the Pauli exclusion principle and large ratio between initial and final size of Feshbach molecules strongly suppresses the relaxation for fermions [32]. The result is a Hilbert space containing the usual atomic levels plus a single

[9] For interparticle spacings of $n^{-1/3} \approx 10^4 a_0$ the Fermi momentum is $|k_F| = (2500 a_0)^{-1}$ yielding interaction stengths of only $|k_F|a \approx 0.03$ [32]

additional molecular level. When tuning the magnetic field B the scattering length obeys the phenomenological equation [40]

$$a(B) = a_{bg}\left(1 - \frac{\Delta}{B - B_0}\right) \tag{2.13}$$

where a_{bg} denotes the background scattering length of the open channel, B_0 the position of the resonance and Δ the width of the resonance.

The broad s-wave Feshbach resonance in the ^{6}Li $|1\rangle$-$|3\rangle$ mixture shown in figure 2.6 allows the free tunability of the interaction over several orders of magnitude. It grants access to both attractive and repulsive interactions, characterised by negative and positive scattering lengths respectively, as well as a convenient zero crossing at 568G, which allows for comparative measurements of a non-interacting system.

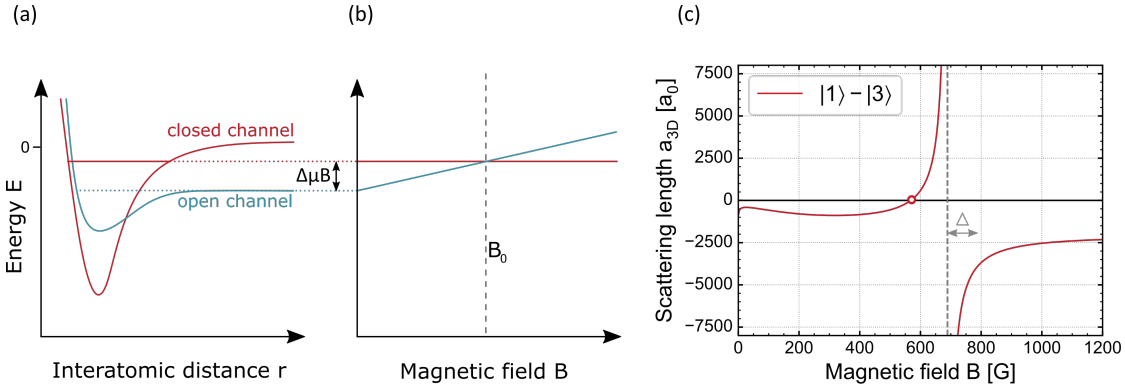

Figure 2.6: **Feshbach resonance** (a) and (b) A Feshbach resonance occurs by tuning the initially open channel scattering state into resonance with a closed channel bound state. (c) In ^{6}Li the broad s-wave Feshbach resonance for a mixture of the lowest and third lowest hyperfine states ($|1\rangle$,$|3\rangle$) at $B_0 = 689.68$G (dashed grey line) allows the scattering length a_{3D}, and hence the interaction to be tuned over several orders of magnitude across the entire BEC-BCS crossover. Moreover the zero crossing at 568.07G (red dot) enables the realisation of a system without interactions ($a_{3D} = 0$) allowing for comparative studies. The definition and in particular sign of the energy follows the convention of reference [40].

In the experiment we achieve the tuning of the scattering length by generating a magnetic offset field using a pair of coils positioned above and below the vacuum chamber. The current flowing through the coils and creating the magnetic field is actively stabilized on a 400kHz PID loop to achieve a relative magnetic field stability of 5×10^{-4}. The precise magnitude of the field at the position of the atoms is impossible to measure in our setup using standard magnetic field probes, hence we rely on a calibration derived from RF spectroscopy on the atoms. Although the accuracy of this measurement is as little as 80mG [41] temperature fluctuations of the coils and stray magnetic fields may alter this calibration.

Quantum many-body theory of ultracold atoms

We now want to expand the description from the microscopic two-particle scattering problem to the macroscopic phenomena that become accessible by the free tunability of the interaction.

Two weakly and attractively interacting fermions can only form a pair on the Fermi surface as Pauli exclusion principle prevents two fermions to scatter into an already occupied

momentum state of the filled non-interacting Fermi sea. For small momenta, the final scattering states are consequently confined to a quasi two-dimensional shell with a constant density of states above the Fermi surface which hosts a bound state[10] for arbitrarily weak interactions. If interactions within the Fermi sea are considered the existence of the bound state entails the realisation of a macroscopic ground state that will be given by a coherent superposition of pairs.

Due to the s-wave scattering nature of ultracold quantum gases the two-body interaction potential $V(\mathbf{r}-\mathbf{r}')$ can be replaced by an effective contact-like interaction

$$V(\mathbf{r}-\mathbf{r}') = g\delta(\mathbf{r}-\mathbf{r}') \tag{2.14}$$

where the coupling constant is directly related to the s-wave scattering length a and mass m via

$$g = \frac{4\pi\hbar^2 a}{m}. \tag{2.15}$$

In the presence of contact-like interactions the problem can effectively be described by the simplified many-body grand-canonical Hamiltonian[42]

$$\hat{H} = \sum_{\mathbf{k},\sigma} \epsilon_{\mathbf{k}} \hat{c}^\dagger_{\mathbf{k},\sigma}\hat{c}_{\mathbf{k},\sigma} - \frac{g}{V}\sum_{\mathbf{k},\mathbf{k}',\mathbf{q}} \hat{c}^\dagger_{\mathbf{k}+\frac{\mathbf{q}}{2}\uparrow}\hat{c}^\dagger_{-\mathbf{k}+\frac{\mathbf{q}}{2}\downarrow}\hat{c}_{\mathbf{k}'+\frac{\mathbf{q}}{2}\downarrow}\hat{c}_{-\mathbf{k}'+\frac{\mathbf{q}}{2}\uparrow} \tag{2.16}$$

with an energy dispersion relation $\epsilon_{\mathbf{k}} = \frac{\hbar^2\mathbf{k}^2}{2m} - \mu$ that relates the single particle energy to the chemical potential μ. The interaction term includes the single-particle operators, $\hat{c}^\dagger_{k\sigma}$ and $\hat{c}_{k\sigma}$, that create and annihilate particles and holes, whose momenta are only considered in a narrow shell above the Fermi surface and is normalised to the volume V. The state with $\mathbf{q} = 0$ has the highest density of final scattering states and consequently minimises the binding energy. As opposed to finite momentum pairing ($\mathbf{q} \neq 0$) where final scattering states are confined to a circle around the Fermi sphere, zero-momentum pairing ($\mathbf{q} = 0$) allows final states on the entire Fermi surface[11]. Neglecting interactions of pairs at finite momenta $\mathbf{q} = 0$ yields the celebrated BCS-Hamiltonian

$$\hat{H}_{BCS} = \sum_{\mathbf{k},\sigma} \epsilon_{\mathbf{k}} \hat{c}^\dagger_{\mathbf{k}\sigma}\hat{c}_{\mathbf{k}\sigma} - \frac{g}{V}\sum_{\mathbf{k},\mathbf{k}'} \hat{c}^\dagger_{\mathbf{k}\uparrow}\hat{c}^\dagger_{-\mathbf{k}\downarrow}\hat{c}_{-\mathbf{k}'\downarrow}\hat{c}_{\mathbf{k}'\uparrow} \tag{2.17}$$

It should be emphasised that neglecting pairs with finite momentum fundamentally excludes density fluctuations which will be of future relevance for the description of collective modes. The theoretical discussion of these density fluctuations is postponed to section 4.1. To find an approximate solution for the BCS state, the Hamiltonian can be expanded around the expectation value of the pair operator

$$\Delta = \frac{g}{V}\sum_{\mathbf{k}} \langle \hat{c}_{-\mathbf{k}\downarrow}\hat{c}_{\mathbf{k}\uparrow}\rangle. \tag{2.18}$$

The interaction term in the Hamiltonian 2.17 can then be expressed around this mean-field value yielding

$$\frac{1}{V}\sum_{\mathbf{k}} \hat{c}_{-\mathbf{k}\downarrow}\hat{c}_{\mathbf{k}\uparrow} = \frac{\Delta}{g} + \left[\frac{1}{V}\sum_{\mathbf{k}} \hat{c}_{-\mathbf{k}\downarrow}\hat{c}_{\mathbf{k}\uparrow} - \frac{\Delta}{g}\right]. \tag{2.19}$$

[10] The existence of a bound state is a result of the constant density of states rather than the dimensionality of two.

[11] Finite momentum pairing is only realised in nature when the Fermi surface deviates from a sphere in which case a finite momentum can actually minimise the binding energy. (e.g. FFLO states)

By additionally introducing the Nambu spinor

$$\psi_{\mathbf{k}} = \begin{pmatrix} \hat{c}_{\mathbf{k}\uparrow} \\ \hat{c}^{\dagger}_{-\mathbf{k}\downarrow} \end{pmatrix} \begin{matrix} \text{particles} \\ \text{holes} \end{matrix} \tag{2.20}$$

and using the interaction term 2.19 the Hamiltonian simplifies in this mean-field approach and can be written as

$$\hat{H} = \sum_{\mathbf{k}} \psi^{\dagger}_{\mathbf{k}} \begin{pmatrix} \epsilon_{\mathbf{k}} & -\Delta \\ -\Delta^* & -\epsilon_{\mathbf{k}} \end{pmatrix} \psi_{\mathbf{k}} + \sum_{\mathbf{k}} \epsilon_{\mathbf{k}} + \frac{V|\Delta|^2}{g}. \tag{2.21}$$

The eigenenergies and eigenstates are obtained by diagonalisation of this Hamiltonian. A Bogoliubov transformation[43] establishes the required relation between the Nambu spinor $\psi_{\mathbf{k}}$ and the fermionic quasi-particle creation and annihilation operators $(\gamma_{\mathbf{k},\sigma}, \gamma^{\dagger}_{\mathbf{k},\sigma})$ via

$$\hat{\gamma}_{\mathbf{k}\uparrow} = u_{\mathbf{k}} \hat{c}_{\mathbf{k}\uparrow} - v_{\mathbf{k}} \hat{c}^{\dagger}_{-\mathbf{k}\downarrow} \qquad \text{and} \tag{2.22}$$

$$\hat{\gamma}^{\dagger}_{-\mathbf{k}\downarrow} = v_{\mathbf{k}} \hat{c}_{\mathbf{k}\uparrow} + u_{\mathbf{k}} \hat{c}^{\dagger}_{-\mathbf{k}\downarrow}. \tag{2.23}$$

with $v_{\mathbf{k}} = \frac{1}{2}\left(1 - \frac{\epsilon_{\mathbf{k}}}{E_{\mathbf{k}}}\right)$ and $u_{\mathbf{k}} = \frac{1}{2}\left(1 + \frac{\epsilon_{\mathbf{k}}}{E_{\mathbf{k}}}\right)$. In terms of the quasi-particle operators the mean-field Hamiltonian reads

$$\hat{H} = \sum_{\mathbf{k}} (\epsilon_{\mathbf{k}} - E_{\mathbf{k}}) + \frac{V|\Delta|^2}{g} + \sum_{\mathbf{k}} E_{\mathbf{k}} \left(\hat{\gamma}^{\dagger}_{\mathbf{k}\uparrow} \hat{\gamma}_{\mathbf{k}\uparrow} + \hat{\gamma}^{\dagger}_{\mathbf{k}\downarrow} \hat{\gamma}_{\mathbf{k}\downarrow} \right) \tag{2.24}$$

While the first two terms correspond to the energy of the pair condensate, the third term corresponds to the energy of excited quasi-particles with

$$E_{\mathbf{k}} = \sqrt{\epsilon^2_{\mathbf{k}} + |\Delta|^2}. \tag{2.25}$$

The resulting spectrum is characterised by two branches with $\pm E_{\mathbf{k}}$ that are gapped due to the attractive interaction. The size of the gap at the Fermi momentum $\mathbf{k} = k_F$ is exactly twice the expectation value of the pair operator, $2|\Delta|$, and is hence usually referred to as the superfluid gap. It sets the minimum energy required to remove a particle from the condensate or dissociate a pair.

Obviously, the ground state of the Hamiltonian is the state that satifies

$$\hat{\gamma}_{\mathbf{k}\uparrow} |\Psi_{BCS}\rangle = \hat{\gamma}_{\mathbf{k}\downarrow} |\Psi_{BCS}\rangle = 0 \tag{2.26}$$

and is characterised by the absence of any quasi-particle excitations. After proper normalisation the ground state is given by a coherent superposition of *Cooper pairs* with opposite momentum on the Fermi surface [42]

$$|\Psi_{BCS}\rangle = \prod_{\mathbf{k}} \left(u_{\mathbf{k}} + v_{\mathbf{k}} \hat{c}^{\dagger}_{\mathbf{k}\uparrow} \hat{c}^{\dagger}_{-\mathbf{k}\downarrow} \right) |0\rangle. \tag{2.27}$$

The BCS state $|\Psi_{BCS}\rangle$ can explicitly be written[12] as a coherent state when expanded in terms of an exponential [42]

$$|\Psi_{BCS}\rangle \sim \exp\left[\sum_{\mathbf{k}} -\frac{v_{\mathbf{k}}}{u_{\mathbf{k}}} \hat{c}^{\dagger}_{\mathbf{k}\uparrow} \hat{c}^{\dagger}_{-\mathbf{k}\downarrow} \right] |0\rangle \tag{2.28}$$

$$\equiv \exp\left[\hat{b}^{\dagger} \right] |0\rangle \tag{2.29}$$

$$= \sum_{n} \frac{1}{n!} \left[\hat{b}^{\dagger} \right]^n |0\rangle \tag{2.30}$$

[12] omitting the normalisation

where $\hat{b}^\dagger$ is the pair creation operator. Although the pair operator $\hat{b}^\dagger$ contains fermion pairs as composite bosons, it is not strictly a bosonic operator since its commutator $[\hat{b}, \hat{b}^\dagger]$ explicitly depends on the fermionic operators $\hat{n}_{\mathbf{k}\sigma} = \hat{c}^\dagger_{\mathbf{k}\sigma}\hat{c}_{\mathbf{k}\sigma}$. Under the assumption that the expectation value $\langle \hat{n}_{\mathbf{k}\sigma} \rangle \ll 1$ the BCS ground state represents a true bosonic coherent state $|\Psi_{BCS}\rangle = \exp(\hat{b}^\dagger)$, a Bose-Einstein condensate. [44]

All other eigenstates can simply be constructed from the ground state by subsequently climbing up the ladder. The mixing of different particle numbers gives rise to off-diagonal long-range order that dictates the macroscopic properties. The special case of a non-interacting Fermi sea is reached when $u_{\mathbf{k}} = 0, v_{\mathbf{k}} = 1$ inside the Fermi sea ($k < k_F$) and $u_{\mathbf{k}} = 1, v_{\mathbf{k}} = 0$ outside. [42]

The presented derivation via pairing field is analogous to Bogoliubov description of an interacting Bose-Einstein condensate, where creation and annihilation operators are replaced by the square root of the number of the condensed atoms $\sqrt{N_0}$ [32] yielding a similar coherent ground state. In consequence the derived wavefunction 2.27 describes the entire range of pairing, from tightly-bound bosonic molecules to weakly and non-interacting fermions. In the following we want to explore these limits.

A journey across the BEC-BCS crossover

In order to parameterise which regime is realised and to quantify the interaction strength it is useful to introduce the dimensionless interaction parameter $\eta = 1/(k_F a)$.

In the **BCS limit** of weak interactions, where $\eta \to -\infty$, Pauli blocking dominates over the interaction energy and pairing occurs only on a narrow shell of momenta δk on the Fermi surface where $\mathbf{k} = k_F$. Writing down the pairing wavefunction in second quantisation is straight-forward as it simply corresponds [32] to the creation of a cooper pair with opposite momenta

$$\langle \Psi_{BCS} | \hat{c}^\dagger_{\mathbf{k}\uparrow} \hat{c}^\dagger_{-\mathbf{k}\downarrow} | \Psi_{BCS} \rangle = u_{\mathbf{k}} v_{\mathbf{k}}. \tag{2.31}$$

In real space the result is similarly straight-forward after evaluating the scalar product

$$\langle \Psi_{BCS} | \hat{\Psi}^\dagger_\uparrow(\mathbf{r}_1) \hat{\Psi}^\dagger_\downarrow(\mathbf{r}_2) | \Psi_{BCS} \rangle = \frac{1}{V} \sum_{\mathbf{k}} u_{\mathbf{k}} v_{\mathbf{k}} e^{-i\mathbf{k}\cdot(\mathbf{r}_1 - \mathbf{r}_2)} \tag{2.32}$$

where $\hat{\Psi}^\dagger_\sigma$ are the creation operators at a position $\mathbf{r}_i$ with spin σ. Moving to a relative coordinate $r \equiv |\mathbf{r}_1 - \mathbf{r}_2|$ the wavefunction can be expressed after some mathematical manipulation [25] as

$$\psi(r) \overset{r\to\infty}{\sim} \sin(k_F r) e^{-\frac{r}{\pi\xi}}. \tag{2.33}$$

This real space wavefunction includes an exponential decay term which is proportional to the two-particle correlation length

$$\xi = \sqrt{\frac{\langle \psi(\mathbf{r}) | r^2 | \psi(\mathbf{r}) \rangle}{\langle \psi(\mathbf{r}) | \psi(\mathbf{r}) \rangle}}. \tag{2.34}$$

The latter sets the typical length scale for pairing for any pairing wavefunction [42]. In the BCS limit the pairing length is indeed proportional to the inverse of the small momentum shell

$$\xi_{BCS} \sim \frac{1}{\delta k} \gg \frac{1}{k_F} \tag{2.35}$$

The oscillating term in the spatial wavefunction implies a strong modulation in the order of the inverse Fermi momentum $1/k_F$ but is well-defined in momentum space where it is

confined very close to the Fermi surface [32]. This behaviour of the pairing wavefunction in the BCS limit can also be understood more naively in the context of uncertainty. Due to the dominating effect of Pauli blocking in the formation of Cooper pairs, the momentum is well defined on the Fermi surface. Heisenberg's uncertainty principle implies an according uncertainty in real space far exceeding the interparticle spacing and pairing is hence said to occur in momentum space. We conclude that the BCS regime is dominated by the fermionic nature of the particles. Adding a spin-up and spin-down particle to the system can only happen at the Fermi surface and consequently the chemical potential is

$$\mu \approx E_F. \tag{2.36}$$

Moreover, we have seen that the same confinement to the Fermi surface dictates the pairing behaviour leading to the formation of Cooper pairs in momentum space.

The opposite limit is realised when $\eta \to +\infty$ where fermions form tightly bound molecules with bosonic character and is hence referred to as the **BEC limit**. The chemical potential is composed of contributions from the binding energy and the interaction among molecules and reads

$$\mu = -\underbrace{\frac{\hbar^2}{2ma^2}}_{\text{binding energy } E_B} + \underbrace{\frac{\pi\hbar^2 an}{m}}_{\text{interaction}} \tag{2.37}$$

where n is the density and m the mass of individual fermions [32]. The negative sign of the binding energy E_B reflects the fact that the pairing is favourable whereas the positive sign of the interaction term implies a repulsive interaction between the individual molecules. The above mean-field treatment would imply a molecule-molecule scattering length of $a_M = 2a$ but is reduced to a value of $a_M = 0.6a$ [45] due to pair correlations that have been neglected by the assumption of binary s-wave collisions. The pairing wavefunction 2.31 can be evaluated in the relative radial coordinate r by substituting $u_{\mathbf{k}}v_{\mathbf{k}} \propto (1 + (\mathbf{k}a)^2)^{-1}$ which simply yields

$$\Psi(r) \sim \frac{e^{-r/a}}{r} \tag{2.38}$$

the wave function of a molecule with the size of the scattering length a. Consequently, in the BEC limit the two-particle correlation length equals the scattering length

$$\xi_{BEC} \sim a. \tag{2.39}$$

As opposed to the Cooper pairs in the BCS limit, the two fermions forming bosonic molecules sit in close spatial proximity and hence have a well-defined position in real space, much smaller than the interparticle spacing. The fast oscillating term present on the BCS side effectively vanished and the well defined position in real space entails a respective uncertainty in momentum space. The pairing behaviour is clearly dominated by binding energy exceeding the Fermi energy and pairing effectively occurs in real space on the BEC side. Both regimes are connected smoothly and the associated microscopic and macroscopic quantities vary continuously as there is no phase transition involved. [32]

In the **unitary regime** where $\eta = 0$, the bond length of a molecule tends to infinity as the scattering length diverges. Since the bond length drops out in the description of the many-body state, it effectively renders the unitary Fermi gas scale invariant. In this regime the inverse Fermi momentum k_F^{-1} presents the only length scale in the system and hence the Fermi energy E_F the only energy scale. Both the average energy content of the gas and the binding energy of a pair are then related to the Fermi energy by universal constants. When $\mu < 0$ the superfluid gap Δ vanishes for non-zero k and the minimum excitation energy

lies at $k = 0$ whereas for $\mu > 0$ minimum is found at finite momenta approaching k_F in the BCS limit. Right before the appearance of the molecular bound state the interactions are maximised at the point of unitarity. While macroscopic quantities vary smoothly across the BEC-BCS crossover, the point at which a significant qualitative change occurs depends on the quantity under consideration and usually lies between $0 < \eta < 1$. In this regime many-body pairing still dominates the effect of a weakly bound two-body state ($a \gg k_F^{-1}$) and one can neither speak of a bare molecular BEC nor BCS condensate. [32]

In our experiment the free tunability of the interaction via the Feshbach resonance allows us to realise quantum many-body states across the entire BEC-BCS crossover encompassing the production of a molecular BEC [46] to that of a pair condensate in momentum space. In addition to the binding and Fermi energy the trap confinement introduces an additional energy and length scale in the experiment that can be approximated by the energy of a harmonic oscillator $E_{ho} = \hbar\omega$ and the harmonic oscillator length $a_{ho} = \sqrt{\hbar/(m\omega_{ho})}$ respectively. The competition between these three energy (or length) scales - the Fermi energy E_F, the binding energy E_B and the confinement energy E_{ho} - will ultimately dictate the behaviour of the quantum many-body system.

In the description of our system we have deliberately ignored one energy scale - the thermal energy $E_{th} = k_B T$. However due to our deterministic preparation scheme (see 2.1.3) and exceptionally high ground state preparation fidelities the thermal energy can be neglected in all experiments presented in this thesis.

2.3 Detection methods

The extraction of observables of the quantum many-body state is equally essential as its deterministic preparation (2.1.3) and engineering the Hamiltonian (2.2). This section exclusively encompasses the techniques used in this thesis although other observables are in principle accessible in our system and have been used before [47, 48, 49, 50].

2.3.1 High fidelity atom counting in the μMOT

The natural observable when working with deterministically prepared number states is the expectation value of the number operator $\langle \hat{N} \rangle$ where $\hat{N} \equiv \sum_i \hat{a}_i^\dagger \hat{a}_i$. It should be emphasised that this definition is not equivalent to the number operator $\hat{n} = \hat{a}_i^\dagger \hat{a}_i$ which counts the occupation of Fock states. Simply counting how many atoms are left after the system has evolved under some Hamiltonian in combination with the ability to project onto the ground state already provide a deep insight into the behaviour of the quantum many-body state. More importantly it establishes the foundation for the spectroscopic studies presented in this thesis and even enables the observation of the deterministic preparation described in section 2.1.3.

After execution of the experiment, atoms in all motional and hyperfine states can be re-captured in the MOT. A high axial magnetic field gradient of approximately 250G/cm [35] leads to a strong compression of the sample which increases the signal-to noise ratio, justifying the name μMOT. The fluorescence signal of the atomic cloud is captured over a period of 1.5 seconds on a CCD camera[13] through a side viewport with a numerical aperture of 0.15. Since the intensity is proportional to the number of emitters in dilute samples the integrated signal enables the determination of the number of atoms. The absolute number of atoms is derived by subtracting the background in the selected integration region.

Figure 2.7 shows a histogram of the normalised intensity sums for small particle numbers as well as exemplary truncation boundaries (dashed grey lines) for 2 atoms. This measurement directly corresponds to the deterministic preparation step plot 2.3 and has

[13] Teledyne FLIR Grasshopper 3

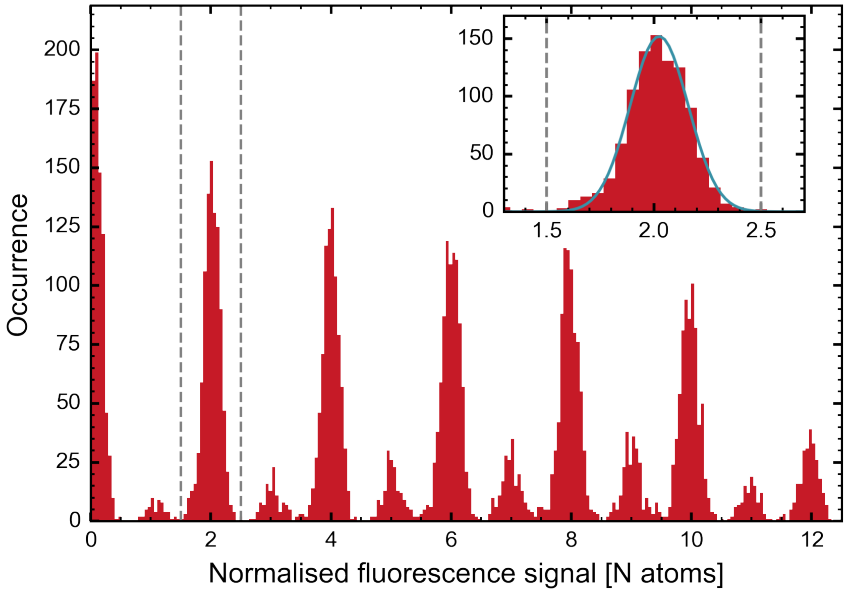

Figure 2.7: **Atom counting in the μMOT** The histogram shows the fluorescence signal normalised to the single-atom intensity when resonantly exciting the atomic sample in the μMOT. The number of atoms can be distinguished after introducing respective boundaries (grey lines) yielding a detection fidelity for $1+1$ atoms of 99.9(7)%. The reduced signal of odd atom numbers is an artefact of the closed shell preparation scheme and does not reflect our ability to count odd atom numbers which is equivalent to that of even numbers.

been derived from the same data. The distinct peaks can be associated with discrete atom numbers when the normalisation constant is chosen to be the intensity sum of a single atom. Fitting a Gaussian (blue curve in the inset) to the peaks and determining how much signal lies outside the boundaries (dashed grey lines) yields an estimated detection fidelity of 99.9(7)% due to the performed truncation. Hence, the limiting factor of this technique is likely the fluctuating background light or the re-capture and limited lifetime in the μMOT, rather than the actual counting. The reduced intensities of odd particle numbers traces back to the closed shell preparation of the harmonic oscillator comparable to the situation established in figure 2.2. Odd particle numbers can be counted equally well as even particle numbers as this only relies on the boundaries of truncation.

2.3.2 Spin-resolved single-atom fluorescence imaging

As an alternative to the atom counting technique in the μMOT the spatially resolved fluorescence signal can also be captured on a camera upon which the position, spatial extent and shape of the atomic cloud can be inferred. As opposed to the μMOT where the atoms are captured in a three-dimensional MOT, here the atoms are resonantly excited in a stroboscopic fashion by two laser beams from opposite sides of the chamber. During the 20 flashing cycles, each lasting 200ns, atoms in the cloud undergo a random walk and spontaneously emit fluorescence photons. Approximately 30 photons per atom are captured through a high NA=0.55 objective from the top of our vacuum chamber and are focused onto an EMCCD camera[14]. By tuning the frequency of the laser[15], a specific

[14] NüVü HNü 512
[15] Toptica DL100 beat-offset locked to the D_2 spectroscopy

hyperfine state can be selected allowing for spin-resolved imaging. To confine the atoms in in the focal plane of the imaging setup, we can introduce an additional axial confinement by superimposing an optical lattice in the axial direction as described in detail in [51]. Two 1064nm beams are focused under a shallow angle creating an interference pattern at the position of the atoms with radially symmetric layers. The created optical dipole potential (compare to 2.1) leads to a trapping of $\omega_r \approx 200$Hz in the radial direction and a much stronger confinement of $\omega_z \approx 15$kHz in the axial direction. This strongly reduces the extent of the wavefunction in axial direction allowing us to probe only a thin layer which matches with the focus plane of the imaging setup. As opposed to quantum gas microscopes[52] the presented stroboscopic imaging technique eliminates the need for an optical lattice in the x-y plane and reduces the imaging time from the order of seconds to a microseconds. Moreover, it significantly simplifies the experimental setup as there is no need for side-band cooling during the long exposure with resonant light in the deep optical lattice.

In principle this technique allows spin and spatially resolved single atom detection of few atoms [53] and has been successfully used to study position and momentum correlations [47, 48, 50] for small atom numbers. Since this technique is not used in the scope of this thesis, further details are omitted.

3 Optical aberration correction

Every real optical system suffers from phase aberrations which inevitably lead to the degradation of the image quality or in our case to the deviation from the desired intensity profile determining the trapping potential. Preparing and probing complex dynamics of quantum many-body systems not only requires the precise knowledge of the confining potential but also depends upon a minimal potential roughness which alters the time evolution. Moreover, a high degree of isotropy of the potential allows for significant simplifications in the theoretical description and an attenuation of undesired heating dynamics. Hence the elimination or at least reduction of optical aberrations marks an essential prerequisite to probe the collective behaviour of our mesoscopic quantum systems.

In order to eliminate the present aberrations the first step is to determine the existing wavefront error in the system with high precision and accuracy and in a second step imprint a phase correction pattern on the light field to compensate for the measured aberrations. Fortunately, the SLM provides a tool to project arbitrary phase patterns onto the light beams and can also be used to measure the wavefront error as described in the following.

This chapter presupposes a basic understanding of Fourier optics, which is for example established in the introductory book by J.W.Goodman [54] and will hereafter be assumed.

When considering an imperfect optical element like a real lens the most rudimentary and naive approach to measure aberrations would be to illuminate the lens with a known beam shape and capture the distortion of the image. Determining the wavefront error in this way is not only difficult and imprecise but only contains indirect information about the phase. In the following we present the experimental implementation of two more advanced techniques to measure wavefront error that in combination significantly reduce the optical aberrations present in our system down to a sub-wavelength level.

3.1 Shack-Hartmann algorithm

Phase aberrations can be treated theoretically [54] by introducing the pupil function of a non-ideal lens

$$p(x,y) = \Theta\left(\frac{D}{2} - r\right) e^{2\pi i W(x,y)}. \tag{3.1}$$

The function takes the value zero outside the lens aperture with a diameter D and acquires an additional phase due to an aberration field $W(x,y)$ inside. Propagating in the z direction the light field $g(\tilde{\mathbf{x}})$ in the focal plane ($z = f$) of the non-ideal lens is then simply given by the spatial Fourier transform of the product of the incident light field $u(x,y)$, and the pupil function yielding

$$g(\tilde{\mathbf{x}}) = \mathcal{F}[u \cdot p](\tilde{\mathbf{x}}_f) \qquad \text{with } \tilde{\mathbf{x}}_f = \frac{\tilde{\mathbf{x}}}{\lambda f}. \tag{3.2}$$

One way to determine optical aberrations is to locally measure the tilt θ of the wavefront as a result of the additional phases introduced by the aberrations. The tilt of the wavefront translates to a displacement

$$d = f \cdot \tan\theta \tag{3.3}$$

of the spot in the focal plane which can for example be detected on a camera. This procedure to measure optical aberrations is commonly referred to as the Shack-Hartmann method. While commercially available solutions usually simultaneously measure the displacements for a discrete sampling grid in a single measurement, we employ a slightly modified version by sequentially determining the displacement for each sampling point one at a time.

Displaying a small aperture with radius $R \ll D$ on the SLM generates a probe beam which locally acquires an additional phase gradient while propagating through aberrated optical components with respect to an unaberrated system as schematically depicted in figure 3.1(a). By successively moving the centre position of the aperture across the SLM and recording the position of the spot $\tilde{\mathbf{x}}_f$ in the image plane we can measure the aberration induced displacement with respect to an unaberrated system for each sampling point $\mathbf{x}_i$.

Experimentally we define a sampling grid of $N = 16 \times 12$ points $\mathbf{x}_i$ with $i = 1, ..., 192$ and each record a single image on the monitoring camera which is conveniently placed in the Fourier plane of the SLM (see figure 2.4). We thereupon extract the displacement vector $\mathbf{d}_i = (d_x d_y)^\top$ for each sampling point $\mathbf{x}_i$ by fitting a Gaussian in both x and y direction to the recorded intensity profile. Since the size of aperture D of the optical system is in general smaller than area covered by the rectangular sampling grid we discard images that do not contain any signal. The corresponding displacement vector field is shown in figure 3.1(b) and represents the (discrete) gradient field $\mathcal{G}$ of the optical phase. Reconstruction of the the full wavefront can consequently be achieved by integrating the gradient field. However as opposed to integrating the gradient field directly and interpolating it to match the resolution 800×600[1] of the SLM, we instead reconstruct the wavefront in the basis of $k = 28$ rectangular Zernike polynomials. Zernike polynomials are commonly used to characterise optical aberrations with low spatial frequencies as they represent the eigenmodes of a circular aperture and directly correspond to typical optical aberrations such as astigmatism or coma. The corresponding phase patterns are shown in figure A.4 in the appendix. Every wavefront $W(x, y)$ can therefore be constructed from the set of Zernike polynomials $\{Z_i\}$ via a linear decomposition of the form

$$W(x, y) = \sum_{i=1}^{k} y_i Z_i \tag{3.4}$$

where y_i is the respective Zernike coefficient. To obtain the spatial representation we start by generating the rectangular Zernike polynomials by performing a gram-schmidt orthonormalisation over the given circular modes on a grid with the same resolution as our SLM (800×600). [55] In a second step we compute the gradients of each Zernike polynomial for each aperture patch using a sobel filter and construct a $(2N, k)$-sized matrix $\mathcal{A}$ containing the gradients for each sampling point $\mathbf{x}_i$. We flatten the two-dimensional gradient map $\mathcal{G}$ into a one-dimensional $(2N, 1)$-vector $\mathbf{g}$ and and solve the matrix equation

$$\mathcal{A} \cdot \mathbf{y} = \mathbf{g} \tag{3.5}$$

by least-squares fitting. The resulting coefficient vector $\mathbf{y}$ fully describes the aberrations in the basis of Zernike polynomials and can hence be used to reconstruct the full wavefront by subsequent multiplication according to equation 3.4. The full phase map which is shown in figure 3.1(b) is relatively flat in the relevant central region with deviations of less than $\lambda/2$, corresponding to a phase of π. Displaying the inverted fitted phase map on the SLM should thus significantly reduce the measured aberrations. The reduced distortion of different beam patterns observed on the camera after projecting the correction map provides convincing evidence for the successful application of the algorithm.

[1] In principle our SLM has a resolution of 792×600, however the SLM control software allows us to define the maps with a resolution of 800×600.

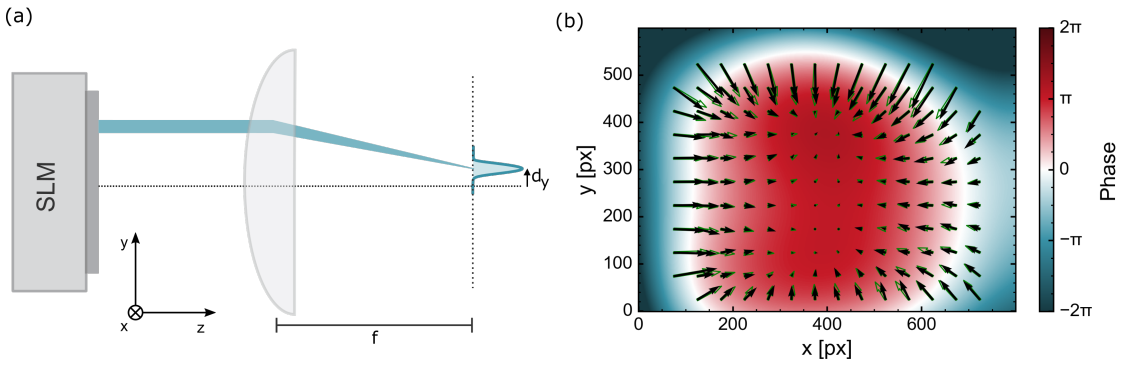

Figure 3.1: **Aberration correction with the Shack-Hartmann algorithm** (a) A beam propagating through an aberrated optical system acquires an additional phase that leads to a measureable displacement d_y in the image plane. (b) Fitting a set of Zernike polynomials to the displacement vectors (black arrows) for each sampling point yields the underlying phase map. The good agreement between the measured vectors and the fitted gradients (green arrows) confirms the satifactory fit of the model.

Measuring and correcting the aberrations through the angular deflection of the wavefront is well suited to measure large optical aberrations corresponding to significant tilts. However the pixel size of the camera ultimately sets an inevitable limit to the smallest displacements and corresponding phase errors that can be detected using this technique. For the precise control of many-body quantum states in tailor-made potentials even flatter incident wavefronts are required which raises the need for a different technique.

3.2 Phase-shift interferometry

Interferometric techniques have become the preferred method to characterise optical systems as they do not rely on absolute intensity profile but instead probe the relative phase of two beam paths. In the following we present an implementation of phase-shift interferometry to measure the wavefront error across the entire aperture of the optical system on a sub-wavelength level.

3.2.1 Theory

Phase-shift interferometry [4] builds on the idea that two coherent beams locally acquire a relative phase with respect to each other as they are moved across the aperture of the optical system, from which the entire wavefront can be mapped out. Phase errors manifest themselves as an additional phase acquired by the beams passing through the optical element. In the image plane of the optical system this leads to modification of the interference pattern, where the exact position of the peaks and fringes is determined by the relative phase. Since the relative phase between the two beams is known, the additional phase can thus be measured as a deviation from expected interference pattern.

The two beams are generated by projecting two apertures with a radius R and a gradient $\mathbf{g}$ on the SLM. As a consequence of their different positions $\mathbf{x}_1 \equiv (x_1 y_1)^\top$ and $\mathbf{x}_2 \equiv (x_2 y_2)^\top$ on the SLM they probe different patches of the aberration function and thereby acquire different average phase shifts $\Delta\varphi_i = 2\pi\langle W\rangle(\mathbf{x}_i)$ with $i \in \{1, 2\}$. The average region over the aberration function of course corresponds to the area encircled by the circumference with radius R of the apertures. Evaluating equation 3.2 for the two beams with intensities

$I(\mathbf{x}_i)$ yields the amplitude in the Fourier plane

$$g(\tilde{\mathbf{x}}) \sim \sum_i \sqrt{I(\mathbf{x}_i)} e^{2\pi i \tilde{\mathbf{x}}_f \cdot \mathbf{x}_i + i\Delta\varphi_i} \mathrm{Ar}(\tilde{\mathbf{x}}_f R). \tag{3.6}$$

Owing to the finite aperture we multiplied with the airy-disk function $\mathrm{Ar}(\nu) = J_1(2\pi\nu)/\nu$ with the spatial frequency ν. The resulting interference pattern is accordingly given by

$$I(\tilde{\mathbf{x}}) \sim \mathrm{Ar}^2(\tilde{\mathbf{x}}_f R) \left[I_1 + I_2 + 2\sqrt{I_1 I_2} \cos(2\pi \Delta\mathbf{x} \cdot \tilde{\mathbf{x}}_f + \Delta\varphi) \right] \tag{3.7}$$

with $\Delta\mathbf{x} = \mathbf{x}_2 - \mathbf{x}_1$ being the displacement of the apertures and $\Delta\varphi = \varphi_2 - \varphi_1$ the respective resulting phase difference. While in principle the shift of the interference pattern is proportional to the phase difference $\Delta\varphi$, extracting it in this way is imprecise and likely to suffer from systematic errors. Instead an additional phase shift $\delta\varphi$ can be introduced to one of the beam apertures resulting in a shifted interference pattern even in the absence of aberrations. Varying the phase shift $\delta\varphi$ and observing the intensity at a single point in the Fourier plane culminates in the cosinusoidal pattern schematically depicted in figure 3.2(b). Additional phases attributed to aberrations can then be detected as a phase offset $\Delta\Phi$ of the cosine. Sampling the cosine for equally spaced phase shifts $\delta\varphi_j = \frac{2\pi j}{N}$ with $j \in \{0, ..., N-1\}$ results in a sequence of interference patterns $I^{(j)}(\tilde{\mathbf{x}})$ that can be decomposed into a Fourier series as derived by Bruning et al. [4]. The total phase $\Delta\Phi(\tilde{\mathbf{x}}) = 2\pi\Delta\mathbf{x}\cdot\tilde{\mathbf{x}}_f + \Delta\varphi$ is recovered by evaluating

$$\tan(\Delta\Phi(\tilde{\mathbf{x}})) = \frac{\sum_{j=1}^{N} I^{(j)}(\tilde{\mathbf{x}}) \sin(\delta\varphi_j)}{\sum_{j=1}^{N} I^{(j)}(\tilde{\mathbf{x}}) \cos(\delta\varphi_j)}. \tag{3.8}$$

Under the assumption that $W(x, y)$ is a continuous function of (x, y), any appearing discontinuities in the phase can be resolved by adding $\pm 2\pi$, which effectively unwraps the phase and maps $[-\pi, \pi) \to (-\infty, \infty)$. [4] The phase difference $\Delta\varphi$ appears by fitting a gradient to the unwrapped phase and determining the offset, which exactly corresponds to the aberration induced phase difference. To obtain a full phase map of the aberration function $W(x, y)$ one would keep one reference beam steady and subsequently move the other "probe" beam across the aperture of the optical system. For each position $\mathbf{x}$ the phase is varied and the sequence of intensity patterns is recorded. The aberration induced phase is extracted by fitting the Fourier decomposed phases from the interference patterns according to equation 3.8 for each position $\mathbf{x}$ and stitching them together to a discrete phase map. Since the coarseness of the discrete phase map and thus the coarseness of the phase recovery depends on the radius R of the two apertures, one would try to minimise R. Decreasing the radius R however leads to a quadratic decrease in power behind the SLM, such that the ability to detect the interference pattern ultimately sets a lower limit for the minimum radius and determines the respective coarseness. Once the phase map is recovered it must be smoothed and extended the to fit the 800×600 aspect ratio of the SLM. Projecting the inverted phase map on the SLM is in succession expected to cancel the measured aberrations.

3.2.2 Experimental determination of phase aberrations

So far we have not discussed how the interference pattern is detected and what aberrations can actually be measured. Naively, one would place a camera behind all optical elements and map out the phase aberrations. In our case we can actually use the camera which is placed in the Fourier plane of the SLM (see figure 2.4) to monitor the light field. The measured pupil function will then include all aberrations from the optical elements between the SLM and the camera. However this leaves us with a problem: how can we be sure that

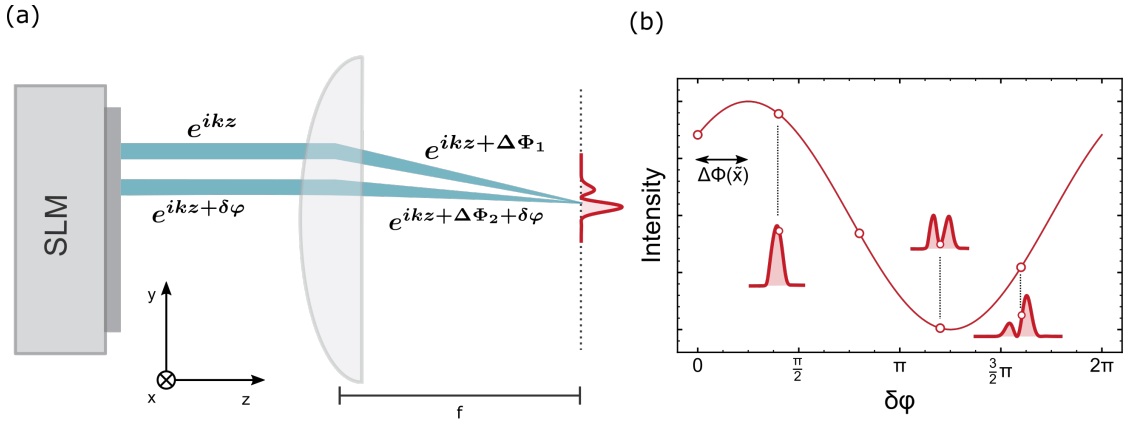

Figure 3.2: **Phase-shift interferometry** (a) Two beams with a relative phase offset $\delta\varphi$ probe different regions of an optical element. Any aberrations manifest themselves as a deviation from the expected interference pattern in the image plane. (b) When observing a single pixel in the interference pattern as the injected phase $\delta\varphi$ is varied, the cosine pattern emerges. From the offset $\Delta\Phi(\tilde{\mathbf{x}})$ one can infer the additional phase picked up due to the aberrations.

the light field on the camera and the light field on the atoms are the same? In reality this is indeed not the case since additional aberrations are picked up further along the beam propagation towards the atoms, mainly introduced by a dichroic mirror and the objective, which is used to focus the beam through the vacuum window into the chamber. Placing a camera in the focal plane of the objective is technically impossible in our setup[2], so is the measurement of aberrations of the vacuum window without breaking the vacuum to put a camera inside. To circumvent this limitation we can use the atoms themselves to probe the light field as has initially been suggested by Zupancic et al. [5]. To correct the aberrations in our system we first perform an aberration correction with the PSI algorithm using the camera and in the second step measure the remaining aberrations by performing the PSI algorithm again on the atoms with the first correction map present.

On the camera

On the SLM we define a $N = 32 \times 24$ sampling grid with a grid spacing of $2R = 50$px covering the whole aperture of the optical system. While the reference beam with a radius of 25 pixels is kept fixed in the centre, the probe beam is moved across the grid. For each position $\mathbf{x}_i$ on the sampling grid and every injected phase value $\delta\varphi \in \{0, \frac{2}{5}\pi, \frac{4}{5}\pi, \frac{6}{5}\pi, \frac{8}{5}\pi\}$ the interference pattern is recorded on the camera.

For each position $\mathbf{x}_i$ we crop a rectangular region from the raw image containing the signal and subsequently compute the phase $\Delta\Phi$ by Fourier decomposition of the recorded intensity $\mathcal{I}(\mathbf{x}_i)$ for different offset phases $\delta\varphi$ following equation 3.8. To obtain a continuous version we unwrap the phase according to the mapping $[0, 2\pi) \to (-\infty, \infty)$. Observe that the unwrapped phase $\Delta\Phi$ will be "two-dimensional" (see figure 3.3(b)). In a second step we sum up the images $\mathcal{I}(\mathbf{x}_i)$ with all different offset phases $\delta\varphi$ within the region of interest yielding an averaged image over all interference patterns for a given position $\mathbf{x}_i$. This allows us to create a signal mask, which we define by discarding pixels below a certain intensity threshold (figure 3.6(a)). To obtain the offset $\Delta\varphi$ we fit a linear curve to unwrapped phases $\Delta\Phi$ using a RANSAC regressor [56] instead of a simple least-squares method. The method is based on repeated random subsampling, meaning that a subset of inliers are

[2]We cannot move the vacuum chamber without moving the optical setup around it.

more likely to be linearly correlated than the outliers or the combination of both. The best model fit will hence be obtained by the subset that only contains inliers. Randomly selecting subsets and comparing the model fits not only allows for the distinction between outliers and inliers, but at the same time also allows for the determination of the best fit parameters for the subset of inliers. We chose the RANSAC algorithm due to its stability against outliers, which are likely to occur if the phase estimation failed.

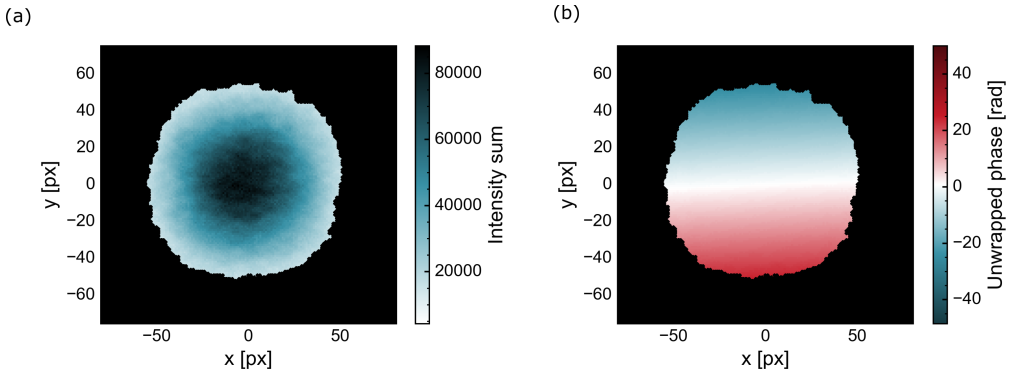

Figure 3.3: **Phase recovery** (a) To create a signal mask we average over all runs and discard pixels below a certain intensity threshold (black crosses). (b) Unwrapped phase $\Delta\Phi$ after performing the Fourier decomposition according to equation 3.8. The linear fit is only be performed within masked region to obtain a single value for $\Delta\varphi$.

For each position $\mathbf{x}_i$ we obtain a phase value $\Delta\Phi$ that can be combined into a two-dimensional phase map $\mathcal{P}$. The recovered phases at the edges are not reliable and have hence been omitted in the following fitting procedure. To recover the full phase map we fit the respective 32×24 grid with a basis set of $k = 28$ rectangular Zernike polynomials. In practise we generate a (N, k)-sized matrix $\mathcal{A}$ similar to the one for the Shack-Hartmann algorithm, but which now contains the actual phases as opposed to the local derivatives for each sampling point. We again solve the matrix equation

$$\mathcal{A} \cdot \mathbf{y} = \mathbf{p} \tag{3.9}$$

where $\mathbf{p}$ is now the flattened (N,1)-dimensional vector corresponding to the phase map $\mathcal{P}$. The solution vector obviously contains k entries corresponding to the coefficients of the Zernike polynomials. The Zernike coefficient vector fully determines the aberrations for the given finite basis of Zernike polynomials. As expected, the major contributions originate from low-frequency polynomials and the coefficients converge to zero for higher frequencies. The particular choice of basis set and interpolation method will be discussed in more detail in section 3.3.3.

Multiplying the Zernike coefficient vector with the Zernike polynomials results in the fitted 800×600 phase map shown in figure 3.4(b). In the construction of the phase map we neglected the offset and tilt corresponding to the lowest three Zernike coefficients as they only alter the position but do not matter for the aberrations. To cancel the aberrations introduced by the optical elements we wrap the phase map again by mapping $(-\infty, \infty) \rightarrow [0, 2\pi)$ and project its inverse on the SLM.

Since the measured phase map varies less than $\lambda/5$ across the probed region, we conclude that the Shack-Hartmann algorithm already compensated the majority of measurable aberrations up to the camera. The aberrations picked up further along the beam path however remain unknown to this point and only running the PSI algorithm on the atoms will allow us to measure and cancel them as we will discuss in the following.

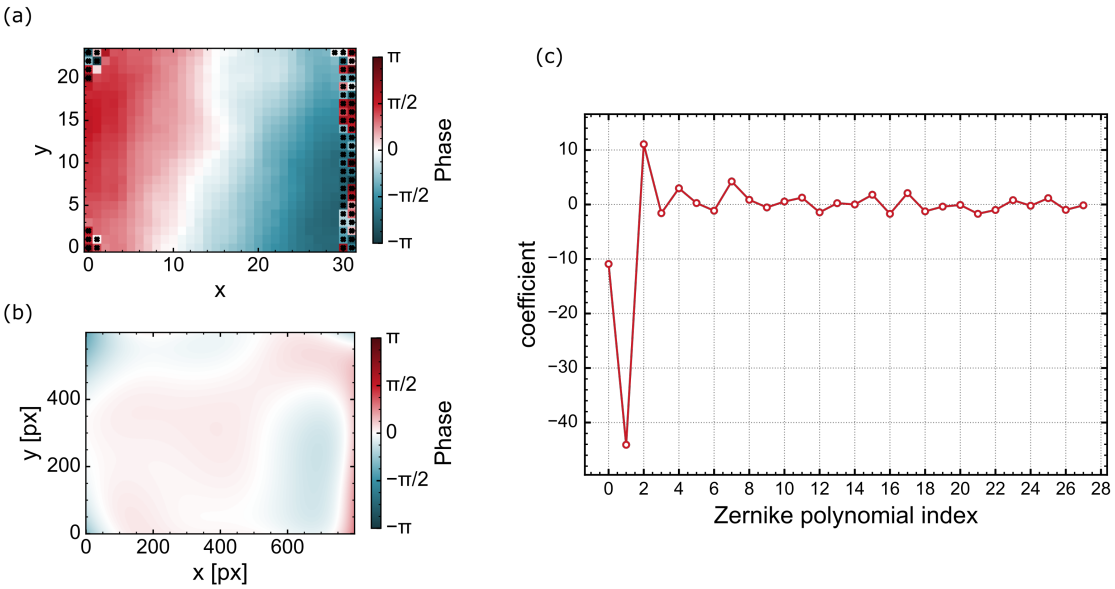

Figure 3.4: **Reconstruction and fitting of the wavefront** (a) The phases for each sampling point on the 32×24 grid can be combined into a phase map. The black crosses indicate points to be neglected in the fitting routine due to lack of signal. (b) The fitted 800×600 phase map is surprisingly flat, which indicates that the Shack-Hartmann algorithm already successfully corrected the majority of the aberrations. (c) In the fitting procedure we omitted the first three Zernike polynomials corresponding to offset and tilt, since they do not represent real aberrations.

On the atoms

As motivated before, the interference pattern can also be projected onto the atoms to measure aberrations from optical elements that are otherwise inaccessible. In accordance with the optical dipole potential 2.1, the atoms will be trapped in the maxima of the interference pattern and if excited resonantly, the observed fluorescence image will contain the necessary information about the light field. While observing the interference fringes on camera is straightforward, the limited resolution on the atoms imposes serious boundaries and jeopardises the successful application of the algorithm. In order to observe the interference pattern we have to maximise the fringe spacing on the atoms by minimising the displacement $\Delta\mathbf{x}$ of the two beam apertures on the SLM according to arguments of Fourier optics. When $\Delta\mathbf{x} = 2R$ the two apertures touch, which allows us to barely resolve two fringes. A smaller fringe spacing does not yield signal on the atoms as the intensity is not high enough for any atoms to remain trapped in the potential. With enough laser power one could circumvent this problem, but the finite imaging resolution would average out the fringe spacing smaller than the diffraction limit. Hence we have to keep the two apertures as close together as possible. To still probe the aberration function $W(x, y)$ across the entire aperture, we have to adapt the algorithm slightly. Instead of only moving one (probe) beam and keeping the other (reference) beam steady, which changes the displacement $\Delta\mathbf{x}$, we now keep the displacement $\Delta\mathbf{x} = 2R$ constant and instead move both apertures together across the SLM with a step size of $2R$. We thereby obtain the phase difference with respect to the neighbouring site and can infer a shear. Measuring the shear in both directions, x and y, subsequently allows us to reconstruct the discrete phase map as discussed above.

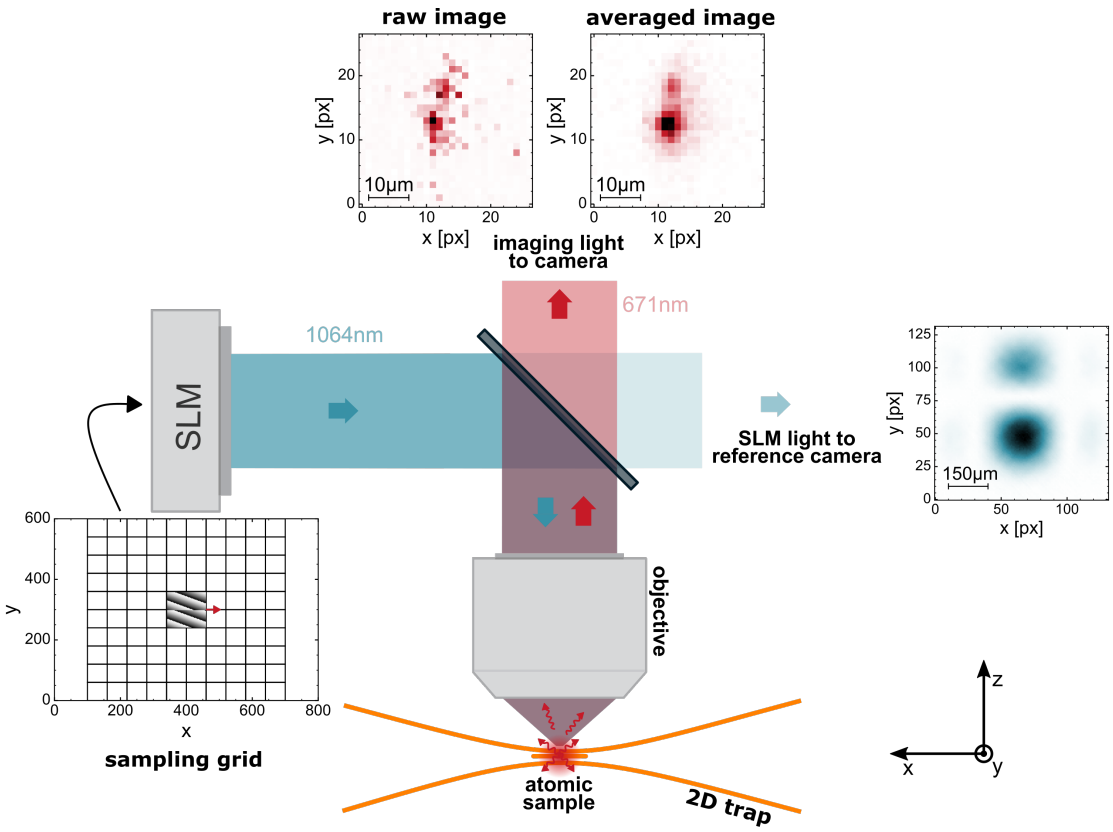

Figure 3.5: **Simplified setup of the PSI algorithm on the atoms** Two beams created by the SLM pick up a relative phase as they propagate through the optical elements which results in a modified interference pattern at the position of the atoms or camera respectively. Capturing the fluorescence signal of the resonantly excited atoms reveals the interference pattern (top images). Subsequent fitting of the averaged image for a given setting allows the determination of the acquired phase. Similarly, the aberrations can also be deduced from the interference pattern of the trapping light which is monitored on a camera (right image). Gradually moving the beams on a sampling grid across the aperture of the system allows for the full reconstruction of the shear (or phase) map.

To maximise the signal we have chosen two rectangular apertures with edge lengths $2R$ and $4R$ respectively as opposed to the circular aperture. Since the intensity profile of the incident beam on the SLM is Gaussian the highest intensity and consequently deepest potential for a given radius is achieved in the centre patch on the SLM. To ensure a constant intensity throughout the entire aperture, we stabilise the laser power using the photodiode behind the SLM. By trial and error a radius of $R = 25$pixels has proven to be optimal. It ensures that the potential is deep enough to trap atoms for each position $\mathbf{x}_i$ on the SLM within the aperture of the objective with a diameter D.

Experimentally, we evaporate for $t \approx 1600$ms in the optical dipole trap before superimposing the interference pattern and thereby loading approximately 100 atoms into the potential. As long as fringes can be observed, the exact number of atoms is not relevant as our technique does not require deterministic preparation. To better confine the atoms in the focal plane of the objective which is the Fourier plane of the SLM, we additionally ramp of the 2D trap and capture the fluorescence image using the technique explained in section 2.3.2. The experimental setup is schematically depicted in figure 3.5. While the signal-to-noise ratio for a single fluorescence image is not adequate to deduce the phase,

averaging over several fluorescence images (like the raw image in figure 3.5) for a given setting $(\mathbf{x}_i, \delta\varphi)$ reveals the emergent intensity pattern (averaged image in figure 3.5).

In concrete terms, we define a quadratic 10×10 sampling grid covering the aperture of the objective. For each of the 100 sampling points $\mathbf{x}_i$ we each record 30 fluorescence images for $N = 5$ different offset phases $\Delta\varphi$.

Similarly to the PSI algorithm on the camera, the phases are obtained by cropping the atom window, generating a signal mask and calculating the Fourier decomposition of the averaged intensity pattern for each setting $(\mathbf{x}_i, \delta\varphi)$. The signal mask and unwrapped phases are shown in figure 3.6(a) and (b) respectively. When comparing the result to the ones obtained by the PSI algorithm on the camera (figure 3.3), the significantly reduced resolution and noisier data becomes apparent and imposes a serious challenge for the accurate reconstruction of the wavefront. The unwrapped phases clearly deviate from a perfect linear gradient in the y (or x) direction which is partially compensated by the use of the RANSAC regressor effectively rejecting outliers. As opposed to the algorithm on the camera, where the phases could be directly extracted, on the atoms we only measured the phase of position $\mathbf{x}_i$ with respect to the neighbouring position $\mathbf{x}_{i-1}$, or in other words the shear. Stacking the apertures next to each other hence yields the discrete shear map $\mathcal{S}_x$ in x direction, whereas stacking them on top of each other yields the shear map $\mathcal{S}_y$ in y direction.

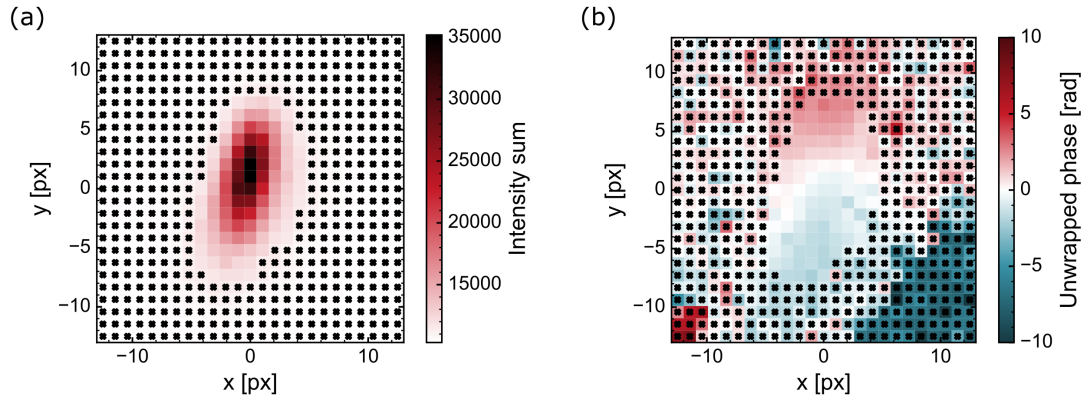

Figure 3.6: **Phase recovery** (a) In the region of interest we create a signal mask by averaging over all runs and discard pixels below a certain intensity threshold (black area). (b) Unwrapped phase after performing the Fourier decomposition according to equation 3.8. The linear fit is only performed within the masked region to obtain a single value for $\Delta\varphi$. Compared to the results obtained on the camera (figure 3.3), the signal is significantly more coarse and slightly distorted.

To recover the full phase map we have to adapt the fitting algorithm slightly, such that the matrix $\mathcal{A}$ contains the shear contributions of each of the k Zernike polynomials for each of the N points on the sampling grid. Since we measured the shear in both x and y direction, we also have to compute the shear contributions of the Zernike polynomials in those two directions yielding a matrix $\mathcal{A}$ of size (2N, k).

The two experimentally obtained shear maps $\mathcal{S}_x$ and $\mathcal{S}_y$ are combined into a flattened $(2N)$ vector $\mathbf{s}$. The fitting is performed in the same way as on the camera by solving $\mathcal{A} \cdot \mathbf{y} = \mathbf{s}$. A quick check of the dimensionality yields

$$\dim[\mathcal{A}] \cdot \dim[\mathbf{y}] = \dim[\mathbf{s}] \tag{3.10}$$

$$(2N, k) \cdot (k) = (2N) \tag{3.11}$$

which confirms that the solution $\mathbf{y}$ is indeed the Zernike coeffcient vector with k entries. For reasons discussed in section 3.3.3 we use $k = 21$ polynomials to reconstruct the 800×600

phase map shown in figure 3.7 after removing offset and tilt. To cancel the aberrations we wrap the phase map and project its inverse on the SLM together with the maps obtained by the Shack-Hartmann algorithm and the PSI algorithm on the camera.

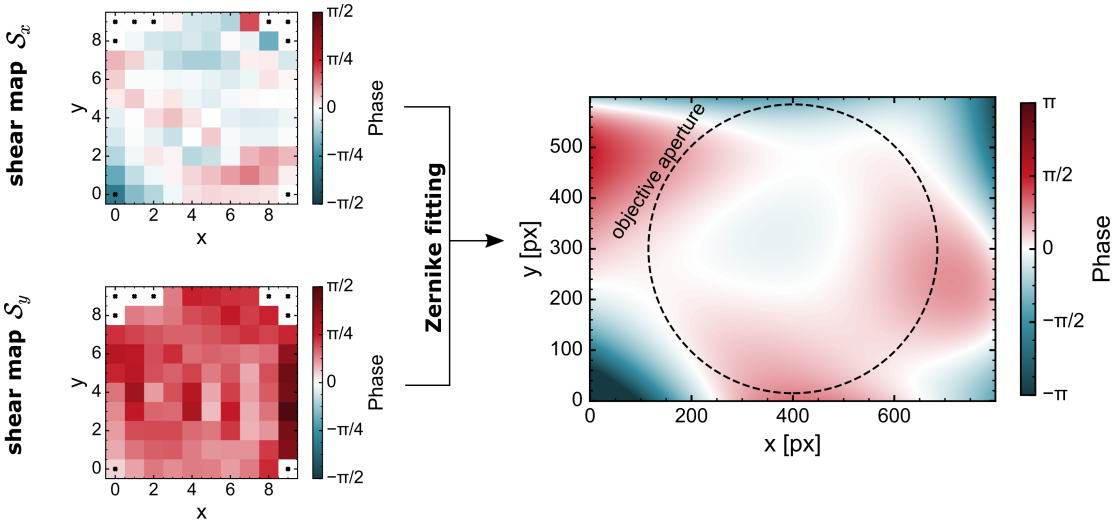

Figure 3.7: **Phase map generation by Zernike fitting** We combine the two shear maps $\mathcal{S}_x$ and $\mathcal{S}_y$ and fit a set of 21 Zernike polynomials to derive a continuous phase map (right). Light outside the circular aperture of the objective (dashed circle) will not hit the atoms and only phases inside the aperture will contribute to the aberrations on the atoms.

The PSI algorithm can of course be applied iteratively to sequentially reduce the aberrations. To improve upon the residual aberrations we hence perform it again using beam 1. Different centre positions of beam 1 and beam 2 on the SLM require slightly different centre positions $\mathbf{x}_i$ of the apertures on the SLM as well as slightly different gradients make it necessary to also measure the aberrations for the second beam.

After these three runs of the PSI algorithm, we verify the success by measuring trap frequencies of the optical tweezer trap generated by beam 1. We prepare 1+1 atoms according to the deterministic preparation scheme described in section 2.2 and subsequently modulate the power of beam 1 sinusoidally with a frequency Ω. If the modulation frequency matches the resonance frequency of the parity-conserving $E^{ho}_{0\to 2}$ transition in the harmonic oscillator potential the atoms will be resonantly excited into the higher level. By spilling a second time to the ground state, atoms in states other than the ground state will be removed. After the second spill the remaining number of atoms is counted in the μMOT (see section 2.3.1) where an excitation is detected as atom loss. Since we are measuring the $0 \to 2$ transition, the resonance frequency at which we detect the atom loss will be twice the trap frequency. Figure 3.8 shows the measurement of the trap frequency with and without the phase maps displayed on the SLM. Without the phase maps (blue squares), we observe two prominent frequencies in the spectrum as opposed to a single resonance frequency corresponding to the $E^{ho}_{0\to 2}$ transition. The appearance of two frequencies can be interpreted as the broken radial symmetry induced by aberrations or other anisotropies. The respective frequencies have been obtained via a Gaussian fit yielding $2\omega_x = 2\pi \times (45.3 \pm 0.2)$kHz and $2\omega_y = 2\pi \times (47.1 \pm 0.2)$kHz respectively, where the choice of direction is arbitrary. When we display all phase maps on the SLM the two peaks shift significantly to higher frequencies $2\omega_x = 2\pi \times (49.6 \pm 0.2)$kHz and $2\omega_y = 2\pi \times (51.7 \pm 0.2)$kHz, but the anisotropy of approximately $\approx 4\%$ still remains. Since the anisotropy cannot be removed in the aberration correction scheme, we do not exclude the wrong incident polarisation as a

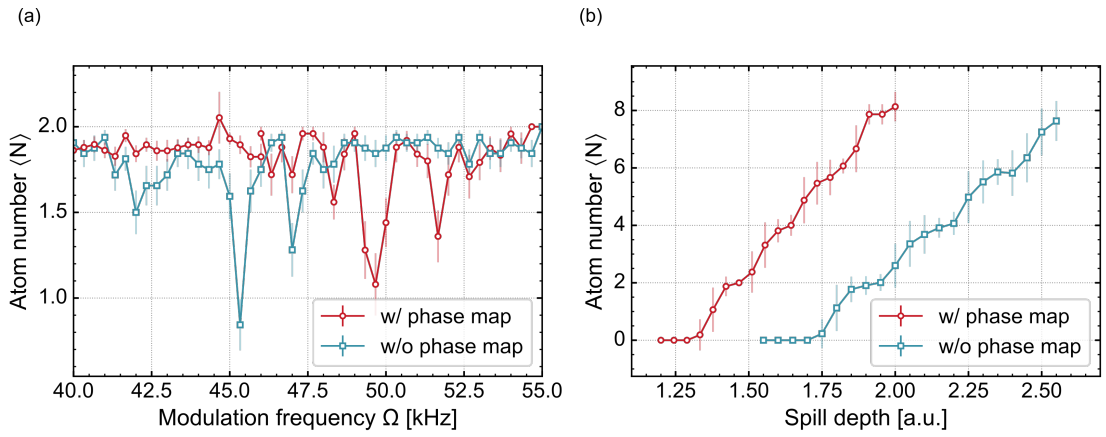

Figure 3.8: **Trap frequencies and deterministic preparation after aberration correction** (a) The sucessful aberration correction is confirmed by a measurement of the radial trap frequency by means of atom-loss spectroscopy in a non-interacting $1 + 1$ system. When displaying the phase correction maps on the SLM, the radial trap frequency (red) increases by $\sim 9\%$ compared to the same measurement (blue) conducted in the absence of correction maps. The anisotropy of approximately 4% could not be removed. (b) Due to the aberration correction the waist of the trapping beam decreased allowing more bound states in the deeper trapping potential. For the same spill depth, more atoms can be trapped and the preparation fidelity increases. The error bars indicate the standard deviations as opposed to the standard error of the mean. The points are connected to provide a visual guide to the eye.

potential cause. The resonance up-shift in the measured excitation spectrum corresponds to an increase in trap frequency of $\sim 9\%$. Since the trap frequency scales anti-proportional with the waist and we kept the optical power constant, the waist must have decreased by $\sim 9\%$. Readers unfamiliar with Gaussian traps are referred to the respective section A.2 in the appendix. Not only does the radial trap frequency after aberration correction exceed the one measured without phase maps, but the reduction of aberrations also manifests itself in a lower ground state spill level as can be seen in the step plot in figure 3.8(b). After applying the correction maps, the entire curve shifts towards lower spill depths signalling that for the same optical power in beam 1, the potential now hosts several bound states. By the same argument as before, the waist of the beam must have decreased. Whereas we could only trap 1+1 atoms for a given optical power, our potential can now trap 4+4 atoms for the same power (spill depth 1.9 a.u.). Moreover, the preparation fidelities increased after applying the phase correction maps, which is reflected in the reduced standard deviations on the steps. We can hence conclude that displaying the phase maps had a positive effect on the homogeneity of the light field and reduced the aberration leading to a smaller waist with a residual anisotropy remaining.

3.3 Precision, accuracy and future prospects

Quantifying the improvement due to the aberration correction is not trivial and should hence be discussed in more detail. In the following we want to deduce an estimate of the error of the presented technique and discuss deficiencies and possible improvements of the algorithm.

3.3.1 Accuracy of the wavefront reconstruction

Not only does the SLM enable us to correct measured aberrations on the atoms, but it also allows us to introduce artificial aberrations to our system. While this appears silly in any running experimental setting it actually offers an excellent bench-marking tool for testing the capabilities of the technique. Concretely, we display a phase map with a known Zernike coefficient and try to reconstruct it by performing the PSI algorithm on the atoms. For testing purposes we choose an astigmatism with Zernike coefficient 5 and a magnitude of 40[a.u.] and create the corresponding phase map (figure 3.9(a)top). Since the aperture of the objective does not fully cover the entire active area of the SLM, we decided to only display the astigmatism on a reduced 600×600 grid and thereby minimise artefacts due to extrapolation issues of the regions that anyway lie outside of the aperture and are not probed by the algorithm.

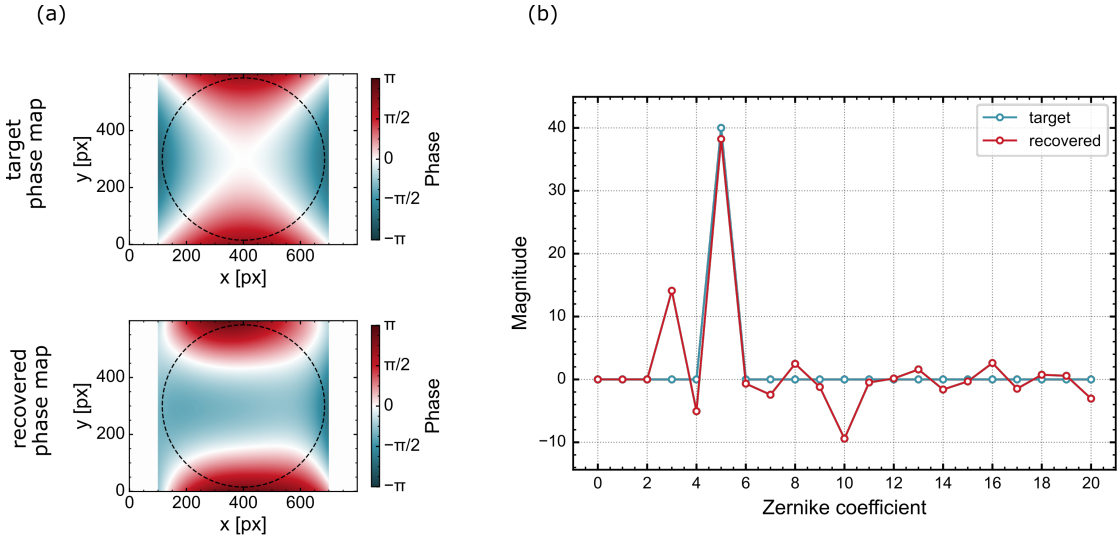

Figure 3.9: **Bench-marking the aberration retrieval** (a) Target phase map (top) with astigmatism that has been displayed on the SLM in contrast to the recovered phase map (bottom). The dashed circle illustrates the aperture of the objective. (b) Zernike coefficients of the target map (blue) displayed on the SLM and recovered phase map (red) from the atoms.

To obtain the phase map we followed exactly the same steps as before, recovered the shear maps for both directions and fitted them using 21 Zernike polynomials. The result which is shown in figure 3.9(a) shows unmissable deviations from the target phase map depicted above which requires further interpretation. As opposed to comparing the two phase maps by eye it is more meaningful to compare their respective Zernike coefficient vectors plotted in figure 3.9(b). While the magnitude of the target astigmatism coefficient 5 is recovered comparatively well with up to approximately 7% residual error, other coefficients deviate much more significantly from the expected target value of zero. The defocus (Zernike coefficient 3) could be attributed to a shift of the layer position of the 2D trap between the runs, a behaviour which has been observed in previous experiments. The other non-zero coefficients could either originate as a consequence of fitting instabilities, noise on the signal from the atoms or from residual aberrations that have not been removed by the initial aberration correction (see section 3.2.2). An even better and in particular basis-independent measure to quantify the deviation between the target map and recovered

phase map is the root-mean-square (RMS) error[3] which we compute by subtracting the target and recovered phase maps point-wise and find a wavefront error of $\sigma_{rms} \leq \lambda/13$. The RMS error represents an average accuracy for the phase retrieval on the atoms. As anticipated the peak-to-peak (pp) error of $\sigma_{pp} \leq \lambda/5$ is significantly higher and thereby sets an upper bound for the accuracy of PSI algorithm performed on the atoms. From the RMS error we can calculate the peak intensity attenuation, usually referred to as the Strehl ratio S via the Ruze relationship[4] [57, 58]

$$S \approx e^{-(2\pi\sigma_{rms})^2} \tag{3.12}$$

which yields $S = 0.80$.

Of course, the accuracy also depends on the signal-to-noise ratio and consequently also on the number of fluorescence image averages for a given setting $(\mathbf{x}_i, \delta\varphi)$. Sub-sampling the measurement dataset allows us to explore the effect of noise on the RMS error. We generate batches consisting of n fluorescence images per setting and subsequently perform our data analysis and waveform reconstruction. In a second step we compare the fitted wavefront with the target astigmatism map and calculate the residual deviation in terms of a root-mean-square error which is shown in figure 3.10. As expected, increasing the number of averages improves the accuracy of the wavefront reconstruction measured by the reduced RMS error. The error will eventually converge to a finite value where adding an additional fluorescence image does not significantly change the averaged image used to determine the phase. Due to the limited experiment time we only took nine fluorescence images per setting for the bench-marking test as opposed to the 30 images for the actual aberration correction.

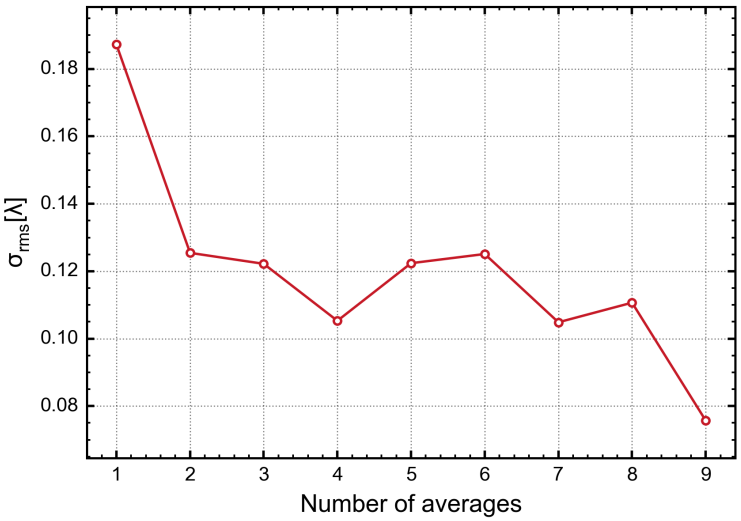

Figure 3.10: **Dependence of the RMS wavefront error on the number of averages** The root-mean-square wavefront error σ_{rms} decreases as the number of averages, from which the phase is extracted, is increased. The data points are connected to better illustrate the changing behaviour. The numerical precision is much smaller than the data points.

[3] $RMSE[\lambda] = \frac{1}{2\pi}\sqrt{\frac{1}{N}\sum_{l=1}^{N}(x_l^{tar} - x_l^{rec})^2}$, where $N = 600^2$ is the number of sampling points, x_l^{tar} the value at the of the target map and x_l^{rec} the value of the recovered phase map.

[4] The approximation only holds for $\sigma_{rms} \leq \lambda/5$. [57]

3.3.2 Precision of the wavefront reconstruction

Not only the accuracy of the wavefront reconstruction represents an important measure but also the precision which quantifies the statistical spread of different runs for the same aberration function. Due to the limited runtime on the experiment we can only afford to run the algorithm twice and estimate the variation by that, which is only statistically significant in the limit of many repetitions. Measuring the induced astigmatism phase map twice and calculating the difference between the two recovered phase maps results in a precision of $\sigma_{rms} \leq \lambda/25$. The measure can be understood as an upper limit for the reproducibility of the wavefront reconstruction. Since the measurements were performed on different days with other measurements in between, the value not only quantifies the precision of the algorithm itself but also includes the experimental stability.

3.3.3 Choice and size of the basis set

To test the dependence on the size of the basis set we can compute the RMS error σ_{rms} as a function of the number of Zernike polynomials m in the basis set. For each number of Zernike polynomials we fit the recovered shear maps and calculate the RMS error with respect to the target phase map. The result is shown in figure 3.11. If the basis set does not even contain the coefficient of interest, which in our case is the coefficient 5 corresponding to the astigmatism, the phase fitting can obviously not reflect the structure of the aberration leading to a large wavefront error. The lowest value for σ_{rms} is found for the case when the maximum coefficient included in the basis set equals the coefficient of interest. Usually the aberrations in a practical setting are however unknown and hence the choice of the size of basis set is not trivial. For our 10×10 grid we observe a decrease in the RMS error in the region between $m = 5$ and $m = 21$. Considering more than 21 Zernike polynomials again leads to a gradual increase in the RMS error before it becomes numerically unstable at $m = 46$. Choosing 21 Zernike polynomials has hence proven to be optimal as it maximises the considered spatial frequency while still maintaining a small RMS error. Since only an infinite set of Zernike polynomials forms a complete basis set, truncating the basis at a filled radial configuration[5] is also advantageous as it should maximise the symmetry of the truncated basis.

Zernike polynomials are commonly used as a basis set due to their relation to the normal modes of an aperture and we chose the rectangular version in accordance with our quadratic sampling grid. However they are not always the best choice to model the measured aberrations. Owing to the truncated basis and consequent loss of orthogonality the effect of one Zernike polynomial can be compensated by another one. This leads to the well-known Runge phenomenon [59] occurring when the size of the basis is too large with respect to the number of discrete and equidistant sampling points. In this case, the amplitude of the Zernike coefficients will be uncontrollably large and the reconstructed wavefront will oscillate on the edges. Consequently, the accuracy of the wavefront reconstruction diminishes. While more advanced non-equidistant sampling grids (Chebyshev sampling) can circumvent this problem, there exists a much simpler solution for reliable wavefront reconstruction. If the exact type of aberration is irrelevant to the end-user, who only wants to achieve the best cancellation of aberrations, then an spline interpolation method might be better suited and is currently under development. Since we are measuring shears as opposed to the actual amplitude, the algorithm can be improved by considering additional constraints to the wavefront. One such example would be the additional constraint that emerges from the assumption of a continuous aberration function $W(x, y)$. In two dimensions the problem of phase reconstruction is overconstrained as multiple paths lead to the same grid point. If we consider four adjacent grid points forming a rectangle one can im-

[5] Considering the lowest 21 Zernike polynomials includes all polynomials up to the fifth radial degree.

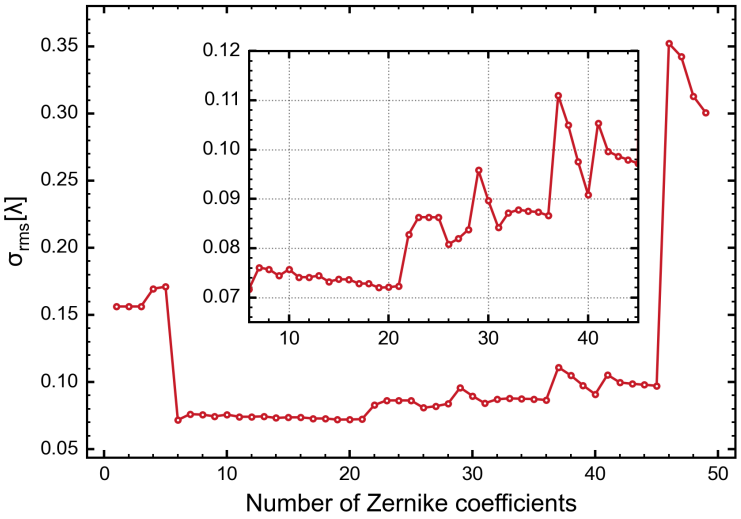

Figure 3.11: **Dependence of the RMS wavefront error on the size of the basis set** The ideal number of Zernike polynomials (21) minimises the root-mean-square error σ_{rms} while maximising the spatial variation. Considering more than 21 Zernike polynomials increases the wavefront error and the fitting routine becomes numerically unstable at a coefficient of 46. The data points, whose numerical precision is negligible, are connected to better illustrate the changing behaviour.

mediately deduce that the curl of the shears much vanish within each rectangle. In other words, shears along closed paths must add up to zero. While this constraint will generally not be satisfied in the presence of noisy data, it may be used to improve the accuracy of the phase map reconstruction.

3.4 Discussion

By using a combination of the Shack-Hartmann algorithm on the camera and iterative applications of the PSI algorithm on the camera and atoms we have successfully demonstrated a reduction of the wavefront error down to a level of accuracy of $\sigma_{rms} = \lambda/13$. The increased isotropy of the trap and higher trap frequency also confirms the pursued goal to better control the preparation and dynamics of the mesoscopic quantum system. While the physical effects certainly proof the remarkable capabilities of the techniques, they each come with their limitations.

While the Shack-Hartmann algorithm is limited in terms of the measurable displacements, phase-shift interferometry on the other hand is incapable of measuring infinitely large gradients. In fact the largest possible gradient g that can be measured and recovered by the algorithm is $g < \frac{\pi}{d}$ where d is the distance between neighbouring positions in the sampling grid. If the gradient between adjacent sampling points is larger than π it is unclear whether the gradient is positive or negative due to the phase unwrapping. This bound is in fact reminiscent of the Nyquist-Shannon sampling theorem [60, 61, 62] which is commonly used in the context of high-frequency signal generation or recording. Larger gradients would lead to an aliasing effect and hence an incorrect reconstruction of the phase. In accordance with this limitation we initially applied the Shack-Hartmann algorithm to flatten the wavefront before progressing with the more evolved PSI algorithm. In general subsequent reduction of the wavefront errors first on the camera and then on the atoms has

proven to be advantageous. Iteratively repeating the algorithm until convergence ensures that the maximum accuracy is achieved.

To better confine the atoms in the focal plane of the objective we additionally superimposed our 2D trap. However this implies that we did not only measure the optical aberrations of the trapping beam but potentially also irregularities of the 2D trap. The absence of the 2D trap did not lead to a significant deviation in terms of isotropy after aberration correction which leads us to the conclusion that the main aberrations originate from the beam path of the tweezer beam. The presented work was based on the assumption that the measured fluorescence signal from the atoms exactly represents the intensity distribution they are subjected to. Obviously, the population of the two wells is non-linear with respect to intensity profile and the fluorescence signal at one point not only depends on the intensity at this point but also on the intensity at all other points. Since we are only measuring the movement of the fringe which is proportional to the injected phase $\delta\varphi$ the non-linear relationship between the intensity profile and the fluorescence image can be neglected. Hence we conclude that the PSI algorithm produces resilient results as long as the interference pattern and central fringe can be resolved adequately.

As opposed to the work by Zupancic et al. [5] we further demonstrated that an optical lattice in the x-y-plane is not required and the interference signal can also be obtained through recurrent averaging over the double well potential. Moreover, we used a spatial light modulator as opposed to a digital mirror device and argue that any device able to create two small beams that can be moved across the aperture and whose relative phase can be varied is sufficient for the successful application of the algorithm.

Although Zernike polynomials are the common choice to construct a phase map, they are not the best choice to model the measured data. For an optimal representation of the data we suggest a spline interpolation, which is currently under development. Most importantly, a spline interpolation does not rely on guessing the truncation of the basis, but instead smoothly interpolates between the measured phases.

4 Collective excitations

Interacting quantum many-body systems behave fundamentally different than their non-interacting counterparts due to their ability to react collectively to an external perturbation. As opposed to the analytically solvable and well understood spectrum of a non-interacting system, that is solely dictated by the external confinement and Fermi statistics, interacting systems exhibit a rich spectrum of single-particle and collective excitations. [32, 63]

Low-energy collective modes and their excitation spectra have been studied extensively in both Bose-Einstein condensates [28, 64] and Fermi gases [6, 31, 65, 66] where they have been used to probe the equation of state, hydrodynamic behaviour or scale invariance at unitarity [67]. Their direct relation to the system's response and velocity fields hence renders them a versatile tool for exploring out of equilibrium quantum dynamics through spectroscopic excitation measurements.

What distinguishes our study in the fermionic cold-atom platform described in section 2 from these, sometimes decade-old studies, is the finiteness of the system. Whereas previous studies all worked in the macroscopic limit with $\sim 10^5$ particles, we now aspire to reduce the particle number by four orders of magnitude and explore the collective dynamics in the mesoscopic limit. In this limit we not only intend to challenge the applicability of hydrodynamics in small size systems, but also probe the limitation of the current theoretical description of collective excitations.

4.1 Theory of collective excitations

Quantum many-body systems that are described by the BCS ground state 2.27 can exhibit two fundamentally different types of excitations - single-particle fermionic excitations or bosonic pair-like excitations. [32]

4.1.1 Single-particle excitations

The single-particle excitations can simply be described by the raising and lowering of the the BCS state which has been discussed in section 2.2.2. For example, the operation

$$\hat{\gamma}^\dagger_{\mathbf{k}\uparrow}|\Psi_{BCS}\rangle = \hat{c}^\dagger_{\mathbf{k}\uparrow}\prod_{\mathbf{l}\neq\mathbf{k}}\left(u_\mathbf{l} + v_\mathbf{l}\hat{c}^\dagger_{\mathbf{l}\uparrow}\hat{c}^\dagger_{-\mathbf{l}\downarrow}\right)|0\rangle \tag{4.1}$$

removes a pair with relative momentum $(\mathbf{k}\uparrow, -\mathbf{k}\downarrow)$ and adds a single fermion with $\mathbf{k}\uparrow$. [32] The energy $E_\mathbf{k}$ associated with this process is exactly the result $E_\mathbf{k} = \sqrt{\epsilon^2_\mathbf{k} + |\Delta|^2}$ (2.25) found by diagonalising the mean-field BCS-Hamiltonian 2.24. This confirms the intuitive picture that adding or removing a single fermion at an energy cost $E_\mathbf{k}$ creates a quasiparticle with an excitation energy $E_\mathbf{k}$. While the described operation is not particle number conserving, it is also possible to excite the system by creating two unpaired particles which consequently satisfies particle number conservation. One example of such a process is the removal of a particle with a momentum $\mathbf{k}$ and adding it back at a different momentum $\mathbf{k}'$. Alternatively, pairs can also be excited into an orthogonal state with respect to the ground state according to

$$\hat{\gamma}^\dagger_{\mathbf{k}\uparrow}\hat{\gamma}^\dagger_{-\mathbf{k}\downarrow}|\Psi_{BCS}\rangle = \left(v_\mathbf{k} - u_\mathbf{k}\hat{c}^\dagger_{\mathbf{k}\uparrow}\hat{c}^\dagger_{-\mathbf{k}\downarrow}\right)\prod_{\mathbf{l}\neq\mathbf{k}}\left(u_\mathbf{l} + v_\mathbf{l}\hat{c}^\dagger_{\mathbf{l}\uparrow}\hat{c}^\dagger_{-\mathbf{l}\downarrow}\right)|0\rangle \tag{4.2}$$

The associated energy of this orthogonal state lies $2E_k$ above that of the ground state. In the BCS limit this corresponds to $2|\Delta|$ whereas in the BEC limit it is given by $2\sqrt{\mu^2 + |\Delta|^2}$. [32]

All of the presented excitations, whether they are particle number conserving or not, are limited to a single pair breaking up or even just a single fermion being added or removed. Collective excitations on the other hand rely on the interplay between many of these pairs which stimulate novel phenomena described in the following.

4.1.2 Collective excitations

In the derivation of the BCS ground state terms with non-zero centre-of-mass momentum $\mathbf{q} \neq 0$ have been omitted. Allowing finite momenta $\mathbf{q}$ in the BCS formalism gives rise to density fluctuations in addition to single-particle excitations, which are often referred to as sound waves. Which type of excitations is dominating depends on the frequency and momenta considered. At low frequencies the spectrum is characterised by a gapless phononic dispersion with a slope which corresponds to the sound velocity as expected for sound waves. At higher frequencies one finds a continuum of excitations as a result of pair breaking into single-particle fermionic excitations (see section 4.1.1). [63] The threshold frequency ω_{th} which determines the onset of pair-breaking varies across the BEC-BCS crossover and is generally given by [63]

$$\omega_{th} = \min_{\mathbf{k}}(E_+ + E_-) \qquad \text{with} \qquad E_\pm = \sqrt{\left(\frac{\hbar^2(\mathbf{q}/2 \pm \mathbf{k})^2}{2m} - \mu\right)^2 + \Delta^2} \tag{4.3}$$

where $E_\pm$ is the energy of a quasi-particle excitation with momentum $\hbar(\frac{\mathbf{q}}{2} \pm \mathbf{k})$. By construction the quasiparticle energy $E_\mathbf{k} = E_+ = E_-$ from equation 2.25 together with the condition $\mathbf{k} \cdot \mathbf{q} = 0$ minimises the expression 4.3 which yields the corresponding threshold energy [63]

$$\hbar\omega_{th} = \begin{cases} 2\Delta & \text{for } \mu > 0 \text{ and } \hbar q < 2\sqrt{2m\mu} \\ 2\sqrt{\left(\frac{\hbar^2 q^2}{8m} - \mu\right)^2 + \Delta^2} & \text{for } \mu > 0 \text{ and } \hbar q > 2\sqrt{2m\mu} \text{ or } \mu < 0 \end{cases} \tag{4.4}$$

In the BCS regime and at unitary, where the first case in equation 4.4 applies, the minimum of $E_+ + E_-$ is at $\frac{\hbar^2 k^2}{2m} = \mu - \frac{\hbar^2 q^2}{8m}$. In the BEC regime on the other hand, where the second case applies, the energy minimum is found at $k = 0$. Intuitively, the threshold energy is then the energy required to break a molecule with a binding energy of $E_\mathrm{B} = 2|\mu|$ into two fermions, which carry a total momentum of $\mathbf{q}$. [63] This "microscopic" threshold frequency is directly related to the macroscopic Landau criterion if one defines Landau's critical velocity as

$$v_c = \min_q \frac{\omega_{th}(q)}{q}. \tag{4.5}$$

While the phonon branch merges into the single-particle continuum in the BCS limit already at low frequencies, it extends to much higher frequencies in the BEC limit. In the latter it changes its characteristic linear dispersion of phonons to a quadratic dispersion reminiscent of free bosonic molecules with an energy $\frac{\hbar^2 q^2}{4m}$ and a mass of $2m$. In the intermediate regime around unitarity the phonon branch is expected to extend up to momenta in the order of the Fermi momentum above which pair-breaking again dominates. [63] Recent measurements by Biss et al. [68] confirm the described dispersion across the BEC-BCS crossover.

The low frequency excitations can be described by a redistribution of momenta owing to collisions among constituents comparable to conventional sound. In a gas density fluctuations can only be mediated by collisions whereas in a Fermi liquid interactions give rise to additional non-trivial collective, but collisionless oscillations of the Fermi surface, called zero sound which will not be of further interest and is only mentioned for completeness. [42] The excitation frequencies ω of collisional sound waves[1] are much smaller than the quasi-particle scattering rate τ^{-1} and in particular bounded by the Fermi velocity $v_F = \frac{\hbar k_F}{m}$. Consequently, the asymptotic behaviour of $\omega\tau$ distinguishes the hydrodynamic ($\omega\tau \to 0$) from the collisionless ($\omega\tau \to \infty$) regime. Probing the collective frequency ω can thus act as an indicator for the applicability of hydrodynamic theory. [32, 42]

The structure of low-energy collective modes and the corresponding energy can be obtained by considering variations in the quasi-particle distribution function $n_\sigma(\mathbf{r}, \mathbf{p}, t) \equiv n$. While not strictly necessary we can neglect fluctuations in the spin degree of freedom σ for simplicity[2]. If the characteristic frequency ω is much smaller than the Fermi energy[3] and the characteristic wavevector $\mathbf{q} \ll k_F$ much smaller than the Fermi wavevector, then the distribution function can be treated semiclassically and follows a Boltzmann equation of the form [42]

$$\left(\frac{\partial}{\partial t} + \dot{\mathbf{r}}\frac{\partial}{\partial \mathbf{r}} + \dot{\mathbf{p}}\frac{\partial}{\partial \mathbf{p}}\right) n = -I[n] \tag{4.6}$$

where the right hand side includes collisions between constituents via the collision integral I. Since collisions conserve the particle number, momentum and energy, corresponding conservation laws can be derived for the mass density, momentum density and energy density by taking moments of the Boltzmann equation. In classical hydrodynamics conservation of mass yields the continuity equation, the conservation of momentum entails the Euler equation and energy conservation an energy balance equation. In general the hydrodynamic equations are under-determined, meaning that the number of degrees of freedom exceeds the number of equations. The set of equations can however be closed by introducing additional equations of state. [69]

If the system is subject to an external trapping potential, as is the case for our experiment, the introduction of an additional energy (and length) scale imposes a set of boundary conditions that fundamentally change the mode structure. The result is a discrete spectrum of low frequency collective modes whose structure is dictated by the symmetry of the trap potential and perturbation.

In the following we consider an axisymmetric harmonic trapping potential of the form

$$V(x, y, z) = \frac{m}{2}\left(\omega_x^2 x^2 + \omega_y^2 y^2 + \omega_z^2 z^2\right) \tag{4.7}$$

with $\omega_x = \omega_y = \omega_r$ and $\omega_z \equiv \lambda\omega_r$ which approximates the experimental situation found for a focused Gaussian beam with an experimental anisotropy parameter $\lambda \approx 1/6$. As opposed to the harmonic potential the Gaussian potential only involves a finite number of bound states above which one finds a continuum of scattering states. For low-lying states in the Gaussian potential however, the harmonic potential should well approximate the physical situation. Collective modes describe time-dependent deviations $\delta n(\mathbf{r}, \mathbf{p}, t) =$

[1] While the authors in reference [64] use the excitation energy of the collective mode as a reference, other authors [7] use the trap frequency. Since the discrete collective modes are in the same order as the trap frequencies and the distinction between the two regimes is a consideration of limits, we arbitrarily choose the excitation frequency as a reference.

[2] Remember we are anyway working with a balanced spin-mixture of hyperfine states.

[3] In finite-size systems this might no longer be applicable as the Fermi erngy E_F can well be in the order of the confinement energy E_{ho}.

$n(\mathbf{r},\mathbf{p},t) - n_0(\mathbf{r},\mathbf{p})$ from the equilibrium distribution n_0. The deviations can be rewritten in terms of a trial function Φ following [70] as

$$\delta n(\mathbf{r},\mathbf{p},t) = n_0(\mathbf{r},\mathbf{p})\Phi(\mathbf{r},\mathbf{p},t). \tag{4.8}$$

Linearising the Boltzmann equation in terms of the small oscillatory deviations δn results in

$$n_0 \left(\frac{\partial}{\partial t} + \dot{\mathbf{r}}\frac{\partial}{\partial \mathbf{r}} + \dot{\mathbf{p}}\frac{\partial}{\partial \mathbf{p}} \right) \Phi = -I[\Phi] \tag{4.9}$$

The time evolution of the space and momentum coordinates is given by the classical equations of motion

$$\dot{\mathbf{r}} = \mathbf{v} = \frac{\mathbf{p}}{m} \tag{4.10}$$

$$\dot{\mathbf{p}} = -\frac{\partial V}{\partial \mathbf{r}}. \tag{4.11}$$

The ansatz Φ for the collective modes can be expanded as a sum of a set of basis functions ϕ_i and an oscillating prefactor

$$\Phi(\mathbf{r},\mathbf{p},t) = e^{-i\omega t}\sum_{i=1}^{n} a_i \phi_i(\mathbf{r},\mathbf{p}). \tag{4.12}$$

The set of basis functions ϕ_i include terms of position and momentum in all three spatial directions. The classical moments of the kinetic equation can be obtained by substituting the expansion of collective modes 4.12 into the linearised Boltzmann equation 4.9 and subsequently multiplying it by ϕ_i. Integrating out the position $\mathbf{r}$ and momentum $\mathbf{p}$ finally results in a set of n linear equations of the coefficients a_i for the collective modes. [71] The determinants of the coefficient matrices containing the coefficients a_i determine expressions for the respective mode frequencies. The frequencies of the collective modes will generally be of complex form $\omega = \Re(\omega) + i\Im(\omega)$, where the real part corresponds to the frequency and the imaginary part to the damping of the mode. [70] The collision integral $I[\phi]$ modifies the bare mode frequencies to include terms proportional to an effective relaxation rate τ^{-1} of the collisions.

In general, the mode structure is complicated and only in some limiting cases and under strict assumptions simple analytical expressions exist and modes decouple. The simplest possible motion only requires first order terms[4] of position and momentum in its basis and describes only a simple sloshing motion, which can be associated with the dipole mode. [72] Higher order terms[5] that include products of position and momentum give rise to dynamics beyond centre-of-mass oscillations. A full set of collective modes up to order n can be found by considering all linearly independent solutions derived from sums of permutations of n^{th} order terms following the basis set expansion 4.12. It should be stressed that in the theoretical derivation presented above no assumptions have been made about the system other than it being a trapped gas with collisions. Without any quantum mechanics at play it already predicts the collective mode structure and frequencies. While our derivation using the Boltzmann equation did not rely on the assumption of a condensed Bose gas that can be described by the Gross-Pitaevskii equation (GPE), the same collective mode structure can be derived from a hydrodynamic formulation of the GPE (see appendix A.3). Our classical approach is in this sense more universal as it does not assume a macroscopic wavefunction and also permits deviation from the hydrodynamic limit. It does however

[4] first order basis: $\phi_1 = r$ and $\phi_2 = p_r$ or $\phi_1 = z$ and $\phi_2 = p_z$

[5] second order basis: e.g. $\phi_1 = x^2 + y^2, \phi_2 = xp_x + yp_y, \phi_3 = p_x^2 + p_y^2$ and $\phi_4 = p_z^2$

assume that position $\mathbf{x}$ and momentum $\mathbf{p}$ are well-defined quantities at all time which is certainly not the case when taking the uncertainty principle into account. At this point it is worth noticing that the classical kinetic theory derivation and derivation via the GPE yield the same result, indicating that without further considerations the collective modes cannot be used to make statements about the quantumness of the system.

While the above derivation did not rely on the assumption of hydrodynamics it is useful to first consider the hydrodynamic limit to describe the dynamics of the modes and establish common terminology. In this limit the symmetry of the potential allows the deviation function Φ to be expanded as a product of a radial part and the spherical harmonics depending on the angular momentum degree $l = 0, 1, 2...$ and its orientation $m = -l, ..., 0, ..., l$. In the axisymmetric case the third component of the angular momentum $m_z \equiv m$ remains a good quantity, however the dispersion law will now also depend on m [30]. For $m = \pm l$ and $m = \pm(l-1)$ the solutions of the deviation function are the simple products of the form [30]

$$\Phi(r, \theta, \phi) = r^l Y_{lm}(\theta, \phi) \tag{4.13}$$

whereas for $m = 0$ coupling terms will arise due to the deviation from the spherical case. Owing to the expansion in spherical harmonics the $l = 0$ mode is referred to as the monopole mode, the $l = 1$ as dipole modes and $l = 2$ as quadrupole modes and so on. The following discussion is limited to those ($l \leq 2$) low-lying excitations. For the simple solutions ($m = \pm l, \pm(l-1)$) the corresponding frequencies of the collective modes are [7, 63]

$$\omega(m = \pm l) = \sqrt{l}\omega_r \tag{4.14}$$

and

$$\omega(m = \pm(l-1)) = \sqrt{(l-1)\omega_r^2 + \omega_z^2}. \tag{4.15}$$

Dipole modes The dipole modes ($l = 1$) can be associated with displacements from the equilibrium position in the respective spatial directions with oscillation frequencies $\omega_D(m = \pm 1) = \omega_r$ in the radial and $\omega_D(m = 0) = \omega_z$ in the axial direction. This is exactly the result expected for a harmonic oscillator potential. This coincidence of the hydrodynamic and harmonic oscillator frequency reaffirms that centre-of-mass oscillations are not affected by interactions.

Quadrupole modes The radial quadrupole modes ($m = \pm 2$) are described by a velocity field $\mathbf{v} \propto \nabla(x \pm iy)^2$ and their macroscopic motions can be described by an alternating elongation of the system in the x-y plane while the volume remains constant. Since the volume remains constant the mode is independent of the equation of state in the limits of our assumptions, which renders it an excellent probe for studying hydrodynamics. In the hydrodynamic limit the frequency is simply $\omega_Q^{hd}(m = \pm 2) = \sqrt{2}\omega_r$. In the collisionless limit one can consider determinant equations[6] derived from the moments of Boltzmann equation and find $\omega_Q^{cl}(m = \pm 2) = 2\omega_r$. It should be stressed that in this limit the expansion 4.13 no longer holds but the Boltzmann approach is still valid.

Quadrupole modes with $m = \pm 1$ are described by a velocity field $\mathbf{v} \propto \nabla(xy)$ and exhibit a scissor like motion, meaning an oscillating deflection of the elongated cigar-shaped system around the z axis. Following equation 4.15 one immediately obtains $\omega_Q^{hd}(m = \pm 1) = \sqrt{\omega_r^2 + \omega_z^2}$ in the hydrodynamic limit. Evaluating the determinant equation for the collisionless limit yields two frequencies $\omega_Q^{cl}(m = \pm 1) = |\omega_r \pm \omega_z|$. Again in the collisionless limit the scissors modes are no longer meaningful eigenmodes of the system.

[6] $\left(\omega_Q^2 - 4\omega_r^2\right) + \frac{i\omega_r}{\tau}\left(2\omega_r^2 - \omega_Q^2\right) = 0$

	hydrodynamic	collisionless
dipole modes $(l = 1, m = \pm 1)$	$\omega_D = \omega_r$	$\omega_D = \omega_r$
scissors modes $(l = 2, m = \pm 1)$	$\omega_Q = \sqrt{\omega_r^2 + \omega_z^2}$	$\omega_Q = \lvert\omega_r \pm \omega_z\rvert$
radial quadrupole modes $(l = 2, m = \pm 2)$	$\omega_Q = \sqrt{2}\omega_r$	$\omega_Q = 2\omega_r$
radial compression modes $(l = 0, m = 0 \leftrightarrow l = 2, m = 0)$	$\omega_{comp} = \sqrt{2(\gamma + 1)}\omega_r$	$\omega_{comp} = 2\omega_r$

Table 4.1: **Frequencies of collective modes** The labelling in terms of l and m refers to the expansion of the collective modes 4.13 in spherical harmonics with respective angular components. For $m = 0$ the axisymmetric potential entails a coupling between the $l = 0$ and $l = 2$ modes whose superposition again describes an eigenmode of the system. The list is not complete as more modes exist.

In the presence of an axisymmetric trap (as opposed to a spherical trap) the $l = 2$, $m = 0$ quadrupole as well as the $l = 0$, $m = 0$ monopole modes couple and are consequently no longer eigenmodes of the system. However their superpositions are eigenmodes that can be described by the velocity field $\mathbf{v} \propto \nabla \left[a(x^2 + y^2) + bz^2\right]$. Since the velocity field is symmetric with respect to the major axis their dynamics are solely described by the expansion and contraction in the radial and axial direction which justifies their name as compression or breathing modes. The in-phase breathing mode is characterised by a simultaneous compression in the radial and axial direction whereas for the out-of-phase breathing the gas is compressed in the radial direction while expands in the axial direction and vice versa. In the hydrodynamic limit the frequency of the radial compression mode is given by $\omega_{rad.comp}^{hd} = \sqrt{2(\gamma + 1)}\omega_r$. Due to the compressional character the frequency of the mode now depends on the equation of state which relates pressure p and density ρ. Here we assumed a polytropic relation $p \propto \rho^{\gamma+1}$ between the two quantities with the power-law coefficient γ. In the collisionless limit one again finds $\omega_{comp}^{cl} = 2\omega_r$ for both modes. Figure 4.1 schematically shows the motions of the low-lying collective modes with their respective frequencies summarised in table 4.1.

Since compression modes explicitly probe the equation of state, bulk properties such as compressibility or bulk viscosity can be determined by its measurement. The compressional character of these modes also manifests itself in a non-vanishing divergence of the velocity field $\mathbf{v}$. The radial quadrupole mode on the other hand is a pure surface mode whose divergence of the velocity vanishes[7]. Since the divergence free modes do not depend on the internal bulk properties[8] but explicitly evaluate the shearing response, they act as an excellent probe to study hydrodynamics. [63] Hence the surface-like radial quadrupole mode ($l = 2, m = \pm 2$) will be the central element in the experimental study of hydrodynamics presented in section 4.2. It should be stressed that hydrodynamic behaviour does not imply superfluidity. Hydrodynamics can occur both above and below the transition temperature for a superfluid and in particular the hydrodynamic equations are identical for superfluid and inviscid, classical collisional hydrodynamics under the current considerations. [32] How superfluidity can still be probed using collective modes will be discussed in section 5.3.

Only in the hydrodynamic limit the collective modes exhibit a simple mode structure with frequencies that can be calculated analytically. However, when deviating from this limit by for example allowing for finite relaxation times the modes described above are

[7] $\nabla \cdot (\nabla(x \pm iy)^2) = 0$

[8] if interactions are weak and treated in a mean-field approach.

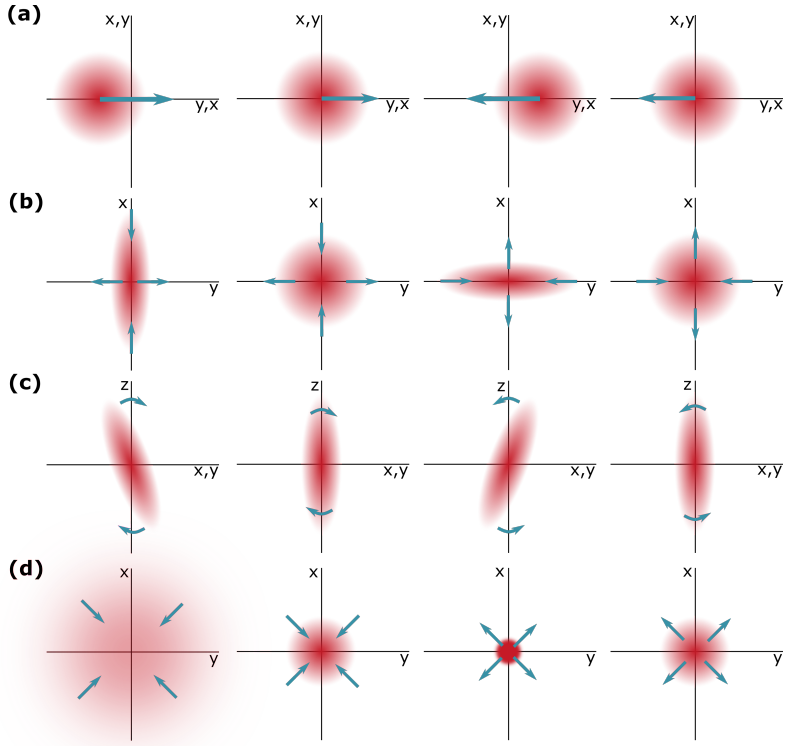

Figure 4.1: **Motion of collective modes in the hydrodynamic limit** (a) Radial dipole modes ($l = 1, m = 0$) (b) Radial quadrupole mode ($l = 2, m = \pm 2$). The second quadrupole mode is turned by 45°. (c) xz and yz scissors modes ($l = 2, m = \pm 1$) (d) Radial breathing mode as a consequence of the coupling between the $l = 0, m = 0$ and $l = 2, m = 0$ modes. The blue arrows schematically depict the movement of the system and the respective densities are not to scale.

no longer necessarily eigenmodes and one has to fall back to the Boltzmann approach. Also this approach looses its validity if the interaction cannot be treated in a mean-field picture anymore. Various theoretical techniques [70, 73, 74] have been developed to include corrections for the neglected kinetic energy rendering the correct description increasingly difficult. One important correction is the so called sum rule approach [73]. It treats the effects of the kinetic energy that has been neglected in the hydrodynamic limit by perturbatively expanding to first order in the ratio between the kinetic and harmonic oscillator energy. For the radial quadrupole mode this correction yields [30]

$$\omega_Q(m = \pm 2) = \sqrt{2}\omega_r \left(1 + \frac{E_{kin}}{E_{ho}}\right)^{\frac{1}{2}} \tag{4.16}$$

In fact the sum rule approach also includes the collisionless result $\omega_Q^{cl}(m = \pm 2) = 2\omega_r$ in the absence of any interaction when $E_{kin} = E_{ho}$.

As discussed above this simple description of collective modes only applies in limiting cases. Hence, we expect the theory to recover some of the qualitative features of the excitation spectrum, while others may not be understood by treating the system macroscopically. In this case, only a full microscopic treatment in terms of collective quasi-particle excitations in the presence of a trapping confinement has the potential to correctly describe all features.

4.1.3 Finite size effects

In the description presented above we assumed a macroscopic system or at least that the respective macroscopic quantities are well defined. But when the number of particles is reduced drastically the macroscopic description looses its validity and the finiteness of the system plays an important role. If the system can locally be approximated by the homogeneous system then the local density approximation (LDA) can be applied. In this case the energy density of the trapped gas is locally given by the energy density of the homogeneous system and the kinetic energy term can be neglected. The condition in which the LDA holds is referred to as the Thomas-Fermi limit which is formally given by [63]

$$\frac{Na}{a_{ho}} \gg 1 \tag{4.17}$$

where N is the particle number, a the scattering length and a_{ho} the harmonic oscillator length. The Thomas-Fermi approximation can also be derived more rigorously in the context of Bose-Einstein condensates where it emerges as a consequence of the neglected kinetic energy pressure term, but thinking of it in terms of locally homogeneous system provides a more general picture. Interestingly, the approximation finds its classical analogue in the hydrodynamic assumption that the molecular mean-free path is much smaller than the system size and the system is in local thermodynamic equilibrium. [75]

However for our small deterministically prepared systems the confinement energy will be in the order of the Fermi energy and the approximation of well separating energy and length scales no longer holds. Hence we expect deviations from the LDA depending on the choice of interaction parameters and number of particles. At unitary ($\eta = 0$) however the average interatomic distance sets the only length scale in the system. Consequently, it can be assumed that at unitarity hydrodynamics can be applied for all wavelengths larger than the inverse Fermi wave vector k_{F}^{-1}. While the presence of a trapping potential modifies this condition by the introduction of the additional length scale, hydrodynamic theory is most successful close to unitarity. [32, 63]

In classical finite-size systems another interesting phenomena occurs. In a confined system the number of particles sets an upper bound for the number of collective modes via number of degrees of freedom. Consider for example a mass-spring chain of N particles, which are coupled with equal spring constants. The system is assumed to be trapped in a box by imposing hard walls on either side of the container, which the last spring is connected to. Then, there are only a finite number of collective oscillations or normal modes that can be excited. Similarly, the number of normal modes of molecular vibrations are also bound by the degrees of freedom giving rise to the classical stretching and bending motions associated with vibrational excitations. [76] The application of this classical expectation to collective modes in mesoscopic cold quantum gases remains unclear and requires further exploration.

4.2 Observation of the quadrupole mode in a mesoscopic quantum system

Surface modes, and in particular the radial quadrupole mode, are well suited to study the applicability and limits of hydrodynamic theory, as they directly probe the shearing response of the system. [63] Our finite-size system with free tunability of the particle number offers an ideal test bed to study the connection between the macroscopic picture of a collective motion to the breakdown of hydrodynamics where microscopic effects become important. In this chapter the experimental observation of the radial quadrupole mode in a mesoscopic Fermi system is presented.

4.2.1 Experimental sequence

The starting point for the experiment will be a deterministically prepared system of $N+N$ atoms in the fermionic ground state of the Gaussian potential after the spilling procedure described in section 2.1.3. The entire experimental sequence is schematically depicted in figure 4.3. Independent of the number of atoms prepared, the optical power of beam 1 is ramped back up to the pre-spilling value to keep the trap depth and trap frequencies the same for all atom numbers ensuring the comparability of the measurements. The Gaussian beam shape translates to a cigar-shaped optical potential (compare section A.2) which is characterised by a radial trap frequency of $\omega_r = 2\pi\times(27.3\pm0.1)$kHz and an axial frequency of $\omega_z = 2\pi \times (4.09 \pm 0.02)$kHz. The former was derived from the sloshing motion in the trap (see figure 4.4), whereas the latter has been obtained via amplitude modulation (see figure A.2). The corresponding ratio $\lambda = \frac{\omega_z}{\omega_r} \approx 1/6.7 \ll 1$ between axial and radial trap frequency justifies the assumption of an axisymmetric trap in the theoretical derivation of collective modes.

The actual experiment starts after the deterministic sample of $N + N$ atoms has been prepared and the optical power is restored to the pre-spilling value. Within 15ms we ramp the magnetic offset field to the desired value B where the quadrupole excitation should be performed. By changing the magnetic offset field we effectively tune the interparticle scattering length a and thereby the binding energy between $E_B = 0.2...3.1\hbar\omega_r$. All two-body binding energies given in this thesis are calculated numerically for our trap geometry following reference [77]. Since we are starting at the high field side of the Feshbach resonance, at 800G, the scattering length remains negative and the interaction will be attractive (see figure 2.6). When adiabatically ramping over the Feshbach resonance the atoms follow the molecular branch and form bosonic molecules. Albeit their attractive interaction, fermions still obey the Pauli exclusion principle, which becomes less important the tighter the molecules get and the more the two fermions can be described as a quasi boson. In this framework it seems possible to create arbitrarily tight molecules by ramping down the magnetic field, however the lifetime decreases due to three-body losses which limit the minimum magnetic field to about 630G ($E_\mathrm{B} \sim 3\hbar\omega_r$) for our small systems. To compensate for the gravitational drag we additionally apply a slight axial gradient of 0.56G/cm by adjusting the relative current through the coils[9]. Due to the small mass of ^{6}Li however, the gravitational correction is minuscule and further gravitational effects can be completely neglected throughout the experiment.

To extract the many-body excitation spectrum we introduce a periodic perturbation $\hat{H}_Q(t) = \hat{H}_Q(t+T)$ with an excitation frequency $\Omega = 1/T$ for a given number of cycles n. If the perturbation frequency is sufficiently close to a resonance[10] of an allowed transition to another many-body quantum state $|e\rangle$ within the accessible Hilbert space the system will be excited with a finite transition probability depending on the coupling strength $\langle e|\hat{H}(t)|g\rangle$. The resulting deviation from the ground state due to the perturbation can afterwards be measured by spilling a second time to the initial preparation configuration. By changing the modulation frequency Ω we can thereby extract the full excitation spectrum.

Since we intend to excite the quadrupole mode, the respective perturbation operator must exhibit quadrupolar symmetry in the radial direction. In the experiment we achieve the quadrupole perturbation by modulating the shape of the optical potential with the respective frequency. In addition to beam 1, that has been used for parts of the evaporation and deterministic preparation, we now also ramp on the second beam. On the SLM we project two superimposed circular apertures for beams 1 and 2 respectively, where the first aperture only leads to the transformation of the Gaussian beam 1 to the respective airy disk. Within the second aperture we additionally add a second order phase winding which

[9] Observe that this value deviates from the expected value of $dB/dz = mg/\mu_\mathrm{B} = 1.06$G/cm.
[10] in terms of the width of the resonance

transforms the initially LG_0^0 Gaussian beam into an approximately LG_0^2 Laguerre-Gaussian beam[11]. The interference of the two overlapping beams (compare figure 2.5) leads to an elliptical deformation of the Gaussian shape for small powers of beam 2. By periodically modulating the power of the second beam we can periodically change the Gaussian light field into an elliptical light field and back. The direction of the major and minor axis of the ellipse is given by the relative phase alignment between the two beams.

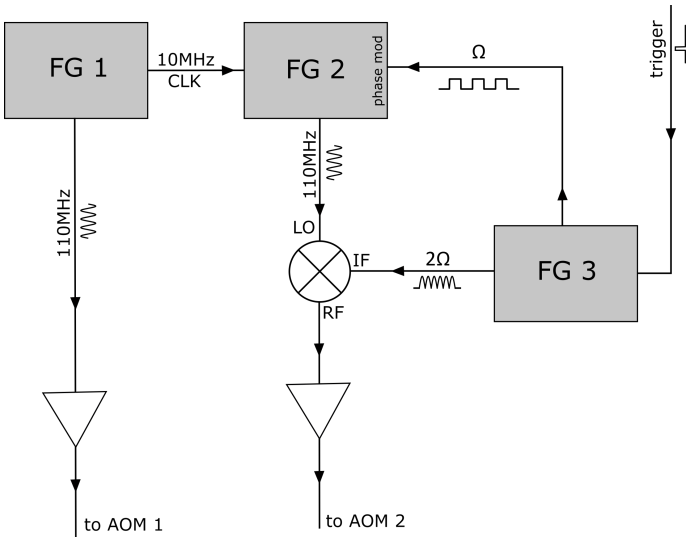

Figure 4.2: **RF setup** Two arbitrary waveform generators (FG 1 and FG 2) provide the 110MHz signal to drive the AOMs. The second RF frequency is modulated with a n-cycle long absolute sine waveform at 2Ω. By additionally modulating the phase of second 110MHz RF signal with a frequency Ω we achieve an alternating elongation of the intensity profile in the x and y direction in the Fourier plane of the superimposed beams.

Experimentally, beam 1 and beam 2 can be individually tuned by two 110MHz AOMs that are controlled by the RF setup depicted in figure 4.2. A function generator[12] (FG 1) provides the necessary 110MHz sinusoidal driving frequency for the first AOM which leads to the in-coupling into the beam 1 fibre that exists on the setup depicted in figure 2.4. A second function generator (FG 2) is used to provide the 110MHz driving frequency for the second AOM altering beam 2 similarly to beam 1. In contrast to FG1, its output frequency is not directly connected to the AOM, but is instead modulated by a RF mixer[13]. The modulation signal is derived from third frequency generator (FG 3) and has the form of an absolute sine with a frequency of 2Ω with typically $n = 2 \cdot 24$ cycles. This results in a periodic driving of the beam 2 power which translates to the deformation of the Gaussian intensity profile to an elliptically shaped profile and back to a Gaussian with a frequency of 2Ω. To achieve an alternating elongation in the x and y direction the phase of the RF signal of the second beam is jumped between 0 and π at a frequency Ω. The 10MHz clocks of the two function generators providing the RF are synchronised to ensure the relative phase stability. The start of the quadrupole oscillation burst is triggered digitally by the experimental control software.

Together, this setup generates the desired quadrupole oscillation of the light field in the Fourier plane of the SLM with a frequency of Ω. For low frequencies $\Omega < 10$Hz we can

[11] Due to the finite aperture the actual outgoing beam will be a convolution of the LG_0^2 and an airy disk of respective aperture radius.
[12] RIGOL DG4162 Arbitrary waveform generator
[13] Mini-Circuits Frequency mixer ZX05-5-S+

confirm on the camera that the intensity indeed performs the desired quadrupole motion. Although we could in principle trigger the image acquisition and thereby also confirm the quadrupole oscillation for high frequencies, the experimentally relevant frequencies Ω exceeds the inverse of the exposure time and hence we would only capture an average image. For high frequencies ($\sim$ 10kHz), the correct behaviour and frequency of the beam 2 power can be confirmed by monitoring the power on a photodiode both before and behind the SLM. For low frequencies ($\sim$mHz-Hz) we have observed phase fluctuations manifesting themselves in random changes of the angle of the ellipse. Given their slowness and random character, these phase fluctuations can most likely be traced back to temperature fluctuations of the high-power fibres and become irrelevant on the short timescales of the quadrupole perturbation of a few hundred micro seconds. Since the frequency of the perturbation is in the same order as the 400kHz PID loop an active stabilisation of the absolute sine modulation in not feasible and instead we only ramp the power to fixed value. The perturbation leads to an increase in power by approximately 5% measured on the photodiode after the SLM. While in the radial direction the interference and elongation do not alter the average trap strength, a small compression is performed in the axial direction.

Under the perturbation the initial system in the ground state will increasingly populate an excited many-body quadrupole mode. After the perturbation has been switched off, we adiabatically ramp the magnetic offset field back up to 800G. The finite population of the excited quadrupole mode should now manifest itself in the occupation of higher excited levels of the harmonic oscillator. Spilling a second time to the initially prepared configuration removes the atoms occupying these higher levels. The remaining atoms are counted in the μMOT (see section 2.3.1) where excitations reveal themselves in atom loss. By repeating the experimental sequence we statistically sample the probability distribution for each chosen values of Ω to measure the expectation value of the number operator $\langle \hat{N} \rangle$ and obtain the full excitation spectrum.

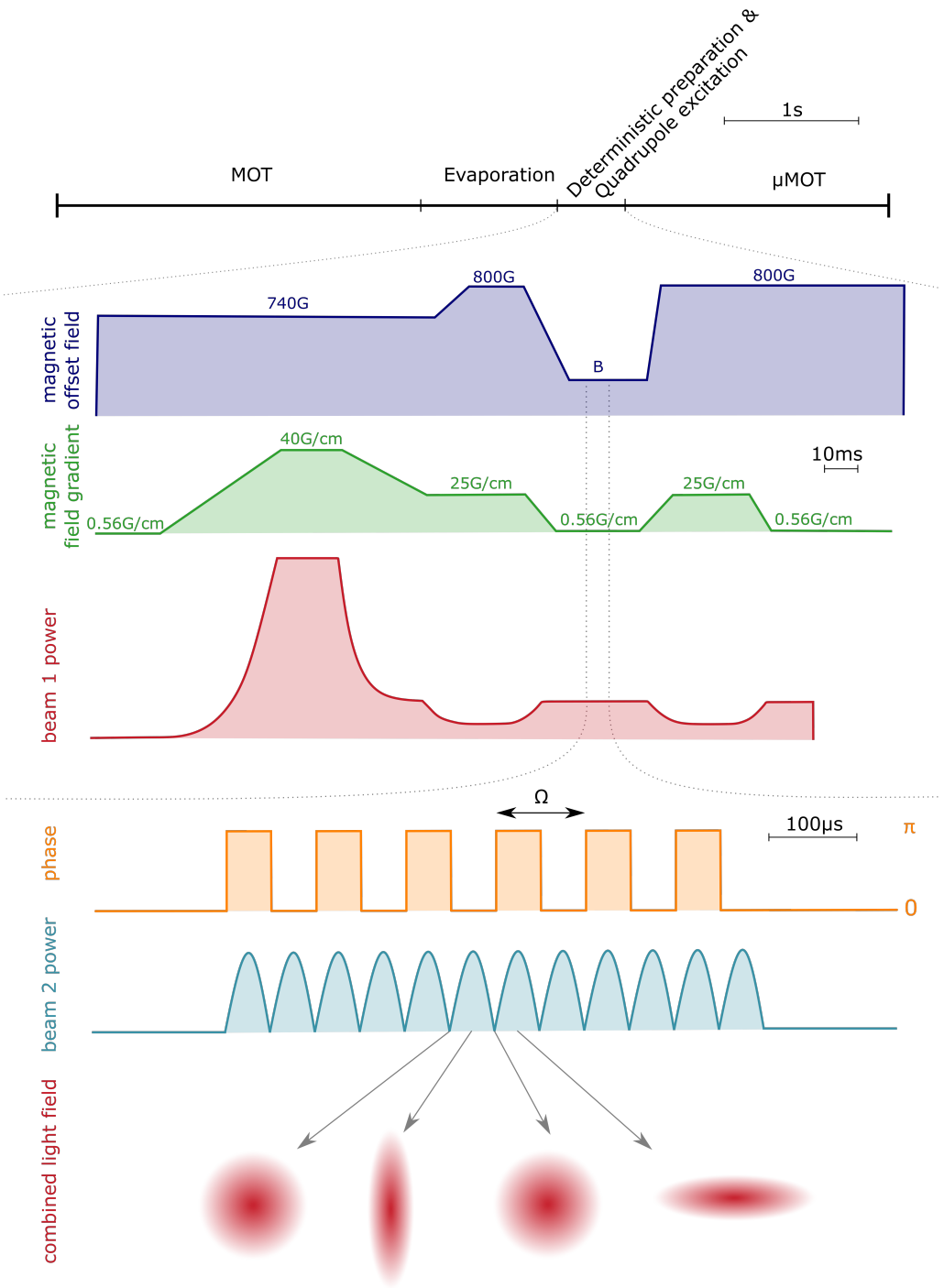

Figure 4.3: **Experimental sequence on different time scales** After the deterministic preparation of the $N + N$ ground state the magnetic offset field is ramped to probe a corresponding interaction strength. The quadrupole oscillation is achieved by modulating the power of the second beam in an absolute sine fashion at a frequency of 2Ω and simultaneously jump the phase with a frequency of Ω. A second spill projects the final state back onto the ground state. An occupation of higher levels of the harmonic oscillator potential with respect to the ground state manifests itself in atom loss that can be detected by counting the remaining atoms in the μMOT.

4.2.2 The non-interacting case

Before we start exploring the physics of collective modes, which are inevitably connected to the interaction between individual constituents, we record the reference spectrum for the non-interacting case. Experimentally this is achieved by preparing the $1+1$ system using the deterministic preparation scheme presented in section 2.1.3 and tuning the magnetic offset field to the zero crossing of the scattering length at $B = 568$G. Measuring the average atom number after 24 quadrupole cycles for excitation frequencies between $\Omega = 2\pi \times 10$kHz and $\Omega = 2\pi \times 65$kHz yields the non-interacting excitation spectrum shown in figure 4.4.

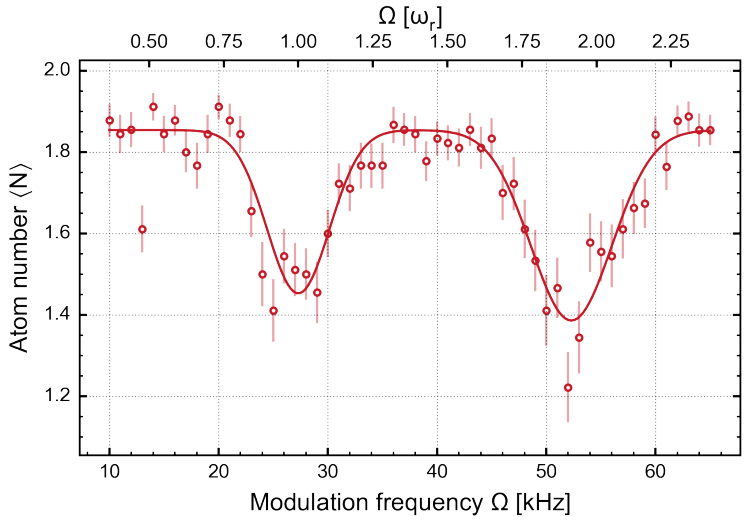

Figure 4.4: **Non-interacting quadrupole spectrum** After preparing 1+1 atoms at the zero crossing of scattering length at 568G we vary the quadrupole modulation frequency Ω and record the average atom loss after 24 driving cycles. Each data point corresponds to the average atom number derived from 90 experimental runs with the standard error of the mean represented by the error bar.

The spectrum features two distinct peaks at $\Omega_1 = 2\pi \times (27.3 \pm 2.9)$kHz and $\Omega_2 = 2\pi \times (52.3 \pm 3.7)$kHz where the second value denotes the width of the resonance derived from a Gaussian fit. The first resonance can be identified with a centre-of-mass oscillation with a frequency of ω_r. In an ideal experiment we would not expect to observe such a sloshing motion, as it implies that the atoms either experience an anisotropic trapping potential or that the quadrupole perturbation is asymmetric. Possibly, beam 1 and beam 2 do not perfectly overlap in the atom plane, or the remaining aberrations lead to deviation from the radial symmetry albeit our efforts to cancel them as explained in section 3. In fact, we measured a slight anisotropy of 4% even after the aberration correction (see section 3.2.2) and also observe a double peak feature on the dipole resonance obscured by the Gaussian fit in figure 4.4. The second dominating peak is located at approximately $\Omega \approx 2\omega_r$ and can consequently be identified with the allowed parity-conserving $E_{0\to 2}$ transition in the Gaussian potential. The modulation of the total power due to the additional perturbation beam leads to the excitation that results in the observed atom loss. The outlier at $\Omega \approx 0.5\omega_r$ can presumably be traced back to the excitation scheme, where a small power difference between the individual absolute sine periods in combination with a relative beam displacement could lead to a centre of mass motion with a frequency of 2Ω. But since the amplitude and width is comparatively small and the resonance is well separated in energy with respect to the dynamics of interest, its contribution can be neglected in the following.

Furthermore, the non-interacting measurement allows us to determine the anharmonicity

defined by the energy difference of the $E_{0\to1}$ and $E_{1\to2}$ transition in the Gaussian potential according to

$$\frac{E_{0\to1} - E_{1\to2}}{E_{0\to1}} = 2 - \frac{\Omega_2}{\Omega_1} \approx 8\%. \tag{4.18}$$

For the following discussions we define the frequency of the sloshing mode as the radial trap frequency ω_r.

4.2.3 The many-body limit

Experimentally, we start exploring the many-body limit by preparing $80 + 80$ atoms and measuring the average atom number after the quadrupole excitation for modulation frequencies between $\Omega = 2\pi \times 10$kHz and $\Omega = 2\pi \times 70$kHz and a certain offset magnetic field B. The right plot in figure 4.5 shows such a single spectrum for an offset field of $B = 676$G. We vary the magnetic field between 636G and 1000G and record a sequence of spectra, which can be stacked to the combined left plot in figure 4.5. It depicts the change of the spectrum when varying the dimensionless interaction parameter $\eta = 1/(k_\mathrm{F}a)$ across the BEC-BCS crossover, where each column corresponds to a single spectrum. It should be pointed out, that the width of the columns does not reflect the uncertainty of the interaction parameter but is an artefact of the limited scanning resolution[14].

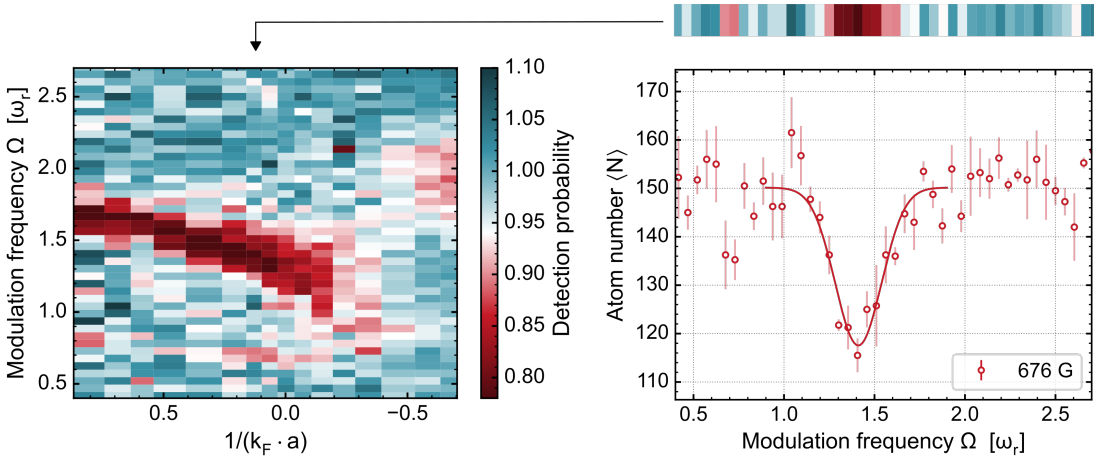

Figure 4.5: **Quadrupole excitation spectrum across the BEC-BCS crossover for 80+80 atoms** Each column in the left plot corresponds to an atom-loss spectrum comparable to the one for $B = 676$G depicted on the right. The reduced atom number on the resonances is indicated in red in contrary to the unaffected atom number elsewhere represented in blue. As the interaction parameter $\eta = 1/(k_\mathrm{F}a)$ and binding energy decreases further towards the BCS side, we observe a downshift of the quadrupole frequency accompanied by a broadening of the resonance. At around $\eta \approx -0.35$ the spectrum exhibits a "jump" to a collisionless branch where the resonance frequency is $\Omega \approx 2\omega_r$. Far in the BEC regime we are experimentally limited by three-body losses manifesting themselves in an overall reduced atom number.

The most prevalent feature of the spectrum is a broad resonance for positive interaction parameters (red atom loss in the left plot in figure 4.5). On the basis of the symmetry of the

[14] Each data point represents the mean atom number derived from 30 experimental repetitions. Given the experimental cycle rate of 5.3 seconds, taking a single spectrum takes about two hours.

quadrupole perturbation operator we argue that the resonance results from the excitation of the celebrated radial quadrupole mode. Only at around $\eta \approx 0.13$ the measured resonance frequency $\omega_Q^{exp} = (1.41 \pm 0.01)\omega_r$, which has been derived from a Gaussian fit shown in figure 4.5, coincides within one standard deviation with the theoretical expectation of $\omega_Q^{th} = \sqrt{2}\omega_r$. Since the quadrupole mode with its surface character explicitly probes hydrodynamic shearing and the deviation is less than 1% with respect to the theoretical value expected for the purely hydrodynamic regime, we interpret the measurement result as an indicator for the potential hydrodynamic behaviour of the system in this interaction regime. As the interaction parameter η is increased the mode frequency departs from the hydrodynamic value and shifts upwards towards the collisionless value of $\omega_Q^{th} = 2\omega_r$ far in the BEC limit. Above $\eta = 0.5$ corresponding to a binding energy of $E_B \approx 2\omega_r$ we are experimentally limited by three body losses, which also manifest themselves in a generally reduced atom number independent of the modulation frequency. To account for the atom losses we normalised the excitation spectrum with respect to the detection probability as opposed to the initial preparation atom number. Throughout the majority of the spectrum the resonance frequency of the quadrupole mode is not constant and most likely depends on the equation of state implying that the pure surface-like character of the mode is lost. For large positive interaction parameters the transition between the hydrodynamic and collisionless regime is continuous[15] as there is no phase transition involved. Below $\eta = 0.13$ the resonance frequency shifts even further down than the theoretical minimum of $\sqrt{2}\omega_r$ (grey dashed line) which renders this region around unitarity one of the most peculiar parts of the spectrum. On the BCS side at $\eta < -0.35$ the mode seems to vanish and the resonance frequency instead jumps to a value of $\Omega \approx 2\omega_r$. This agrees well with the expectation that the small binding energies are not sufficient to support the collective quadrupole mode, which instead is found in the collisionless branch.

Apart from the resonance frequencies we also extract the damping from the width of the Gaussian fit of the resonance shown in figure 4.6. For consistency we follow the same notation as other authors [6, 31] and choose to express the damping in terms of an exponential damping rate κ of the quadrupole oscillation assuming the latter follows

$$\langle x \rangle \sim e^{-\kappa t} \cos(\omega_Q t). \tag{4.19}$$

From the width σ of the Gaussian fit we calculate the factor $Q = \omega_Q / \Delta\omega_Q$ taking into account that the relation between the full width at half maximum and the standard deviation is given by $\Delta\omega_Q = 2\sqrt{2\ln 2}\sigma$. The Q factor is directly related to the damping rate via

$$\kappa = \frac{\omega_Q}{2Q} = \sqrt{2\ln 2}\sigma. \tag{4.20}$$

Across a wide range in the BEC regime where $\eta > 0$ we observe a comparatively small damping rate, whereas it increases rapidly on the BCS side before it drops again for $\eta < -0.5$. The rapid increase in the damping coincides with the downbending of the branch below the hydrodynamic prediction and sudden jump in resonance frequency. Since the width of the resonance may be altered by amplitude broadening effects, it only constitutes an upper limit for the damping. Hence, we waive a quantitative analysis and focus on the qualitative comparison instead.

Comparison with experiment

Although we suggestively referred to 80+80 atoms as the many body limit, the atom number is still two orders of magnitude smaller than in a comparable experiment performed

[15] to the precision of our measurement

by Altmeyer et al. [6]. As a consequence we find in addition to few similarities also significant qualitative and quantitative deviations, which require further discussion and hint at how the system size affects the mode. Figure 4.6 shows the fitted quadrupole resonance frequencies (red) and damping rates (blue) of our measurement and the data (black) obtained by Altmeyer et al. for comparision. Compared to our experiment, the larger system

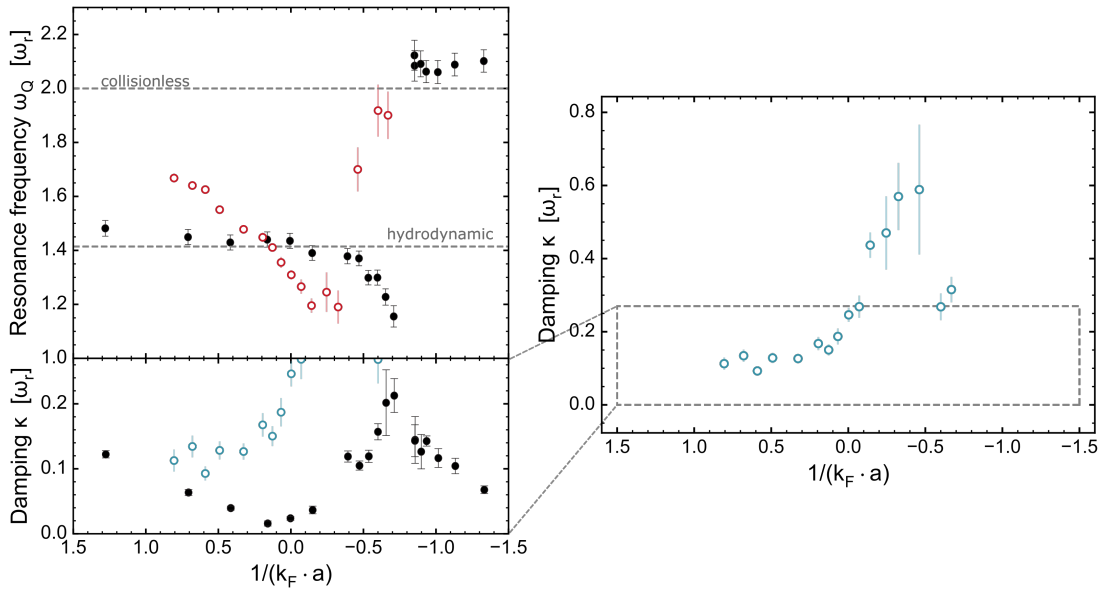

Figure 4.6: **Comparison of the resonance frequencies and damping across the BEC-BCS crossover** The fitted quadrupole resonance frequencies (red circles) and corresponding damping rates (blue circles) in our system of $N = 80 + 80$ atoms exhibit significant deviations from the results obtained by Altmeyer et al. [6] (black points), who studied the radial quadrupole mode for $N = 4 \times 10^5$ atoms. Although we also observe a downshift of the resonance frequency below the hydrodynamic result towards the BCS regime which is accompanied by an increase in the damping, the downshift occurs for higher interaction parameters in our case. Since our damping rates are extracted from the resonance widths they constitute an upper bound and are significantly larger than the results obtained by Altmeyer et al. [6]. The error bars indicate the standard error of the mean.

size in the Altmeyer et al. study permits much higher Fermi momenta and consequently can cover a wider range of interaction parameters. Our study on the other hand shows the qualitative features "squeezed" on a smaller range of interaction parameters. In particular, they also observed a down-shift of the quadrupole resonance frequency below the hydrodynamic prediction of $\sqrt{2}\omega_r$, but in their system it occurs further on the BCS side at around $\eta \sim -0.75$. Contrary to their macroscopic study we do not observe a stable "hydrodynamic plateau" in the sense, that there exists an extended region where the resonance frequency remains constant at $\omega_Q \approx \sqrt{2}\omega_r$. We only find the predicted square-root of two value between $0.15 < \eta < 0.25$ and hence recover the purely hydrodynamic result in a much smaller regime. Outside of this interaction range however, the theory of ideal hydrodynamics cannot explain the measured collective frequencies.

Most likely, only a combination of different effects can explain the discrepancy between our data and the results obtained by Altmeyer et al. In our system the interaction strength at which the quadrupole mode frequency exhibits the jump occurs closer to unitarity, whereas the mode extends further into the BCS limit in the large system of Altmeyer et

al. containing $N = 4 \times 10^5$ atoms. One explanation for the found discrepancy could be the significantly higher temperature of the sample of $T \leq 0.1T_F$ compared to our system[16]. However, it seems unlikely that a higher temperature stabilises the mode, such that it extends further into the BCS regime, where the binding energy is significantly smaller. More plausibly, the shifted disappearance of the quadrupole mode is associated to the reduced Fermi energy with respect to the confinement energy of the harmonic trap in our system. Altmeyer et al. report a Fermi energy of $E_F = 41.7\hbar\omega_r$ [6], whereas the Fermi energy in our system is approximately an order of magnitude smaller $E_F = 4.3\hbar\omega_r$ and in particular in the same order as the confinement energy. In a system with a smaller Fermi energy, the phononic branch, which is expected to extend to about the Fermi momentum [63] is accordingly shorter and the system cannot even host the lowest frequency phononic excitations such as the quadrupole mode.

The evolution of the damping rate across the BEC-BCS crossover displays qualitative similarities to the Altmeyer et al. study, as for example the strong increase towards the BCS side during the downshifting below the hydrodynamic $\sqrt{2}\omega_r$ resonance frequency. However our data does not reproduce the increase in damping deep in the BEC limit, which may either not exist in our system or be shadowed by the amplitude broadening. In the macroscopic limit the increased damping far in the BEC side can be understood as an increased susceptibility to heating by inelastic processes [6]. Deep in the BCS regime for $\eta < -0.5$, the damping of the collisionless resonance decreases again, but stays above the resonance widths of the collective branch, which is comparable to the qualitative evolution found by Altmeyer et al.

Comparison with theory

To explain the unexpected behaviour of the shifting quadrupole resonance frequency and sudden "jump", multiple theoretical models have been developed, which shall be discussed in the following.

The square-root of two value for the resonance frequency of the quadrupole mode is only obtained in the ideal hydrodynamic limit where changing interactions have been neglected. Obviously, the change of interactions across the BEC-BCS crossover plays an essential role in the description of the system, which can be treated in a first-order correction. Menotti et al. [78] derive a theoretical expression for the resonance frequency of a normal Fermi gas in a mean-field approach using the local density approximation (LDA). The effect of interactions is parameterised in the ratio $\chi = E_{int}/E_{ho}$ between the interaction and harmonic oscillator energy. From a virial theorem of the form

$$2E_{kin} - 2E_{ho} + 3E_{int} = 0 \tag{4.21}$$

it can be shown [7] that the interaction ratio is approximately $\chi \simeq 0.3k_F a = 0.3\eta^{-1}$ for trapped Fermi gases with Fermi momentum $k_F = \sqrt{2m(3N)^{1/3}\omega_{ho}/\hbar}$. Expanding the semi-classical Landau-Vlasov equation [78], which is comparable to the Boltzmann equation 4.6, in terms of this ratio and solving it using a scaling ansatz yields a mean-field quadrupole frequency

$$\omega_Q = 2\omega_r\sqrt{1 - \frac{3}{4}\chi} = 2\omega_r\sqrt{1 - \frac{3}{4}\cdot 0.3\eta^{-1}}. \tag{4.22}$$

Although they derived this result for the quadrupole frequency for the case of a spherical trap ($\omega_r = \omega_z$), the equation still holds for an axisymmetric ($\omega_r \neq \omega_z$) trap. The congruence is explained by the symmetry of the quadrupole motion oscillating only in the

[16] As described in section 2.1.3 the definition of a temperature is meaningless in our small systems. However given our small atom number fluctuation, the entropy per particle is likely smaller than in the macroscopic system by Altmeyer et al.

isotropic x-y plane, but being decoupled from the axial direction. The breathing mode frequency on the other hand would be affected by a change in symmetry, since its description explicitely requires a coupling to the axial degree of freedom. The result matches the sum-rule approach from equation 4.16 after rearranging the virial theorem 4.21 for the kinetic energy. When applying the sum rule approach in its original form 4.16, one would expect the quadrupole frequency to always be larger than $\sqrt{2}\omega_r$. An ideal fluid would consequently exhibit the smallest resonance frequency since the kinetic energy cannot be negative. However through the energy balance equation 4.21 the resonance frequency can undercut the ideal fluid result.

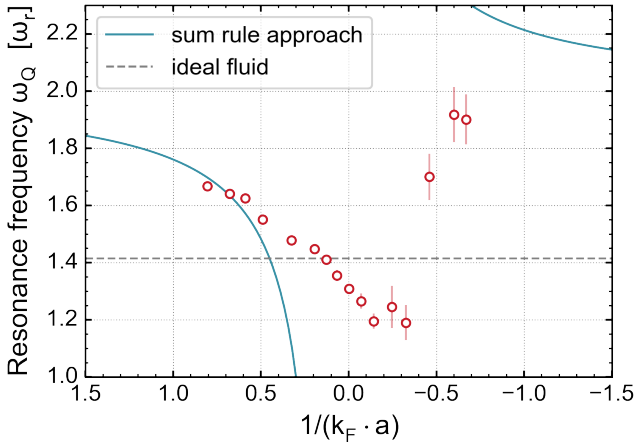

Figure 4.7: **Comparison of resonance frequencies with theory** A simple mean-field correction following the sum-rule approach fails at explaining the observed resonance frequencies (red circles). The ideal fluid result is only recovered in a very small regime of interaction parameters where $0.15 < \eta < 0.25$. A better theoretical model including microscopic dynamics is required to explain the experimental findings.

The mean-field model 4.22 for the quadrupole frequency is plotted in figure 4.7 and shows a very poor agreement with the measured quadrupole frequency for $80+80$ atoms in our experiment. While it recovers the downshift of the mode frequency towards unitarity qualitatively, it completely fails at describing it quantitatively. Due to the parameterisation of the interaction parameter being inversely proportional to the scattering length, the model predicts a divergence of the resonance frequency at unitarity. However, we observe the survival of the mode in the weak BCS regime and hence the downbending branch explicitly crosses the point of divergence. Deeper in the BCS regime the sum rule approach correctly predicts a mode frequency, which in the limit of $\eta \to -\infty$, tends to the collisionless value of $2\omega_r$. This leads us to conclude that the observed phenomenon is neither simply explained by a normal Fermi gas in a mean-field LDA approach, nor an ideal fluid in the hydrodynamic limit [78, 79] and thus encourages further theoretical investigation.

Urban et al. [80] analysed the radial quadrupole mode across the BCS normal to superfluid phase transition using quasiparticle transport theory. Their theoretical results suggest that the downshift below the ideal fluid result may be explained by the coupling of two modes, the hydrodynamic mode on the BEC side and the normal gas mode with $2\omega_r$ in the collisionless BCS regime. Both modes naturally repel each other due to their coupling similar to an avoided crossing. In their simulations the collisionless mode is driven by thermally excited quasi particles, which behave like a normal gas and hence oscillate with a frequency of $2\omega_r$. This suggests that a theoretical description of our results of the

mesoscopic system requires the inclusion of microscopic dynamics outside of the validity of LDA. Quasi-particle transport theory [80] or the quasi-particle random phase approximation method [81] hold the promise to better describe the observed spectra. Alternatively, if the equation of state is known for the system under investigation across the entire BEC-BCS crossover, the collective frequencies can be calculated numerically [74, 82, 83] from the former. Due to the numerical expense and complexity associated with these methods such a simulation is infeasible within the framework of this thesis and theorists are encouraged to support a better theoretical description.

The correct interpretation of the measured damping rates and underlying microscopic processes remains a matter of current discussion with theorists [84]. It was suggested to extract the damping rates across the entire BEC-BCS crossover and deduce respective upper limits for the shear viscosity [84]. One plausible explanation for the increased damping is the break-up of pairs into single fermionic excitations which would act similarly to scattering defects [85].

4.2.4 Emergence of a collective mode in the few-body limit

The poor agreement between our experimental results and the theoretical predictions or previous macroscopic studies raises the necessity for a better insight into the microscopic processes related to the excitation of collective modes and their emergence in the few-body limit. Fortunately, our system and preparation scheme provides us with the required ability to deterministically reduce the atom number and access microscopic properties.

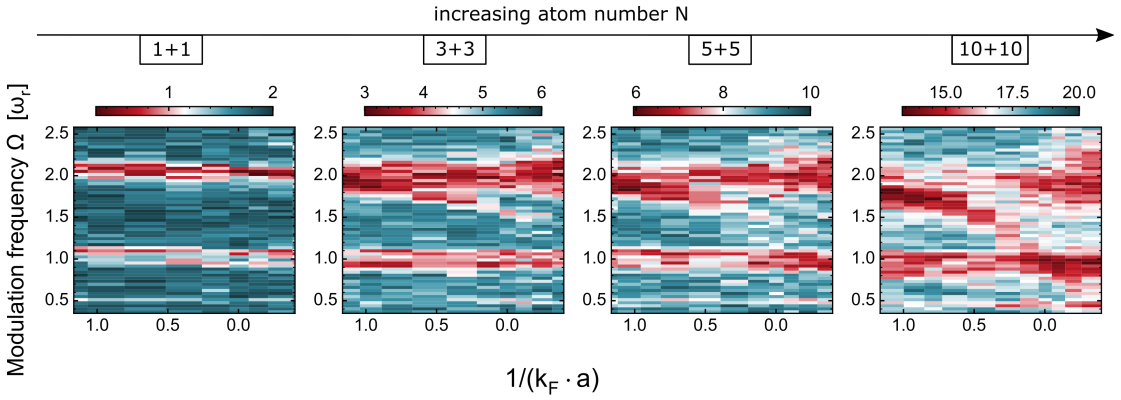

Figure 4.8: **Emergence of the quadrupole mode** In the two-body limit the quadrupole excitation spectrum is dominated by the confinement. By deterministically increasing the atom number we witness the separation of the collective quadrupole mode as a downbending interaction dependent branch. In the case of $10 + 10$ atoms the mode is fully developed and approaches the interaction independent dipole mode at $1\omega_r$ before exhibiting a jump into the collisionless branch at $2\omega_r$. The colour bar representing the total atom loss is re-scaled to support the visibility.

Following this approach, we deterministically prepare systems of 1+1, 3+3, 5+5 and 10+10 atoms and record spectra across the BEC-BCS crossover for interaction strengths between $-0.4 < \eta < 1.2$ and a total of 24 excitation cycles. The result is presented in figure 4.8. For the two-body system with 1+1 atoms the two frequencies at $\Omega \approx 1\omega_r$ and $\Omega \approx 2\omega_r$ do not vary across the crossover, which is reminiscent of the non-interacting case. However, the higher energy resonance frequency is up-shifted by approximately 7%[17] with respect to the expected non-interacting value of $2\omega_r$. This could be explained by the anharmonicity

[17] obtained with a Gaussian fit

of the Gaussian potential, which can couple the relative and centre-of mass motion leading to an interaction induced offset shift. For 3+3 atoms we observe the emergence of an additional interaction-dependent branch which departs from the $E_{0\to2}(\Omega = 2\omega_r)$ resonance at around $\eta \sim 0.5$ and extends to about $\eta \sim -0.2$. Its maximum deviation of $0.5\omega_r$(at $\eta \sim -0.2$) from the $2\omega_r$ resonance is less than the single-particle gap of ω_r, which can be interpreted as a clear signature for a collective interaction effect. At that moment we are witnessing the birth of the quadrupole mode. In addition, both the $2\omega_r$ resonance as well as the $1\omega_r$ dipole resonance broaden and shift down. For 5+5 atoms the collective branch separates earlier on the BEC side and bends down even further. Moreover, one can surmise the opening of a gap between the BEC and BCS side of the crossover. However, at this particle number the collective branch and the $2\omega_r$ resonance coexist, meaning that for a given interaction strength one can observe both resonances. While on the BEC side the resonance frequency shifts below the $2\omega_r$ value, it remains at $2\omega_r$ from the point where the collective branch separates. For 10+10 atoms we clearly observe the quadrupole mode starting at $1.8\omega_r$ at $\eta \sim 1.2$ on the BEC side and extending all the way down to $1\omega_r$ which is reached at $\eta \sim 0$. As the number of atoms is increased, the relative atom loss is reduced, indicating that the perturbation strength depends on the atom number (compare figure A.3). While the collective branch separates even further there is still a small region of coexistence with the $2\omega_r$ resonance. Although it seems as if the quadrupole resonance frequency shifts below the dipole resonance at $1\omega_r$ further in the BCS regime, the limited statistical confidence does not permit a conclusive statement. In addition, the coupling to the dipole mode at frequencies close to $1\omega_r$ screens the visibility of the collective branch. Surprisingly, the transition from the hydrodynamic to the collisionless regime in the BCS limit is not continuous, but rather exhibits a jump for large enough atom numbers, a behaviour that has already been observed by other authors [6, 31, 65], not only for the radial quadrupole mode but also for the radial breathing mode.

To this end, we interpret the "jump" of the collective branch into the collisionless $2\omega_r$ branch as the manifestation of pair-breaking of bosonic quasi-particles into single fermionic excitations. We emphasise, that while this interpretation may describe some of the observed features, it still seeks experimental evidence and remains on a speculative basis. The onset of pair-breaking is determined by the energy required to break up a pair, which coincides with the binding energy plus an energy contribution from the trap. Interestingly, we observe that the binding energy at which the collective mode intersects with the dipole resonance at $1\omega_r$ is very close to $E_B = \hbar\omega_r$ ($\eta \sim 0.1$). This can partially be explained by the single particle gap $\hbar\omega_r$ present in our system which is comparable to the Fermi energy $E_\mathrm{F} \sim 2.1\hbar\omega_r$ for $10 + 10$ atoms. If the binding energy is less than the harmonic oscillator energy, then the energy of the harmonic oscillator alone can break up pairs if they are not protected by another mechanism or gap.

The single-particle collisionless branch broadens symmetrically around $2\omega_r$ as we move further into the BCS side. Macroscopically one can associate the increasing width of the resonance with an increased damping. To the precision of our experiment we do not observe additional resonances which would correspond to a discrete level structure. Grasso et al. [81] have performed a microscopic quantum mechanical theoretical study of the radial quadrupole mode in the framework of the Bogoliubov–de Gennes and quasiparticle random-phase approximation method. The interested reader is referred to the referenced literature [81] for a detailed description of the theoretical model and methods used as we will only discuss some of the results. The authors numerically predict a "fragmentation" of the excitation spectrum, as the Fermi energy is reduced. As opposed to a single mode frequency they find multiple closely spaced peaks both for the collective quadrupole mode on the downbending branch as well as for the collisionless mode. Interestingly, we also observe a very wide spread, collisionless branch which could be interpreted as a "fragmented"

resonance. Since the study assumed trapped fermionic atoms in the superfluid BCS phase, and the latter is still a matter of great dispute in our system, the transferability of the results is ambiguous. However the fragmentation of the excitation spectrum as a generic effect of finite size systems may also be applicable outside the assumption of superfluidity and can partially explain the broadening of the collisionless branch in the BCS regime. While the origin of the broadening cannot be fully explained, one can argue that the space of possible k momenta is increased as the Fermi surface melts up due to the increased interaction strength and hence states further away from the initial Fermi energy can be occupied. As the particle number is increased the collisionless branch is shifted further to the BCS side. In fact for the 80+80 spectrum we did not observe the coexistence of the phononic excitations manifesting themselves in the collective branch and the single-particle collisionless branch indicating that in this "many-body" limit single particle excitations and collective excitations clearly separate in the low-energy regime where $\Omega < 2.5\omega_r$.

It is remarkable, that even for 10+10 atoms we find a small regime close to unitarity where the resonance frequency recovers the $\sqrt{2}\omega_r$ result expected for the hydrodynamic limit. This result together with the surface character of the mode explicitly probing the shearing behaviour supports the applicability of hydrodynamic theory even in very small systems such as ours. However our measurement also entails the breakdown of ideal hydrodynamics outside of this very narrow interaction regime, where such a simple theory fails at explaining the collective interplay in the system.

4.2.5 Exciting and de-exciting the quadrupole mode

Up to this point, the interpretation of the nature of the excitation and underlying microscopic processes was on a highly speculative basis that inevitably requires further experimental evidence. Experimentally, we only observed atom loss as a consequence of the smaller overlap of the evolved system with the ground state after the presented excitation scheme. This method obviously does not distinguish the excitation of a well-defined mode from a simple heating process where constituents are excited and eventually lost from the trap. If the collective excitation of the quadrupole mode is governed by a unitary time evolution it should be possible to excite and subsequently de-excite the mode.

In the experiment we can excite the quadrupole mode for n cycles and then wait for a certain time T before repeating the same quadrupole modulation again. Due to the periodic nature of the drive the perturbation Hamiltonian satisfies $\hat{H}_Q\left(t+\frac{T}{2}\right) = \hat{H}_Q(-t)$ opening the possibility to probe the unitary evolution. If the waiting time T equals half an oscillation period $T = \frac{1}{2\Omega}$ of the quadrupole mode we effectively reverse time and thereby rewind the accumulated phase, the latter only holding in the case of unitary evolution. While this measurement would in principle work, it is very sensitive to dephasing. Instead of driving the quadrupole perturbation for n cycles, then waiting for half a quadrupole period and driving it again for n cycles, we drive it forward for one cycle and backward for one cycle and repeat the forward-backward driving for a total of $2n$ cycles. Technically this is achieved by modulating the phase jump with a frequency of $\frac{\Omega}{2}$ as opposed to Ω as depicted schematically in figure 4.9(a).

The measurement, which was performed at $B = 670\text{G}(\eta = 0.21)$ in a "macroscopic" sample of $50 + 50$ atoms with $2n = 24$ driving cycles acts as a first indicator that the observed excitation is not simply a heating process but actually obeys unitary time evolution. While the dipole mode at $\Omega = 1\omega_r$ cannot be rewound, the quadrupole resonance vanishes in the forward-backward driving scheme as seen in figure 4.9(b).

The promising result of the recycled quadrupole mode encourages further studies of coherent oscillations as originally envisioned, albeit potential limitations due to dephasing. Indeed, if the time of the phase accumulation is increased dephasing occurs and the quadrupole resonance appears again in the spectrum. However, exactly on resonance we

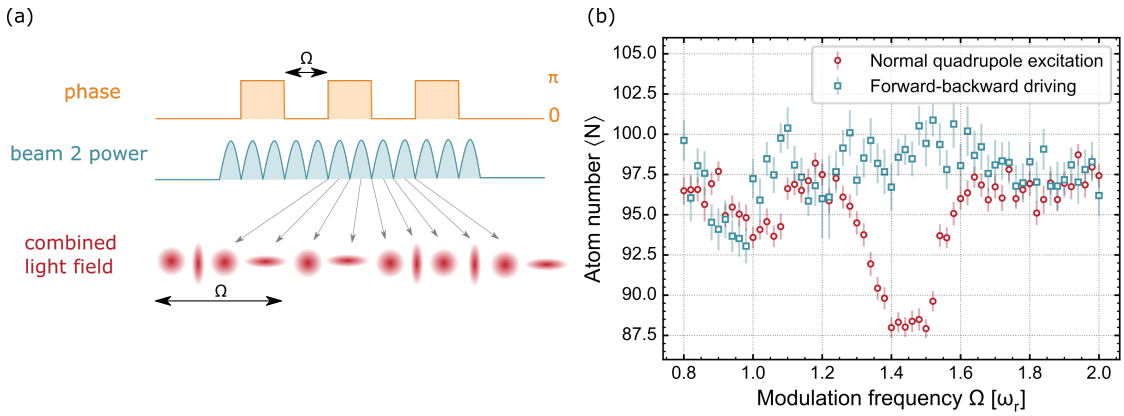

Figure 4.9: **Exciting and de-exciting the quadrupole mode** (a) The excitation scheme is changed such, that the phase jump is modulated with a frequency of Ω instead of $\Omega/2$ as for the normal quadrupole excitation. This scheme should excite and de-excite the quadrupole mode in each cylce. (b) When winding the excitation forth and back in each cycle the quadrupole resonance disappears whereas the dipole resonance at $\Omega = 1\omega_r$ remains.

find a small region where we can drive back a small fraction of the system to the ground state even for as many as ten cycles. Figure 4.10(a) shows the high-resolution spectrum for $40 + 40$ atoms at a magnetic field of $B = 636$G ($\eta = 0.86$) with the corresponding Gaussian fit yielding a quadrupole frequency of $\Omega = 2\pi \times (40.3 \pm 0.3)$kHz. The observed behaviour is quite remarkable considering that the many-body wave function accumulates phase due to the quadrupole oscillation for $n = 10$ periods and after waiting half an oscillation period, the phase can be rewound. In the wings of the resonance, the system is not perfectly in phase and significant dephasing impedes a recycling of the mode. Of course, only exactly on resonance the waiting time $T = \frac{1}{2\Omega} = \frac{1}{2\omega_Q}$ matches half a period of the oscillation, since we did not re-scale the delay time T to the respective frequency Ω. For modulation frequencies lower than the quadrupole frequency $\Omega < \omega_Q$, the time evolution is behind the evolution on resonance, whereas for higher modulation frequencies $\Omega > \omega_Q$ the time evolution is ahead of the evolution on resonance. In both cases the delay time $T = \frac{1}{2\omega_Q}$ does not correspond to a real "time-reversal" as $\hat{H}_Q\left(t + \frac{1}{2(\omega_Q \pm \delta)}\right) \neq \hat{H}_Q(-t)$ where $\delta = |\Omega - \omega_Q|$ is the detuning from resonance.

Even on resonance we are only able to recover a fraction of the $40+40$ initially prepared atoms probably due to technical limitations. For large atom numbers, where the Gaussian trap is completely filled, we have observed uncontrollable atom loss from the trap during the quadrupole excitation even without removing atoms above the initial fermionic ground state by spilling a second time. In this case the quadrupole oscillation is so strong that it can eject weakly-bound atoms in high levels of the Gaussian potential, which of course cannot be driven back. A non-vanishing coupling to other modes is also plausible, which would render a complete excitation recycling infeasible. Moreover, the measurement requires a high power stability of the trap. Only in a small region, approximately 500Hz wide, which corresponds to approximately 2% of the trap frequency ω_r, the excitation can be (partially) reversed. Since the trap frequency scales with the square-root of the optical power, the stability requirement for power fluctuations is $\Delta P \lesssim 4\%$ over the entire experiment and slight drift of the main trap frequency despite its power stabilisation seems possible. In addition, the perturbation beam is unstabilised during the quadrupole excitation due to the lack of a fast PID loop able to control the absolute sine modulation on frequencies $\sim$ 100kHz. The previously measured anisotropy of the potential might further alter the

excitation. As a consequence, the forward driving cycles may not be exactly identical to the backward driving cycles, which prevents a complete phase rewinding. In summary, measuring coherent oscillations of a quantum many-body system in our experiment is a delicate endeavour.

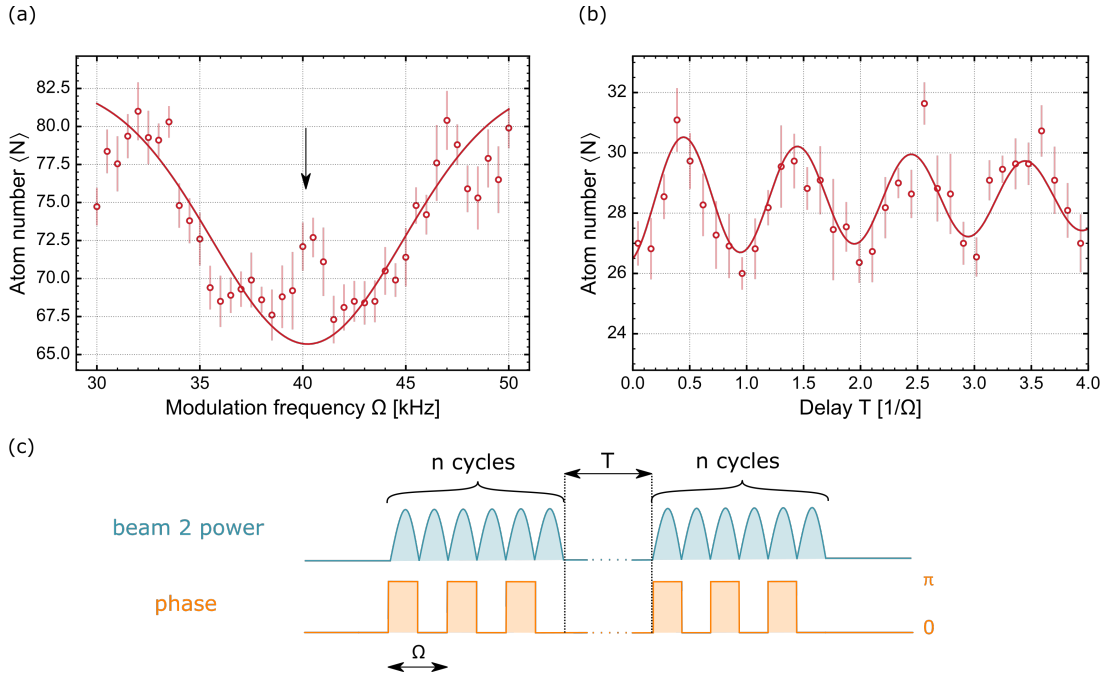

Figure 4.10: **Coherent oscillations of the quadrupole mode** (a) High-resolution spectrum of the quadrupole mode for $40 + 40$ atoms at $B = 636$G. Exactly on resonance, a fraction of the atom number can be restored if the delay time between excitation and de-excitation is $T = 1/(2\Omega)$. (b) Varying the time delay T between the excitation cycles and de-excitation cycles we observe coherent oscillations of the population of the quadrupole mode for 20+20 atoms. (c) Schematic excitation scheme: after n cycles we wait for a time T before modulating a second time for n cycles.

Hence, coherent oscillations may only be observed exactly on the quadrupole resonance and in a smaller sample where we have a better control of the preparation. To examine the phase dynamics of the mode in more detail, we prepare a smaller sample of $20 + 20$ atoms at $B = 636G$ ($\eta = 0.96$) and excite the quadrupole mode at the resonance frequency of $\Omega = 2\pi \times (45.73 \pm 0.03)$kHz for $n = 10$ cycles, wait for a delay time T and modulate again for $n = 10$ cycles (see figure 4.10(c)). The resulting expectation value of the number operator $\langle \hat{N} \rangle$ by our projective measurement scheme is shown in figure 4.10(b). A delay time of $T = 0$ corresponds to a normal quadrupole modulation with $2n$ cycles, where approximately 35% of the initially prepared 40 atoms are lost. Half a quadrupole oscillation later at $T = \frac{1}{2\Omega} = 10.9\mu$s, approximately one third of the initial population of atoms is restored. We indeed observe coherent oscillations of the population of the mode, which demonstrates our ability to control the excitation process by pumping energy into the mode and (partially) reverting the process.

Fitting a damped cosine function of the form

$$f(T) = A \cdot e^{-\lambda T} \cos(2\pi T - \varphi) + y \tag{4.23}$$

to the data yields a damping rate of $\lambda = (0.16 \pm 0.03)\Omega$ corresponding to a decoherence time of approximately 140μs. It should be stressed that the frequency of the oscillation

is set by the modulation frequency Ω and is hence not a fitting parameter in the function 4.23. This technique constitutes an alternative method to derive damping rates which has raised interest among theory collaborators [84] to derive upper bounds for the viscosity. Measurements across the BEC-BCS crossover are currently in progress.

The same measurement for $20+20$ atoms can be repeated on the BCS side at $B = 750$G ($\eta \sim -0.36$). We follow the same measurement protocol as on the BEC side but choose the collisionless resonance frequency $\Omega = 2\pi \times 52\text{kHz} \approx 2\omega_r$ for the excitation. The result is shown in figure 4.11 where the y axis is scaled to the same range as in figure 4.10(b) to allow for a direct comparison. As opposed to the previous measurement on the BEC side, we do not observe coherent oscillations at the precision of the measurement on the BCS side. The obtained result agrees well with the strong increase of the damping rate observed in the $50 + 50$ system (compare section 4.2.3) on the BCS side. This may serve as a first

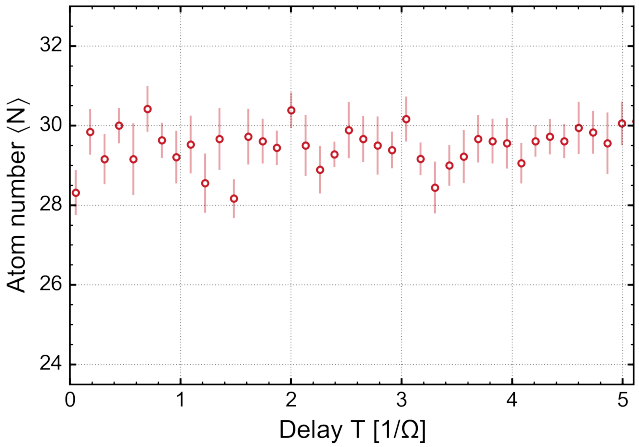

Figure 4.11: **Coherence measurement at 750G** At the precision of our measurement we do not observe coherent oscillations in a system of 20+20 atoms on the collisionless resonance. This agrees well with the increased damping rate on the BCS side.

indicator that the quadrupole mode on the collective branch exhibits coherence properties, whereas on the collisionless branch the coherence is lost. Further measurements are needed to confirm this observation across the BEC-BCS crossover and potentially identify the occurring jump from the collective into the collisionless branch as the transition between coherent and incoherent dynamics.

5 Discussion and outlook

5.1 Aberration correction

Precise control of quantum many-body states requires high-NA diffraction-limited optics which happen to be very sensitive to optical aberrations and deviations from a flat wavefront. Inexplicable spectral features and cloud shapes initially sparked the interest in reducing the optical aberrations in our system. After replacing faulty optical elements, such as a dichroic mirror and characterising the high-NA objective outside of the experiment (not presented in this thesis) we still observed residual aberrations that needed to be addressed. The PSI algorithm has been successfully used before [39, 86, 87] to measure aberrations on a camera. This method is however limited to a certain part of the optical path as motivated in section 3 and in particular excludes the objective and vacuum window. In this work we not only refined the PSI algorithm on the camera, but also implemented and tested a new variant of it to directly characterise the aberrations where they matter - on the atoms themselves. The method builds upon previous work from Zupancic et al. [5] but also differs significantly from it as we use a SLM and eliminate the need for an optical lattice. Our implementation of the PSI algorithm on the atoms requires:

- a device (e.g. SLM or DMD) to generate two small beams that can be moved across the aperture of the optical system. The relative phase between the beams should be variable.
- sufficient resolution of the imaging system in order to resolve at least one fringe minimum. It is sufficient to extract the signal after several averages.
- a method to confine the atomic cloud in the focal plane of the objective.

In principle, an axial lattice like our 2D trap is not necessarily required, since the atoms should anyway be trapped in the focal plane of the objective. However we have observed that the accuracy is significantly reduced when only using the single tweezer in the absence of the 2D trap. This can be explained by the elongation of the cloud in the axial direction resulting in an averaged phase that includes regions outside of the focal plane. In addition, the already limited fringe contrast is even further reduced possibly altering the phase recovery. Consequently, we still recommend introducing an axial confinement although it is not strictly necessary.

Moreover, we benchmarked the technique by introducing an artificial aberration and conjecture that wavefronts can be reconstructed with an accuracy of $\sigma_{rms} = \lambda/13$ and a precision of $\sigma_{rms} = \lambda/25$.

The accuracy could be improved further by running the algorithm several times until convergence. At this point in time, we are furthermore continuing to improve the wavefront reconstruction software and might eventually replace the primitive Zernike fitting routine with a spline interpolation which better describes the measured phases as discussed in section 3.4.

While the presented technique certainly came to fruition in our experiment, its universality may also benefit other quantum gas experiments around the world. From the creation of uniform Bose-Einstein condensates in box potentials [88] to tweezer arrays [89, 90] used for quantum information processing, they all rely on aberration-free potentials. While using decent optical elements in the first place is certainly a necessary prerequisite, our method

has proven to enable precise control of residual aberrations. The technique is incapable of compensating terrible optics and alignment but it offers a way to operate the commonly used high-quality components to its optimum - it does not make bad optics good, but it makes good optics great.

5.2 Collective excitations in mesoscopic quantum systems

In the performed experiments we successfully demonstrated the excitation of the radial $l = 2$, $m = \pm 2$ quadrupole mode in mesoscopic systems of different particle numbers. The obtained atom-loss spectra exhibit clear signatures of interaction-driven dynamics when compared to the non-interacting system (figure 4.4).

Towards the macroscopic limit ($80 + 80$ atoms), we have observed significant deviations from theoretical descriptions and previous experiments. In particular, the resonance frequency varies much stronger on a smaller range of interaction parameters when compared to the experimental work by Altmeyer et al. [6]. The further the atom number is decreased the steeper the slope of the collective branch gets. Mean-field corrections via the sum rule approach displays the same qualitative behaviour of a downbending of the mode from the BEC side towards unitarity, but shows very poor quantitative agreement and fails to recover the correct slope. In the many-body system studied by Altmeyer et al. [6], they observe a sudden jump from the collisionless to the hydrodynamic regime by smoothly varying the interaction parameter $\eta = 1/(k_{\mathrm{F}}a)$. This was associated to pair-breaking into single fermionic excitations that entailed the breakdown of hydrodynamics. Far in the BCS regime, we find a similar collisionless behaviour and while smoothly increasing the interaction parameter, we observe a sudden jump to the collective branch. In contrast to the Altmeyer et al. study, we did not find a plateau at $\sqrt{2}\omega_r$ which is only expected in the limit where ideal hydrodynamics is applicable, or in other words where the pairing gap clearly separates from the trap frequencies. If this is not the case, the collisionless and the collective mode couple to each other leading to a deviation from the hydrodynamic expectation of $\sqrt{2}\omega_r$ for the collective mode frequency. [44]

In addition, we cross the hydrodynamic expectation for the resonance frequency in a regime, where one would expect a more collisionless behaviour. In the presence of the trapping confinement, $\omega\tau \sim 1$ marks the transition between the hydrodynamic and collisionless behaviour, where ω is the excitation frequency of the mode and τ the collisional relaxation time. Purely collisional hydrodynamic behaviour is only recovered in the limit of $\omega\tau \to 0$. Naively, the collision rate τ^{-1} can be calculated by [32]

$$\tau^{-1} = n\sigma v \tag{5.1}$$

where n is the density, σ the collisional cross section and v the velocity. Since we are interested in an upper bound for the collision rate, we can consider the maximum unitarity limited cross section and write the "classical" collision rate [32] as

$$\tau^{-1} = \frac{k_{\mathrm{F}}^3}{6\pi^2}\frac{4\pi}{k_{\mathrm{F}}^2}\frac{\hbar k_{\mathrm{F}}}{m} = \frac{4}{3\pi}\frac{E_{\mathrm{F}}}{\hbar} \tag{5.2}$$

which results in $\omega\tau \approx 1.1$ for the 10+10 systems. This value represents a lower bound since we did not yet take into account Pauli blocking which reduces the number of final scattering states for collisions by an additional temperature dependent factor $\sim T^2$. [71] The true collision rate will consequently be significantly smaller suggesting that the observed behaviour lies in the collisionless regime.

Signatures of hydrodynamic behaviour in a mesoscopic system has also been observed very recently on a different experiment in our group (manuscript in preparation). They

studied the interacting expansion of a sample containing as few as ten atoms from an elliptic trap. This experiment is reminiscent of the elliptic flow experiments in a strongly interacting Fermi gas performed by O'Hara et al. [91]. Similar to the result in a macroscopic system, our colleagues also observe an inversion of the initial aspect ratio after long interacting expansion times in the mesoscopic system, which is a well-established observable for hydrodynamic behaviour. In this sense, their measurement of hydrodynamic behaviour in mesoscopic systems agrees well with our spectroscopic study of the surface mode explicitly probing hydrodynamics. Consequently, these complementary probes of hydrodynamic behaviour strongly suggest that even small systems with contact interactions can behave hydrodynamically despite a strongly suppressed number of collisions.

By varying the atom number and recording the spectra across the BEC-BCS crossover we witnessed the emergence of the collective branch constituting the birth of the quadrupole mode. In the limit of 1+1 particles the spectra are solely dominated by the confinement and do not show any signs of interaction apart from a small constant offset. As the number of atoms is increased the collective quadrupole mode separates from the $2\omega_r$ resonance which is fully developed at $10+10$ atoms. The steep increase or "jump" towards the BCS regime observed by Altmeyer et al. [6] occurs closer to unitarity in our 80+80 system, whose Fermi energy is a factor of ten smaller than the system studied by Altmeyer et al. It appears as if the collisionless branch moves further towards the BCS side as the particle number is increased and the collective mode branch survives smaller interaction parameters.

In accordance with theory [44, 63, 92] we currently interpret the transition between the downbending collective branch and the collisionless branch on the BCS side as the death of the collective mode due to pair-breaking. If the system size is reduced drastically, not even the lowest collective modes such as the quadrupole mode survive. If the size of the pairs exceeds the wavelength of an excitation, a single particle can be excited and a pair can be broken. [44, 68] In a superfluid system[1] the onset of pair-breaking would certainly depend on the pairing gap which has been experimentally confirmed [68]. Following this picture, we can plot the resonance frequencies of the quadrupole mode as a function of the pairing gap instead of the interaction parameter as shown in figure 5.1. The pairing gap is calculated from the mean-field BCS theory in the zero temperature limit following reference [93] for each interaction parameter η. Mean-field BCS theory is known to overestimate the pairing gap, which is thus only an upper approximation. Whereas the jump for different system sizes occurs at different interaction strengths, it seems to happen at approximately the same value of the pairing gap $\Delta \approx 2\hbar\omega_r$ for both systems (80+80 and 10+10). If the energy of single fermionic excitation[2] $2\hbar\omega_r$ is similar or exceeds the pairing gap Δ, then the ground state of the system is not a superfluid and would hence be found on the collisionless branch. [44] The competition between energy scales, in this case the pairing gap and the confinement energy, would ultimately dictate the behaviour of the system. A similar competition was observed in the study of the precursor of the Higgs mode in a mesoscopic system [3]. The strong increase in damping could then be explained by a diverging susceptibility and correlation length associated with a second-order phase transition. While this theory provides a qualitative description, we cannot confirm its applicability given the limited data (only 10+10 and 80+80) as well as the limited access to observables and the assumptions being made. In particular we were not able to study the suspected microscopic mechanism of pair breaking but only observed a loss of coherence on the BCS side. Since the interpretation still seeks experimental evidence, we only refer to it in the discussion part and do not claim it as a result and definitely not as evidence for superfluidity. Instead, it is supposed to encourage discussions about the microscopic mechanisms governing the transition from the collective to the collisionless branch.

[1] It should be stressed that we do not claim that our system is superfluid.

[2] parity allowed transition in the harmonic oscillator potential

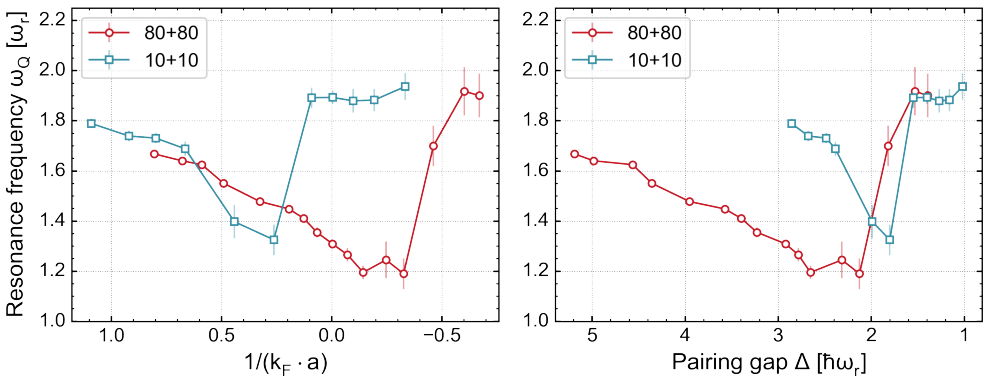

Figure 5.1: **Collective-to-collisionless transition** The jump of the quadrupole mode from the collective to the collisionless branch occurs at different interaction parameters $\eta = 1/(k_\mathrm{F}a)$ in the different sized mesoscopic systems (left plot). In the smaller 10+10 atom systems ($E_\mathrm{F} = 2.1\hbar\omega_r$) the transition is found on the BEC side, whereas in the larger 80+80 system ($E_\mathrm{F} = 4.3\hbar\omega_r$) it occurs further on the BCS side. Interestingly, the jump happens at similar values of a pairing gap around $2\hbar\omega_r$ for both systems (right plot), which can be interpreted as a competition between energy scales. The data points, which have been extracted from Gaussian fits of the quadrupole resonances, are connected to provide a visual guide to the eye.

The direct observation of the quadrupole oscillation similar to previous experiments [6] by taking snapshots of the cloud transpires to be challenging in our system. As presented in section 2.3.2 we are in principle capable of imaging microscopic samples with single-atom resolution. In situ, the size of the system confined in the tweezer is in the same order as the diffraction limit of our high-NA optics rendering the resolution of the in-situ density infeasible. However, the quadrupole motion should also manifest itself in the momentum distribution which can be extracted after letting the sample expand for a finite non-interacting time-of-flight [50, 53]. The beginning of the expansion can be timed very precisely, below the excitation period $\tau \approx 1/\Omega \approx 25\mu$s allowing for the measurement of the momentum at different times during one single quadrupole oscillation. Since each image of an experimental shot only contains very few atoms, extracting the density distribution would require substantial averaging. Although this is not a problem per se, it raises the need for monitoring the orientation of the ellipse or quadrupole deformation which might vary from experimental shot to shot due to thermal fluctuations of the relative phase of the two beams. The camera monitoring the light field behind the SLM (compare figure 2.4) can be used for this purpose. Each individual time-of-flight image could then be rotated back in post-processing according to the initial orientation of the elliptical deformation. From the averaged image the momentum distribution of the quadrupole oscillation could furthermore be extracted for different times during an oscillation period. In addition to the obtained spectrum this measurement would provide valuable insight to the dynamics of the system.

5.2.1 Outlook

Collective modes are commonly described as classical oscillations and derived in the framework of hydrodynamics. For Bose-Einstein condensates an alternative microscopic quantum theory of collective modes has been developed [63, 94, 95]. Although the microscopic details of this theory still seek experimental evidence and its applicability in Fermi gases is

unclear, the predictions of novel quantum dynamics makes it worthwhile considering its implications for our experiment. In this framework, collective oscillations of a condensate are treated as a coherent superposition of stationary states with different number of quanta of the oscillator comparable to a bosonic mode in a cavity. [94, 95, 96] While coherent states are the most classical states a quantum system can be in and have minimal uncertainty, they still exhibit fundamentally non-classical behaviour. [97] One such non-classical phenomenon that has been predicted by theory is the collapse and revival of collective oscillations. A coherent state in a perfect harmonic oscillator would simply oscillate forth and back without dispersing. However, fluctuations in the number of quanta of the oscillations of the mode ultimately lead to a dephasing and subsequent collapse of the collective excitation. Since the process is not dissipative, the oscillation reappears in the form of a revival. The effect is a consequence of the non-linearity which is introduced by the different transition frequencies for the stationary components of a coherent state. Following the work from Pitaeskii [95] the collective mode can be described as an anharmonic oscillator whose frequency is given by

$$\omega = \omega_0 + \delta\omega = \omega_0(1 + \kappa E) \tag{5.3}$$

considering the first linear correction in the energy E to the bare collective mode frequency[3] ω_0 with κ being the first-order non-linearity constant. The sinusoidal driving prepares the coherent state of the oscillator, which can be expressed as

$$\Psi = \sum_n c_n \psi_n \exp\left[-i\omega_n t\right] \tag{5.4}$$

where ψ_n are the respective stationary states with energy $\hbar\omega_n$ of the oscillator. It should be stressed that n is not the occupation number of atoms but rather the number of quanta of oscillations of the mode. The coefficients c_n follow the Gaussian form

$$|c_n|^2 = \frac{\exp(-\bar{n})\bar{n}^n}{n!} \approx \frac{1}{\sqrt{2\pi\bar{n}}} \exp\left[-\frac{(n-\bar{n})^2}{2\bar{n}}\right] \tag{5.5}$$

where $\bar{n}$ is the average number of quanta in the mode. The underlying dynamics manifest itself when evaluating the expectation value of the oscillator coordinate x, which in our system would be connected to the observed atom loss (see section 4.2.5). Under the assumption that only transitions of the form $n \to n \pm 1$ contribute to the fluctuations, the oscillator coordinate x reads

$$\langle x(t)\rangle \approx A \sum_n |c_n|^2 \cos\left[(\omega_0 + \kappa\hbar\omega_0^2)t\right] \sim \exp\left[-\left(\frac{t}{\tau_c}\right)^2\right] \tag{5.6}$$

where A is the fractional amplitude of the oscillation and thus varies between zero and one. Hence, the non-linearity entails a Gaussian damping of the amplitude of the oscillation with a collapse time τ_c. This result is fundamentally different from the exponential damping expected from dissipative decoherence. The revival time can be calculated directly from the periodicity of $\langle x(t)\rangle$ yielding

$$\tau_r = \frac{2\pi}{\hbar\omega_0^2|\kappa|} \tag{5.7}$$

and the collapse time is given by

$$\tau_c = \frac{1}{|\kappa|\omega_0}\frac{1}{\hbar\omega_0}\sqrt{\frac{2}{\bar{n}}} = \frac{1}{|\kappa|\omega_0}\sqrt{\frac{2}{E\hbar\omega_0}}. \tag{5.8}$$

[3] for the quadrupole mode in the hydrodynamic limit $\omega_0 = \sqrt{2}\omega_r$

Dalfovo et al. [98] have provided a useful relation to common system quantities such a as the atom number N and chemical potential μ. Under the assumption of LDA the authors have shown that

$$\kappa = \frac{\delta}{\epsilon \mu N} \qquad \text{with} \qquad \delta = \frac{16 - 5\lambda^2}{4(16 - 7\lambda^2)} \tag{5.9}$$

where $\lambda = \omega_z/\omega_r$ is the anisotropy parameter and ϵ a mode-specific constant that relates the energy E of the mode with the chemical potential, atom number and amplitude via $E = \epsilon \mu N A^2$. Using this relation the collapse and revival times are given by

$$\tau_c = \frac{1}{\omega_0} \frac{\sqrt{2\epsilon}}{A|\delta|} \sqrt{\frac{\mu N}{\hbar \omega_0}} \qquad \text{and} \qquad \tau_r = \frac{2\pi \epsilon \mu N}{\hbar \omega_0^2 \delta}. \tag{5.10}$$

From the above equations it becomes clear that the observation of this effect is favoured in small N systems. In fact, Pitaevskii [95] states about the visibility of the collapse and revival

"*To observe the effect considered here one must try to have as small a number of atoms as possible.*"

Our few-Fermion system thus seems to be an ideal candidate platform to test this highly non-classical behaviour of collective modes. Let us estimate the experimental parameters naively assuming that the same equations derived above also hold for Fermi gases. Deep in the molecular BEC we can approximate the chemical potential with $\mu \sim -E_B/2$ [93]. For the quadrupole mode with $\epsilon = 4/7$ [98] these equations give $\tau_c \approx 200\mu$s and $\tau_r \approx 600\mu$s in our system assuming $\lambda = 1/6$, $A = 0.2$, $N = 10 + 10$, $\omega_0 = \sqrt{2}\omega_r$ with $\omega_r = 2\pi \times 27.3$kHz. The derived values are by no means thought to be quantitative as they have been derived for BECs under the assumption of LDA and numerous approximations along the way. Although these results may be off quite substantially the time scale is still within experimental reach in our setup, as opposed to other macroscopic systems. Studying such a collapse and revival of a quantum field constitutes a prime example for coherent quantum dynamics far from equilibrium. Moreover, the collapse and subsequent revival would immediately imply the quantisation of the collective mode. [99]

One of the key features of mesoscopic systems is the existence of a shell structure, which is found in atomic nuclei, electronic configurations of atoms, metallic clusters but also in our trapped mesoscopic quantum gas system. During our studies of collective modes we have not observed any influence of the shell structure on the collective modes nor "magic number" effects associated with particular number of atoms. The absence of these effects can be explained by the respective symmetry of the excitation and symmetry of the shell structure. While the radial quadrupole mode only couples in the radial direction, the elongated trap shape in the axial direction dictates a bunching of axial and not radial states. Since the symmetry axis of the quadrupole oscillation (radial) and the symmetry axis of the shell structure (axial) are orthogonal, a coupling and consequent effect might not be expected. The breathing or scissors modes on the other hand would enable the study of the shell configuration dependence of collective modes due to their coupling to the axial degree of freedom, which is highly relevant to nuclear physics.

In general the study of collective modes in cold atom systems exhibits a multitude of analogies to nuclear matter found in for example atomic nuclei or neutron stars [44]. As opposed to cold atoms, nuclei consist of two types of nucleons, protons and neutrons, and can hence form three different types of pairs - proton-proton (pp), neutron-neutron (nn) and proton-neutron (pn). The last one hosts a bound state, called the deuteron or heavy hydrogen. For low densities the deuteron is bound, whereas for higher densities the binding energy decreases and the bound "dimer" becomes unbound and turns into a pn Cooper pair,

reminiscent of the BEC-BCS crossover discussed in this thesis for cold atoms. The higher abundance of neutrons over protons, commonly referred to as n-p asymmetry, favours pp and nn pairing. Since the nn system is almost bound, its scattering length becomes very large comparable to the unitary regime. [44] Describing nuclear matter in the framework of BCS theory consequently comes natural and under certain limitations a lot can be learned about one system by studying the other. Alpha-particle condensation in finite nuclei and its connection to the excited Hoyle state has recently raised a lot of attention and discussion in the nuclear scientific community. [44, 100, 101, 102] The observation of such an analogous peculiar state in a mesoscopic quantum-gas experiment may contribute to a better understanding of microsopic processes of alpha-particle condensation and would hence constitute a prime example of quantum simulation with ultracold atoms.

5.3 Probing superfluidity

Our work on collective modes was originally inspired by the search for signatures of superfluidity in mesoscopic systems. Indications of superfluidity have already been observed in mesoscopic systems of atomic nuclei [20] and tiny Helium-4 clusters [2] consisting of as few as 60 particles. Probing and understanding the emergence of superfluidity promises to reveal new insights about this peculiar phenomenon stimulating the scientific curiosity and has the potential to inspire new technological applications. Loophole free proofs of superfluid behaviour are generally not trivial in microscopic systems as macroscopic phenomena, such as vanishing resistance may not be directly observable.

The connection between superfluidity and collective modes was first established in nuclear physics and soon extended to the study of Bose-Einstein condensates. The observation of the scissors mode in a trapped Bose-Einstein condensate [28] was considered a clear proof for its superfluid behaviour. Generally, the relation between Bose-Einstein condensation and superfluidity is a subtle one. Bose-Einstein condensates do not necessarily exhibit superfluid behaviour, with one prominent example being an ideal non-interacting Bose gas in the zero temperature ground state. On the other hand superfluidity can also occur in systems that are not true BECs as for example in reduced dimensions via the BKT mechanism. In "bosonic" BECs the frequency of the scissors mode for the normal and superfluid phase differ allowing for a clear distinction between the two regimes by the single measurement of the resonance frequency of a collective mode [103]. In the absence of superfluidity the moment of inertia of the gas takes a rigid value implying two modes with respective frequencies $\omega = \omega_z \pm \omega_x$[4]. In the superfluid case on the other hand only a single frequency $\omega = \sqrt{\omega_x^2 + \omega_z^2}$ for the scissors mode is found. An important condition for the direct relation between the mode frequency and superfluidity is that the collisional relaxation times τ in BECs are very long and the system is hence found in a collisionless regime.

As promising as deduction of superfluidity from the mode frequency may sound, the connection between collective mode frequencies and superfluid behaviour is not as straightforward in ultracold Fermi gases. While the scissors mode has been observed [66] in a trapped Fermi gas it does not provide conclusive evidence for superfluidity. Apart from the mode frequency Wright et al. [66] reported a second damping peak of the scissors mode which they associate with the transition from a hydrodynamic to a superfluid phase, but their explanation remains on a highly speculative basis and later a similar positive slope of damping versus temperature was found in a normal interacting Fermi gas [104]. Close to a Feshbach resonance the high collision rates favour the realisation of a hydrodynamic regime even at lowest temperatures and in the absence of superfluidity. [63] As has been pointed out by Cozzini and Stringari [105], in this crossover regime a clear distinction

[4] following the coordinate system used in [28]

between collisional hydrodynamics and superfluid hydrodynamics based on collective mode frequencies is impossible. A similar argument can be made for the frequencies of the radial compression mode [106]. It has been shown experimentally [104] that the frequency of the radial compression mode at unitarity remains constant when the temperature is increased. This suggests that the system is governed by the same hydrodynamic equations both in the low-temperature limit of the superfluid but also far above the critical temperature for superfluidity. [63] Although damping of the mode may be used as a probe for the viscosity the promised "evidence for superfluidity" [107] remains ambiguous.

Owing to the present equivocation in Fermi gases we conclude that clear evidence for superfluidity is not found by the direct measurement of collective mode frequencies without further considerations. In fact, the striking and unambiguous evidence for superfluidity in Bose-Einstein condensates and Fermi gases was not the observation of collective modes but was provided by observation of quantised vortices [108, 109] arranged in vortex lattices. As opposed to a normal gas, a superfluid is described by the equations of irrotational hydrodynamics [105]. At zero temperature $T = 0$ and within the limits of the local density approximation the equations can be expressed as

$$\frac{\partial n}{\partial t} + \nabla \cdot (n\mathbf{v}) = 0 \tag{5.11}$$

and

$$\frac{\partial \mathbf{v}}{\partial t} = -\nabla \left(\frac{v^2}{2} + \frac{V_{ext}}{M} + \frac{\mu}{M} \right) = -\nabla \left(\frac{v^2}{2} + \frac{V_{ext}}{M} \right) - \frac{\nabla P}{Mn} \tag{5.12}$$

where $\mathbf{v}$ is the velocity field, n the density, V_{ext} the trapping potential, μ the chemical potential, M the mass and P the pressure. In the zero temperature limit the pressure and chemical potential are directly related via $\nabla P = n\nabla\mu$. The superfluid velocity field $\mathbf{v}$ is irrotational since its vorticity, the curl of its velocity field, is zero. A normal gas on the other hand can support vorticity as its velocity field is governed by the Euler equation

$$\frac{\partial \mathbf{v}}{\partial t} = -\nabla \left(\frac{v^2}{2} + \frac{V_{ext}}{M} \right) - \frac{\nabla P}{Mn} + \mathbf{v} \times (\nabla \times \mathbf{v}). \tag{5.13}$$

involving the vorticity term $\mathbf{v}\times(\nabla\times\mathbf{v})$. It is commonly accepted [32, 94] that irrotationality is indeed a distinguishing factor between the superfluid and normal phase applicable in both Bose [94] and Fermi systems [63]. As opposed to the vorticity $\nabla \times \mathbf{v} = 2\Omega$ of a normal gas, the vorticity of a superfluid is concentrated along a single line and the circulation of the velocity field is quantised [94]

$$\oint \mathbf{v} \cdot dl = \frac{\pi\hbar}{m} n. \tag{5.14}$$

with n being an integer. Under the assumption that the vortex is aligned with the symmetry axis (z) of the density profile the corresponding angular momentum is given by

$$\langle \hat{L}_z \rangle = m \int d\mathbf{r} (\mathbf{r} \times \mathbf{v}) n(\mathbf{r}) = N \frac{\hbar}{2}. \tag{5.15}$$

The nucleation of a vortex is only energetically favourable above a critical rotation frequency Ω_c, when its energy E_v is equal to the energy change of the system $E - \Omega_c \langle \hat{L}_z \rangle$ rotating with angular velocity Ω_c. [63] If the angular velocity is increased further, more vortices are nucleated because it is energetically favourable to have two vortices with single angular momentum, as opposed to one vortex with two angular momenta. As a result they form a vortex lattice where the vorticity approaches the rigid value 2Ω. The density of

vortices $n_v = 2m\Omega/(\pi\hbar)$ is solely dictated by the rotation frequency and in particular independent of the density of the system. [63]

The process of vortex nucleation in condensates is commonly related to the formation of nodal lines that enter from the surface as angular momentum cannot be transferred spontaneously. In fact, in classical systems such as atmospheric weather, vortices are formed in a similar fashion by a separation of a boundary layer [110], but in these systems the vorticity is of course continuous as opposed to the quantum mechanical situation. In quantum systems vortices are thought to be nucleated as a collapse of surface excitations, which provide the required coupling to angular momentum [111]. The critical velocity for such a a rotational instability is $\Omega_c = \min_l(\omega_l/l)$ which corresponds to Landau's critical velocity [21]. The creation of a vortex from a quadrupole excitation with frequency $\sqrt{2}\omega_r$ would hence occur at a critical frequency of $\omega_r/\sqrt{2}$ when the quadrupole excitation becomes rotationally instable. However, vortex formation has also been observed [21] below the instability frequency of surface excitations which only sets an upper bound for the critical frequency as shown theoretically by Dalfovo et al. [112]. Nonetheless, the existence of a critical rotation frequency for the transfer of angular momentum is fundamentally different from the classical system where such a boundary does not exist. The observation of a long-lived vortex above the critical rotation frequency would hence provide reliable evidence for the achievement of a superfluid.

Our current experimental setup allows us to rotate the elliptically deformed trap by changing the relative phase between the two incident beams on the SLM (see section 2.2.1). By changing the relative frequencies using the respective AOMs the rotation frequency of the interference pattern can be continuously tuned from $\Omega = 0$ (no rotation) to far beyond the trap frequency $\Omega \gg \omega_r$ setting the deconfinement limit. Even if a vortex could be nucleated in our experiment, the small size of our system containing only a few (~ 10) atoms makes a direct observation of a vortex challenging. In general, the typical size of a vortex is given by the healing length [94]

$$\xi = \sqrt{\frac{1}{8\pi na}} \tag{5.16}$$

and gives the smallest distance over which the order parameter can heal. At unitarity the healing length will be minimal[5] and a potential vortex cannot be resolved in situ but only after expansion. The expansion of the in situ wavefunction using a matterwave magnifier [113, 114, 115] is currently not implemented in our setup but could in principle be achieved by generating an expansion trap using an existing AOD tweezer setup not presented in this thesis. Due to its topological nature a vortex should also manifest itself in the momentum distribution and could in principle be observed even after a time of flight eliminating the need for a matterwave magnifier. However even under the assumption that the sample might host a vortex and we could resolve its healing length via expansion, a direct observation as a "hole" in the density could only be obtained after subsequent averaging over many experimental runs. A single shot only represents the projection of the wavefunction on the position of ~ 10 particles, from which claims about the existence of a vortex is infeasible. While subsequent averaging over many experimental implementations of the same many-body wavefunction reveals the density which is the first-order correlator, the vortex position would have to be fixed. Otherwise its manifestation as a "dip" in the density profile may just be washed out by the averaging. Fortunately a single vortex would even equilibrate in the center of the cloud to minimise its energy. Qualitatively, this can be understood as a repulsion from the boundaries of the cloud to minimise its energy. It would be experimentally very challenging and time-consuming to tune the rotation frequency to

[5] it does not converge to zero as one might expect from its inverse relation to the scattering length but rather reaches a finite value in the order of k_F^{-1}.

a regime, where only one single vortex is created[6]. Finding the right rotation frequency without knowing the exact onset of vortex nucleation in combination with a poor imaging that heavily relies on averaging is literally the experimentalist's version of finding the needle in the haystack.

Instead, collective modes with angular momentum may provide an alternative route to measure the angular momentum of the system. The coupling of angular momentum, which is directly related to the rotationality, could however also be observed in the spectrum of collective modes. In the absence of angular momentum the $l = 2$ quadrupole mode, and in fact any $l > 1$ mode is degenerate in the m quantum number. This degeneracy is however lifted if the system is rotated introducing angular momentum. Consequently, the resonance peak of modes with angular momentum, such as the quadrupole mode, would split, which can be observed in the spectrum. In addition to the quadrupole motion of the density in real space, the angular momentum leads to precession of the cloud above a critical rotation frequency that has been observed before [116].

Let us first consider the case for a normal fluid, where Cozzini and Stringari [105] have shown that the mode frequencies of the $m = \pm 2$ modes in the presence of rotation are given by

$$\omega_Q(m = \pm 2) = \sqrt{2\omega_r^2 - \Omega^2} \pm \Omega \tag{5.17}$$

where Ω is the frequency of rotation. Observe that this equation only holds for the hydrodynamic limit where $\omega_Q = \sqrt{2}\omega_r$ and does not apply in the superfluid phase due to irrotationality. The splitting can also be obtained via the sum rule approach [117]

$$\Delta\omega = \omega_{+2} - \omega_{-2} = \frac{2}{M}\frac{\langle l_z \rangle}{\langle x^2 + y^2 \rangle} \tag{5.18}$$

where $\langle l_z \rangle$ describes the angular momentum per particle. This value corresponds to the rigid value $\langle l_z \rangle = M\Omega\langle x^2 + y^2 \rangle$ in the collisional hydrodynamic regime [105]. Since the splitting is of the same order as the quadrupole and trap frequencies it should easily be visible in our spectral measurements.

In the case of a superfluid, angular momentum is quantised with $\langle l_z \rangle = \hbar/2$ and can only be transferred into the system above a critical rotation frequency Ω_c for vortex nucleation. Hence we conclude that the splitting of the quadrupole mode alone does not provide evidence for superfluidity, but rather the existence of a critical rotation frequency and the long lifetime of a vortex. Below the critical rotation frequency, no angular momentum can be transferred into the system due to the irrotationality condition and only a single quadrupole resonance is observed. Above the critical frequency vortices can be nucleated transferring (quantised) angular momentum into the system which leads to a splitting of the quadrupole mode. In the presence of a single vortex the resulting splitting $\delta\omega$ can be calculated[7] perturbatively [118] or using the sum rule approach [117] both under the assumption of LDA yielding

$$\Delta\omega = \omega_{+2} - \omega_{-2} = \frac{2\omega_r}{\lambda^{2/5}}\left(15\frac{Na}{a_{ho}}\right)^{-2/5} \tag{5.19}$$

where $\lambda = \omega_z/\omega_r$ characterises the trap deformation. Naively evaluating this expression for typical parameters in our system (~ 50 atoms, $B = 630$G, $\omega_r = 27$kHz, $\lambda = 1/6$) yields a large relative splitting of $\Delta\omega/\omega_Q \approx 1.3$ when compared to the splitting of a macroscopic

[6] or at least a configuration where a vortex is located in the middle of the cloud

[7] In the general derivation Bruun et al. [118] assumed a spherical trap. In the case of the $m = \pm 2$ quadrupole mode which do not couple to the axial degree of freedom, the result should still hold in axisymmetric traps. The deviation from spherical symmetry only leads to the coupling between the $l = 0, m = 0$ and $l = 2, m = 0$ compression modes, leaving the x-y plane modes unchanged.

system ($\sim 10^6$atoms) of only $\Delta\omega/\omega_Q = 0.02$. The respective resonances would be found at $\omega_{-2} = 0.5\omega_r$ and $\omega_{+2} = 2.3\omega_r$, whereas the $\sqrt{2}\omega_r$ peak would have completely disappeared. Obvisouly, the dramatic result has been obtained under the imprudent assumption of LDA. As we have seen in the measurement of the radial quadrupole mode the LDA is generally not applicable in mesoscopic systems, where the vortex is not a perturbation but might be a feature in the same size as the system. However, even outside the applicability of LDA, we would expect the effect of the presence of a vortex on the spectrum to be substantial for the same reason. Since even the macroscopic splitting of the mode is within the precision of our experiment, we argue that the spectroscopic detection method may be advantageous to a direct imaging of a vortex. Indeed, this was the original motivation for studying the spectrum of the quadrupole mode after all.

A first experimental attempt of observing the splitting of the quadrupole mode remained unsuccessful, in the sense that we did not observe a splitting of the quadrupole mode. Experimentally, we prepared a system of $50 + 50$ atoms in our tweezer and adiabatically ramped on the rotating perturbation beam to approximately 5%. Subsequently, we rotated the system for 20 periods with frequencies between $\Omega/\omega_r = 0 - 1$ before quenching off the perturbation beam. We let the system evolve for ~ 5 oscillation periods allowing for potential vortex nucleation through a rotational instability. After the nucleation period, we started our normal quadrupole excitation scheme and reconstructed the spectrum via atom loss spectroscopy equivalent to the methods used in section 4.2. So far, these first experimental attempts were immature and the experimental techniques and pathways for vortex nucleation are far from being exhausted. Nevertheless, the presented work on collective modes paved the way for future spectroscopic probes of superfluid behaviour in mesoscopic systems. To the present day, vortex nucleation in previous experiments was primarily[8] stimulated by rotational instability comparable to the famous rotating bucket of liquid helium with rough walls. Dagnino et al. [122] have theoretically proposed a promising adiabatic passage for vortex nucleation in a mesoscopic system containing as few as 6 or 10 atoms that might be realisable in our system. As the authors point out this study would apart from its implications for superfluidity act as a prime example for symmetry breaking in quantum many-body states. In the case of rapid rotation a similar adiabatic pathway has been proposed [123] to achieve novel parameter regimes hosting strongly correlated states associated with fractional quantum Hall effects.

We conjecture that the precise control of quantum many-body states in combination with the ability to introduce rotation has the potential to dawn a new paradigm in the study of complex ordering phenomena. Understanding the emergence of interaction-driven quantum many-body phenomena may not only spark new technological applications but also stimulate humanity's curiosity in fundamentally understanding collective behaviour.

[8] Other mechanism, such as the Kibble-Zurek mechanism [119, 120] or Berezinskii–Kosterlitz–Thouless mechanism [121], can enable vortex nucleation even in the absence of a rotational instability.

A Appendix

A.1 Electronic level structure of ^{6}Li

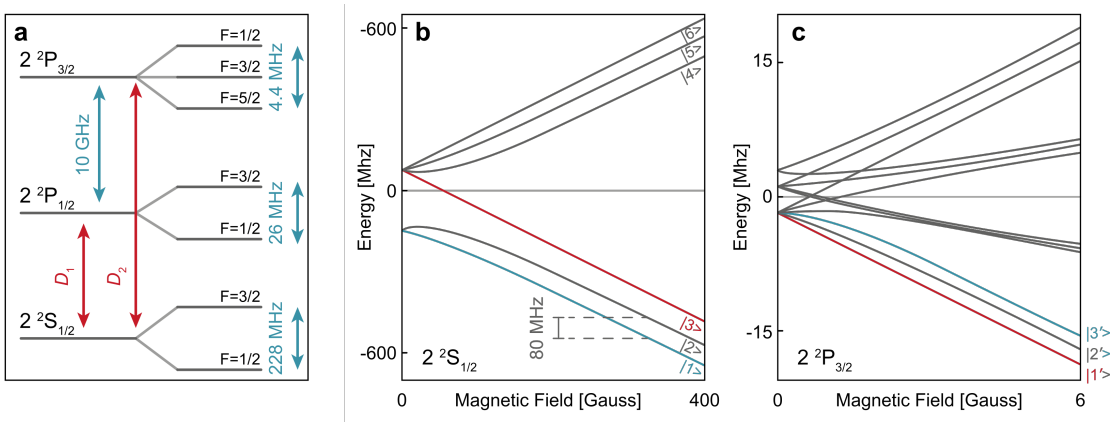

Figure A.1: **Electronic level structure of ^{6}Li** (a) The electronic ground state $2^2S_{1/2}$ of ^{6}Li exhibits two hyperfine manifolds at zero magnetic field that can be coupled via the D_1 and D_2 lines to the higher excited $2^2P_{1/2}$ and $2^2P_{3/2}$ states. In the presence of a magnetic offset field both the ground state (b) as well as the excited state (c) levels split according to the magnetic sub-manifolds. In the Paschen-Back regime at high magnetic fields the hyperfine energy splitting becomes proportional to the m_J quantum number.
This figure is adapted from reference [37].

A.2 Trapping potential of a Gaussian beam

The trapping potential of the optical tweezer is generated by focusing beam 1 through our high-NA objective presented in section 2. The intensity profile of the focused Gaussian beam propagating in z direction is given by [54]

$$I(r,z) = \frac{I_0}{1+\left(\frac{z}{z_0}\right)^2} \exp\left[-\frac{2r^2}{w_0^2}\right] \tag{A.1}$$

where I_0 is the peak intensity and w_0 the waist defined as the radius where the intensity dropped to a factor of $1/e^2$. The Rayleigh range is given by

$$z_0 = \frac{\pi w_0^2}{\lambda} \tag{A.2}$$

where λ is the wavelength (1064nm). Inserting this expression for the intensity profile into the equation for the optical dipole trap 2.1 yields

$$U(r,z) = -\frac{U_0}{1+\left(\frac{z}{z_0}\right)^2} \exp\left[-\frac{2r^2}{w_0^2}\right] \tag{A.3}$$

where U_0 incorporates the entire pre-factor in equation 2.1. A relation to the resulting trap frequencies can be established by Taylor expanding [33] the trapping potential about the centre where atoms are trapped

$$U(r,z) \simeq -U_0 + \frac{U_0}{z_0^2}z^2 + 2\frac{U_0}{w_0^2}r^2 + ... \tag{A.4}$$

The first and second order term corresponds to the harmonic approximation of the Gaussian potential from which we can identify the respective trap frequencies by setting

$$\frac{U_0}{z_0^2}z^2 \equiv \frac{1}{2}m\omega_z^2 z^2 \tag{A.5}$$

$$2\frac{U_0}{w_0^2}r^2 \equiv \frac{1}{2}m\omega_r^2 r^2. \tag{A.6}$$

where m is the mass of ^{6}Li atoms. Rearranging for the axial and radial trap frequencies yields

$$\omega_z = \sqrt{\frac{2U_0}{mz_0^2}} \tag{A.7}$$

$$\omega_r = \sqrt{\frac{4U_0}{mw_0^2}}. \tag{A.8}$$

A.3 Hydrodynamics and collective modes in the framework of the Gross-Pitaevskii equation

This alternative derivation of collective modes follows the work from Dalfovo et al. [94]. The many-body Hamiltonian of interacting bosons confined in an external potential in second quantization can be composed as

$$\hat{H} = \int d\mathbf{r}\hat{\Psi}^\dagger(\mathbf{r})\left[-\frac{\hbar^2}{2m}\nabla^2 + V_{ext}(\mathbf{r})\right]\hat{\Psi}(\mathbf{r}) + \frac{1}{2}\int d\mathbf{r}d\mathbf{r}'\hat{\Psi}^\dagger(\mathbf{r})\hat{\Psi}^\dagger(\mathbf{r}')V(\mathbf{r}-\mathbf{r}')\hat{\Psi}(\mathbf{r}')\hat{\Psi}(\mathbf{r}) \tag{A.9}$$

where $\hat{\Psi}^\dagger(\mathbf{r})$ and $\hat{\Psi}(\mathbf{r})$ are the boson field operators, creating or annihilating the boson at position $\mathbf{r}$. The first two terms in the first integral describe the kinetic and potential energy respectively, while the second integral describes the interaction between two constituents via an interaction potential $V(\mathbf{r}-\mathbf{r}')$.

The time evolution of the field operator describing the dynamics of interest is of course governed by the Heisenberg equation

$$i\hbar\dot{\hat{\Psi}}(\mathbf{r},t) = \left[\hat{\Psi}, \hat{H}\right]. \tag{A.10}$$

While the above equation obviously covers the full dynamics of the many-body system, the solution to this problem is generally complex and the equation as such only provides limited insight into the condensate's dynamics which we intend to study.

In order to retrieve the time-dependent condensate wave function $\psi(\mathbf{r},t)$ the field operators can be replaced by the classical field ψ given that the distance $\mathbf{r}-\mathbf{r}'$ is large.

Substituting ψ and the effective two-body potential (2.14) into equation A.10 yields the celebrated Gross-Pitaevskii equation (GPE) [1]

$$i\hbar\frac{\partial}{\partial t}\psi(\mathbf{r},t) = \left(-\frac{\hbar^2\nabla^2}{2m} + V_{ext}(\mathbf{r}) + g|\psi(\mathbf{r},t)|^2\right)\psi(\mathbf{r},t). \tag{A.11}$$

[1] Theoretical derivations can be found in standard quantum mechanics text books [36, 42] and are omitted for the purpose of focusing on the resulting consequences.

The non-linear nature of the equation arises from the interaction among the constituents which is treated as a mean-field potential of the $N-1$ other particles. It is thus well suited to describe the macroscopic dynamics and variations of the order parameter on length scales larger than the interparticle spacing. On microscopic length scales or for small system sizes the mean-field approach looses its validity and the GPE is no longer applicable to the situation.

In the limit of large numbers of constituents, which are interacting repulsively, the Thomas-Fermi approximation can be applied, which allows for analytic expressions for ground state properties. When $Na/a_0 \gg 1$ the quantum pressure term in the GPE is only relevant at the boundary and becomes negligible when compared to the interaction energy. When the quantum pressure term is completely neglected the density profile simplifies to

$$n(\mathbf{r}) = \begin{cases} \psi^2(\mathbf{r}) = \frac{1}{g}\left(\mu - V_{ext}(\mathbf{r})\right) & \text{for } \mu > V_{ext}(\mathbf{r}) \\ 0 & \text{for } \mu < V_{ext}(\mathbf{r}) \end{cases} \tag{A.12}$$

This is considered the Thomas-Fermi approximation or local density approximation (LDA), which is applicable if the Fermi energy and chemical potential are much larger than the single particle harmonic oscillator energy $\mu \gg \hbar\omega$. In this limit the wave function can be expressed as

$$\psi(\mathbf{r}, t) = \sqrt{n(\mathbf{r}, t)} e^{i\phi(\mathbf{r},t)} \tag{A.13}$$

where the density[2] n defines the modulus and ϕ the phase. The phase sets the velocity field

$$n(\mathbf{r}, t)\mathbf{v}(\mathbf{r}, t) = \frac{\hbar}{2im}\left(\psi^* \nabla\psi - \psi\nabla\psi^*\right) \tag{A.14}$$

which can subsequently be written as

$$\mathbf{v}(\mathbf{r}, t) = \frac{\hbar}{m}\nabla\phi(\mathbf{r}, t). \tag{A.15}$$

From the GPE A.11 one obtains two equations for the density and velocity, representing the equation of continuity and the other one establishing the irrotational flow respectively. They read

$$\frac{\partial}{\partial t} n + \nabla \cdot (\mathbf{v}n) = 0 \tag{A.16}$$

and

$$m\frac{\partial}{\partial t}\mathbf{v} + \nabla\left(V_{ext} + gn - \frac{\hbar^2}{2m\sqrt{n}}\nabla^2\sqrt{n} + \frac{mv^2}{2}\right) = 0. \tag{A.17}$$

If the repulsive interaction between constituents is strong, the kinetic pressure term can be neglected in the equation for the velocity field

$$m\frac{\partial}{\partial t}\mathbf{v} + \nabla(V_{ext} + gn + \frac{mv^2}{2}) = 0 \tag{A.18}$$

which describes the potential flow of a fluid with equation of state $p = \frac{1}{2}gn^2$. Linearising the continuity equation A.16 and the equation for the potential flow A.18 and combining them yields

$$\frac{\partial^2}{\partial t^2}\delta n = \nabla \cdot (c^2(\mathbf{r})\nabla\delta n) \tag{A.19}$$

[2]In the case of Fermi gases the density referred to here is the molecular density corresponding to half the atomic density.

where c is the local sound velocity with $mc^2(\mathbf{r}) = \partial p/\partial n = \mu - V_{ext}$. In the case of axisymmetric traps ($\omega_z \ll \omega_r$), the above equation can be expanded in the respective trap frequencies

$$m\frac{\partial^2}{\partial t^2}\delta n = \nabla \cdot \left(\left[\mu - \frac{m}{2}(\omega_r^2 r^2 + \omega_z^2 z^2) \right] \nabla \delta n \right). \tag{A.20}$$

For axial symmetry the third component of the angular momentum $\hbar m$ remains a good quantum number but the dispersion law now also depends on the third component of the angular momentum m. The linearised equation A.19 can consequently be rewritten in terms of the respective frequencies resulting in

$$-\omega^2 \delta n = \frac{1}{m}\nabla \cdot \left[n_0 \nabla \left(\frac{\partial \mu}{\partial n}\delta n \right) \right] \tag{A.21}$$

This equation eventually yields a discrete mode structure - the collective modes. In the most general form the density oscillates according to

$$n = n_0 + \delta n \cdot e^{-i\omega t} \tag{A.22}$$

where n_0 denotes the equilibrium density. Since the radial and angular part of density fluctuation δn separate the collective modes can be expressed as a product of the former

$$\delta n \propto r^l Y_{lm}(\theta, \varphi). \tag{A.23}$$

The mode frequencies derived via this approach coincide with the results obtained from the kinetic theory in the hydrodynamic limit. While this theory assumes a macroscopic wave function at zero temperature and the applicability of the Gross-Pitaevskii equation, this restriction is not necessary to derive collective modes in general.

A.4 Additional figures

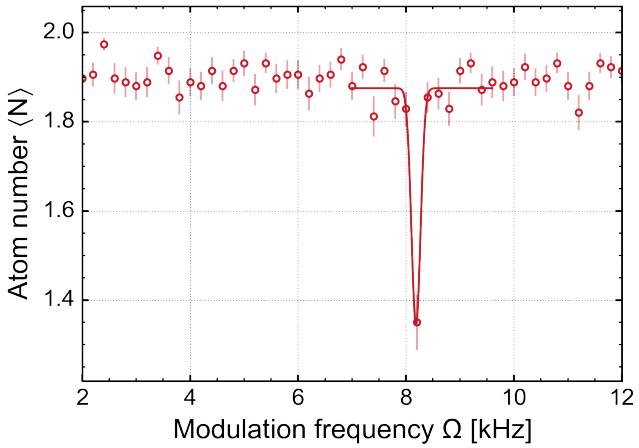

Figure A.2: **Axial trap frequency measurement** The observed resonance at $\Omega = 2\pi \times (8.19 \pm 0.04)$kHz corresponds to the $E_{0\to 2}$ transition in axial direction. The axial trap frequency is hence $\omega_z = \Omega/2 = 2\pi \times (4.09 \pm 0.02)$kHz. The spacing between the lowest and second lowest level might be slightly higher than this value due to the anharmonicity of the Gaussian potential.

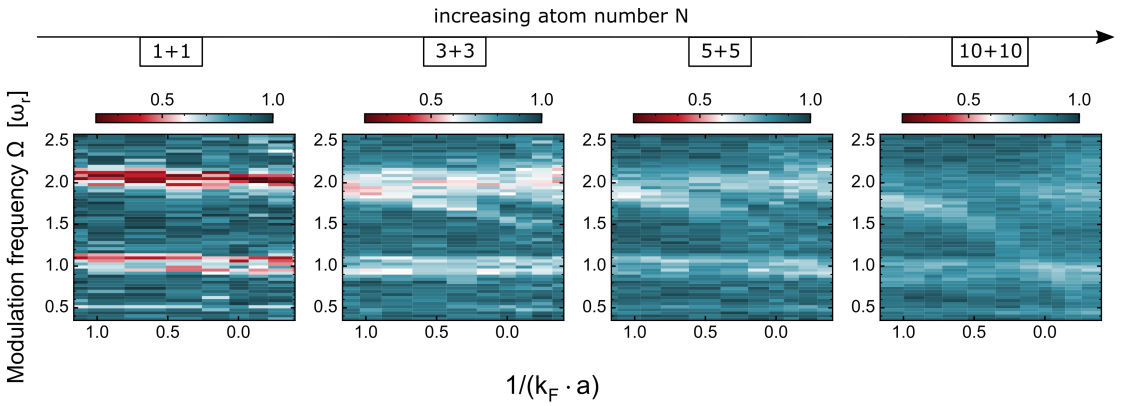

Figure A.3: **Emergence of the quadrupole mode rescaled to the detection probability** This plot is equivalent to figure 4.8 but re-scaled to the detection probability represented by the colour bar. As the number of atoms is increased the relative atom loss is reduced indicating that the perturbation strength explicitly depends on the atom number.

A.5 Full counting statistics

Our small size systems and single-atom resolved counting allows us to investigate the statistical distribution of the atom loss. Concretely, we can count how many times N atoms are lost and derive the respective counting statistics. We refer to the channel N as the channel, where exactly N atoms are lost after the second spilling procedure. Using this technique we can however not resolve where the atom loss occured with respect to the Fermi surface since we are only measuring $\langle \hat{N} \rangle \equiv \sum_i \hat{a}^\dagger \hat{a}_i$ but not the actual occupation of each level. Nevertheless, we can for example distinguish between odd and even atom number loss, where latter could be attributed to the loss of a pair. Figures A.5, A.6 and A.7 show the full number resolved channel loss spectra where the colour directly corresponds to the occurrence. A resonance manifests itself in the full counting statistics as an absence of counts in the "full" channel, representing the initial preparation and increased count number in lower channels. Pictorially atoms are lost from the $N + N$ preparation channel to lower channels where they are counted.

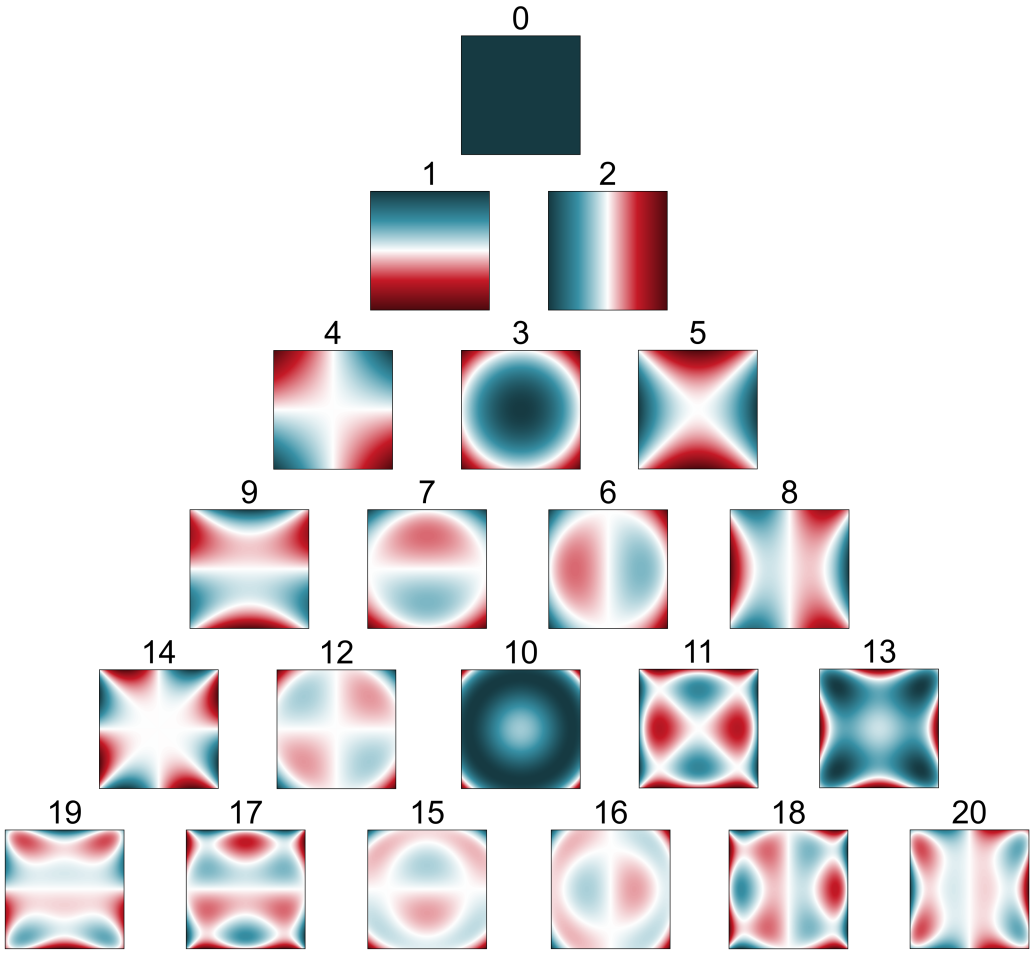

Figure A.4: **Rectangular Zernike polynomials** The lowest 21 rectangular Zernike polynomials are obtained via a gram-schmidt orthonormalisation over the respective grid. The number above each polynomial indicates the Zernike coefficient.

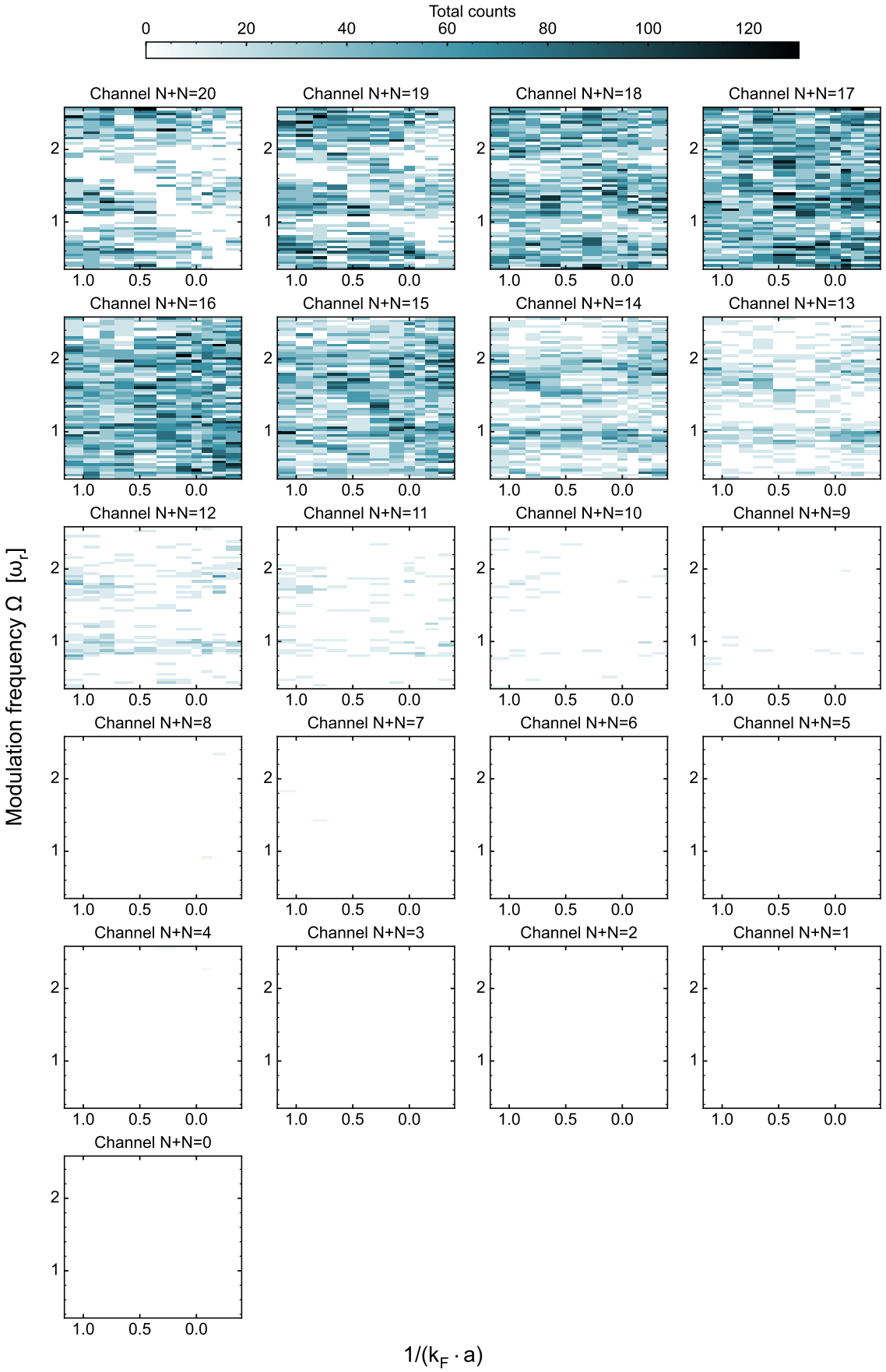

Figure A.5: **Full counting statistics for 10+10 atoms**

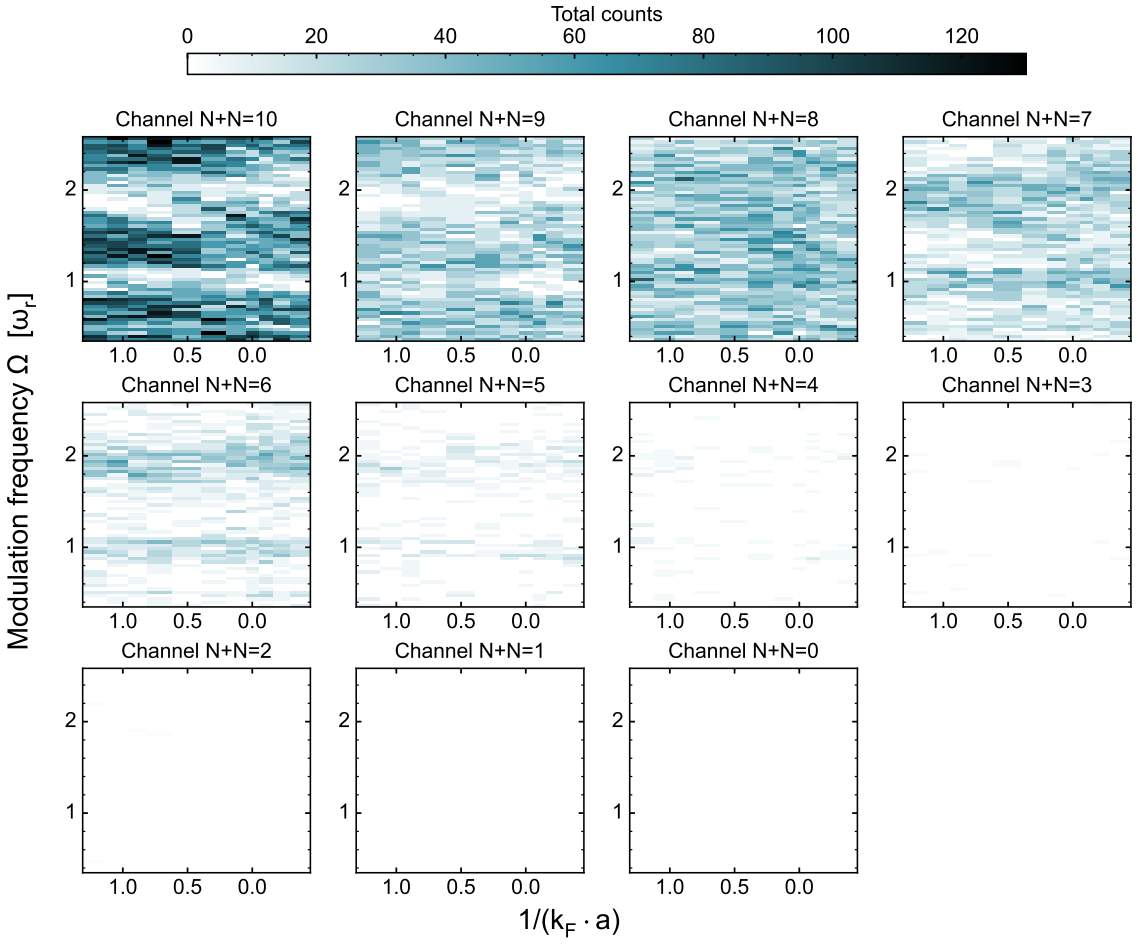

Figure A.6: **Full counting statistics for 5+5 atoms**

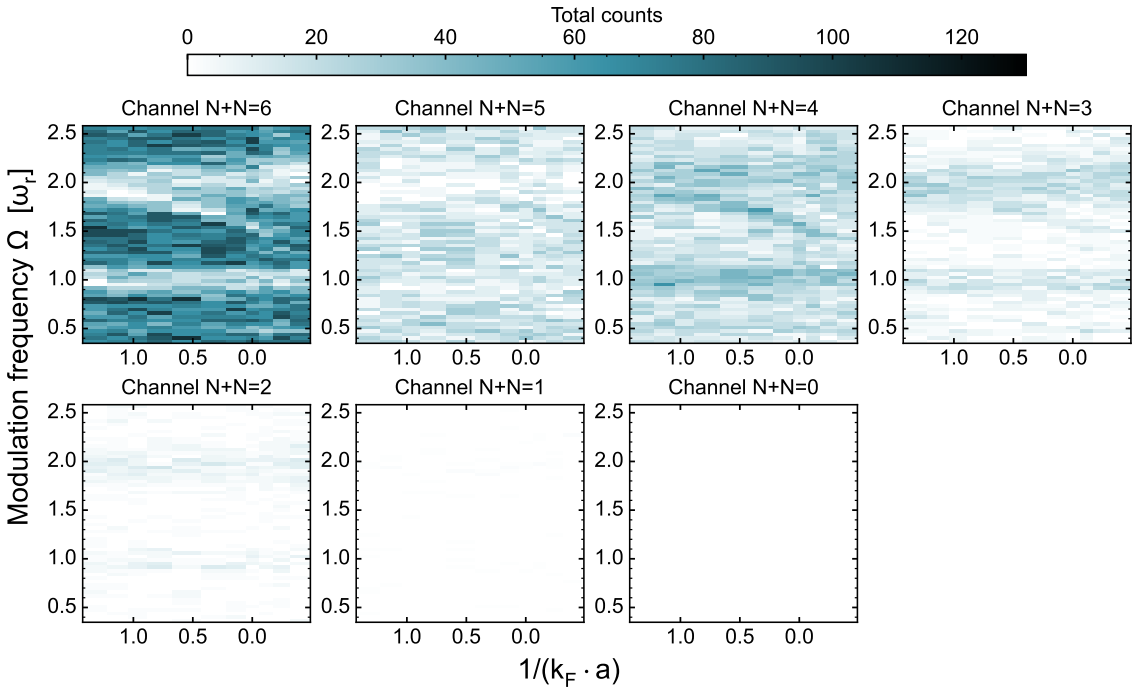

Figure A.7: **Full counting statistics for 3+3 atoms**

B Bibliography

[1] Ben R. Mottelson. Elementary modes of excitation in the nucleus. *Science*, 193(4250): 287–294, 1976. doi: 10.1126/science.193.4250.287. URL https://www.science.org/doi/abs/10.1126/science.193.4250.287.

[2] Slava Grebenev, J Peter Toennies, and Andrei F Vilesov. Superfluidity within a small helium-4 cluster: The microscopic andronikashvili experiment. *Science*, 279 (5359):2083–2086, 1998.

[3] Luca Bayha, Marvin Holten, Ralf Klemt, Keerthan Subramanian, Johannes Bjerlin, Stephanie M Reimann, Georg M Bruun, Philipp M Preiss, and Selim Jochim. Observing the emergence of a quantum phase transition shell by shell. *Nature*, 587 (7835):583–587, 2020.

[4] J. H. Bruning, D. R. Herriott, J. E. Gallagher, D. P. Rosenfeld, A. D. White, and D. J. Brangaccio. Digital wavefront measuring interferometer for testing optical surfaces and lenses. *Appl. Opt.*, 13(11):2693–2703, Nov 1974. doi: 10.1364/AO.13.002693. URL https://opg.optica.org/ao/abstract.cfm?URI=ao-13-11-2693.

[5] Philip Zupancic, Philipp M Preiss, Ruichao Ma, Alexander Lukin, M Eric Tai, Matthew Rispoli, Rajibul Islam, and Markus Greiner. Ultra-precise holographic beam shaping for microscopic quantum control. *Optics express*, 24(13):13881–13893, 2016.

[6] A Altmeyer, S Riedl, MJ Wright, C Kohstall, J Hecker Denschlag, and R Grimm. Dynamics of a strongly interacting fermi gas: The radial quadrupole mode. *Physical Review A*, 76(3):033610, 2007.

[7] L Vichi and S Stringari. Collective oscillations of an interacting trapped fermi gas. *Physical Review A*, 60(6):4734, 1999.

[8] Steven J Portugal, Tatjana Y Hubel, Johannes Fritz, Stefanie Heese, Daniela Trobe, Bernhard Voelkl, Stephen Hailes, Alan M Wilson, and James R Usherwood. Upwash exploitation and downwash avoidance by flap phasing in ibis formation flight. *Nature*, 505(7483):399–402, 2014.

[9] Marcus Woo. How bird flocks are like liquid helium. *Science*, 2014. doi: 10.1126/article.22777.

[10] Andrea Cavagna, Alessio Cimarelli, Irene Giardina, Giorgio Parisi, Raffaele Santagati, Fabio Stefanini, and Massimiliano Viale. Scale-free correlations in starling flocks. *Proceedings of the National Academy of Sciences*, 107(26):11865–11870, 2010.

[11] Jolyon J Faria, Stefan Krause, and Jens Krause. Collective behavior in road crossing pedestrians: the role of social information. *Behavioral ecology*, 21(6):1236–1242, 2010.

[12] Tamas Vicsek. A question of scale. *Nature*, 411(6836):421–421, 2001.

[13] Peter W. Higgs. Broken symmetries and the masses of gauge bosons. *Phys. Rev. Lett.*, 13:508–509, Oct 1964. doi: 10.1103/PhysRevLett.13.508. URL https://link.aps.org/doi/10.1103/PhysRevLett.13.508.

[14] Philip W Anderson. More is different: broken symmetry and the nature of the hierarchical structure of science. *Science*, 177(4047):393–396, 1972.

[15] John Anderson. *Fundamentals of Aerodynamics (SI units)*. McGraw hill, 2011.

[16] Joe J Monaghan. Smoothed particle hydrodynamics. *Annual review of astronomy and astrophysics*, 30(1):543–574, 1992.

[17] K Dolag, F Vazza, Gf Brunetti, and G Tormen. Turbulent gas motions in galaxy cluster simulations: the role of smoothed particle hydrodynamics viscosity. *Monthly Notices of the Royal Astronomical Society*, 364(3):753–772, 2005.

[18] Christopher C Hayward, Paul Torrey, Volker Springel, Lars Hernquist, and Mark Vogelsberger. Galaxy mergers on a moving mesh: a comparison with smoothed particle hydrodynamics. *Monthly Notices of the Royal Astronomical Society*, 442(3): 1992–2016, 2014.

[19] M Gyulassy, KA Frankel, and Horst Stoecker. Do nuclei flow at high energies? *Physics Letters B*, 110(3-4):185–188, 1982.

[20] A.B. Migdal. Superfluidity and the moments of inertia of nuclei. *Nuclear Physics*, 13(5):655–674, 1959. ISSN 0029-5582. doi: https://doi.org/10.1016/0029-5582(59)90264-0. URL https://www.sciencedirect.com/science/article/pii/0029558259902640.

[21] K. W. Madison, F. Chevy, W. Wohlleben, and J. Dalibard. Vortex formation in a stirred bose-einstein condensate. *Phys. Rev. Lett.*, 84:806–809, Jan 2000. doi: 10.1103/PhysRevLett.84.806. URL https://link.aps.org/doi/10.1103/PhysRevLett.84.806.

[22] M. Goldhaber and E. Teller. On nuclear dipole vibrations. *Phys. Rev.*, 74:1046–1049, Nov 1948. doi: 10.1103/PhysRev.74.1046. URL https://link.aps.org/doi/10.1103/PhysRev.74.1046.

[23] Immanuel Bloch, Jean Dalibard, and Sylvain Nascimbene. Quantum simulations with ultracold quantum gases. *Nature Physics*, 8(4):267–276, 2012.

[24] Jonathan Simon, Waseem S Bakr, Ruichao Ma, M Eric Tai, Philipp M Preiss, and Markus Greiner. Quantum simulation of antiferromagnetic spin chains in an optical lattice. *Nature*, 472(7343):307–312, 2011.

[25] John Bardeen, Leon N Cooper, and John Robert Schrieffer. Theory of superconductivity. *Physical review*, 108(5):1175, 1957.

[26] Richard P Feynman. Simulating physics with computers. In *Feynman and computation*, pages 133–153. CRC Press, 2018.

[27] D. S. Jin, J. R. Ensher, M. R. Matthews, C. E. Wieman, and E. A. Cornell. Collective excitations of a bose-einstein condensate in a dilute gas. *Phys. Rev. Lett.*, 77:420–423, Jul 1996. doi: 10.1103/PhysRevLett.77.420. URL https://link.aps.org/doi/10.1103/PhysRevLett.77.420.

[28] O. M. Maragò, S. A. Hopkins, J. Arlt, E. Hodby, G. Hechenblaikner, and C. J. Foot. Observation of the scissors mode and evidence for superfluidity of a trapped bose-einstein condensed gas. *Phys. Rev. Lett.*, 84:2056–2059, Mar 2000. doi: 10.1103/PhysRevLett.84.2056. URL https://link.aps.org/doi/10.1103/PhysRevLett.84.2056.

[29] D Bohle, A Richter, W Steffen, AEL Dieperink, N Lo Iudice, F Palumbo, and O Scholten. New magnetic dipole excitation mode studied in the heavy deformed nucleus 156gd by inelastic electron scattering. *Physics Letters B*, 137(1-2):27–31, 1984.

[30] Sandro Stringari. Collective excitations of a trapped bose-condensed gas. *Physical review letters*, 77(12):2360, 1996.

[31] M Bartenstein, A Altmeyer, S Riedl, S Jochim, C Chin, J Hecker Denschlag, and R Grimm. Collective excitations of a degenerate gas at the bec-bcs crossover. *Physical review letters*, 92(20):203201, 2004.

[32] Wolfgang Ketterle and Martin W Zwierlein. Making, probing and understanding ultracold fermi gases. *La Rivista del Nuovo Cimento*, 31(5):247–422, 2008.

[33] Michael E Gehm. Properties of 6li. *Jetlab,*, 2003.

[34] Wolfgang Demtröder. *Experimentalphysik 3: Atome, Moleküle und Festkörper*. Springer-Verlag, 2016.

[35] Friedhelm Serwane, Gerhard Zürn, Thomas Lompe, TB Ottenstein, AN Wenz, and S Jochim. Deterministic preparation of a tunable few-fermion system. *Science*, 332 (6027):336–338, 2011.

[36] Jun John Sakurai and Eugene D Commins. Modern quantum mechanics, revised edition, 1995.

[37] Marvin Holten. *From Pauli Blocking to Cooper Pairs: Emergence in a Mesoscopic 2D Fermi Gas*. PhD thesis, May 2022. URL http://ultracold.physi.uni-heidelberg.de/files/PhD_2022_Marvin.pdf.

[38] Jan Hendrik Willibald Becher. *Characterizing Few-Fermion Systems with Momentum Correlations*. PhD thesis, May 2020. URL http://archiv.ub.uni-heidelberg.de/volltextserver/28329/1/DissertationJanHendrikBecher.pdf.

[39] Paul Hill. Towards physics of the fractional quantum hall effect in rotating few-fermion systems. Master's thesis, May 2021. URL http://ultracold.physi.uni-heidelberg.de/files/Masterarbeit_2021_Paul.pdf.

[40] Cheng Chin, Rudolf Grimm, Paul Julienne, and Eite Tiesinga. Feshbach resonances in ultracold gases. *Rev. Mod. Phys.*, 82:1225–1286, Apr 2010. doi: 10.1103/RevModPhys.82.1225. URL https://link.aps.org/doi/10.1103/RevModPhys.82.1225.

[41] Gerhard Zürn, Thomas Lompe, Andre Niklas Wenz, Selim Jochim, PS Julienne, and JM Hutson. Precise characterization of li 6 feshbach resonances using trap-sideband-resolved rf spectroscopy of weakly bound molecules. *Physical review letters*, 110(13): 135301, 2013.

[42] Piers Coleman. *Introduction to many-body physics*. Cambridge University Press, 2015.

[43] NN Bogoljubov, Vladimir Veniaminovic Tolmachov, and DV Širkov. A new method in the theory of superconductivity. *Fortschritte der physik*, 6(11-12):605–682, 1958.

[44] Giancarlo Calvanese Strinati, Pierbiagio Pieri, Gerd Röpke, Peter Schuck, and Michael Urban. The bcs–bec crossover: From ultra-cold fermi gases to nuclear systems. *Physics Reports*, 738:1–76, 2018.

[45] DS Petrov, Christophe Salomon, and Gora V Shlyapnikov. Weakly bound dimers of fermionic atoms. *Physical review letters*, 93(9):090404, 2004.

[46] Selim Jochim, Markus Bartenstein, Alexander Altmeyer, Gerhard Hendl, Stefan Riedl, Cheng Chin, J Hecker Denschlag, and Rudolf Grimm. Bose-einstein condensation of molecules. *Science*, 302(5653):2101–2103, 2003.

[47] Marvin Holten, Luca Bayha, Keerthan Subramanian, Carl Heintze, Philipp M Preiss, and Selim Jochim. Observation of pauli crystals. *Physical Review Letters*, 126(2): 020401, 2021.

[48] Marvin Holten, Luca Bayha, Keerthan Subramanian, Sandra Brandstetter, Carl Heintze, Philipp Lunt, Philipp M Preiss, and Selim Jochim. Observation of cooper pairs in a mesoscopic two-dimensional fermi gas. *Nature*, 606(7913):287–291, 2022.

[49] J. H. Becher, E. Sindici, R. Klemt, S. Jochim, A. J. Daley, and P. M. Preiss. Measurement of identical particle entanglement and the influence of antisymmetrization. *Phys. Rev. Lett.*, 125:180402, Oct 2020. doi: 10.1103/PhysRevLett.125.180402. URL https://link.aps.org/doi/10.1103/PhysRevLett.125.180402.

[50] Andrea Bergschneider, Vincent M Klinkhamer, Jan Hendrik Becher, Ralf Klemt, Lukas Palm, Gerhard Zürn, Selim Jochim, and Philipp M Preiss. Experimental characterization of two-particle entanglement through position and momentum correlations. *Nature Physics*, 15(7):640–644, 2019.

[51] Ram-Janik Petzold. Few ultracold fermions in a two-dimensional trap. Master's thesis, 2020. URL http://ultracold.physi.uni-heidelberg.de/files/Masterarbeit_2020_RJPetzold.pdf.

[52] Waseem S Bakr, Jonathon I Gillen, Amy Peng, Simon Fölling, and Markus Greiner. A quantum gas microscope for detecting single atoms in a hubbard-regime optical lattice. *Nature*, 462(7269):74–77, 2009.

[53] Andrea Bergschneider, Vincent M Klinkhamer, Jan Hendrik Becher, Ralf Klemt, Gerhard Zürn, Philipp M Preiss, and Selim Jochim. Spin-resolved single-atom imaging of li 6 in free space. *Physical Review A*, 97(6):063613, 2018.

[54] Joseph W Goodman. *Introduction to Fourier optics*. Roberts and Company publishers, 2005.

[55] Quantum Optics and Computational Imaging Group at Heriot-Watt University. Rectangular zernike polynomials. https://github.com/HWQuantum/Rectangular-Zernike-Polynomials, cloned 11/16/2022.

[56] Martin A Fischler and Robert C Bolles. Random sample consensus: a paradigm for model fitting with applications to image analysis and automated cartography. *Communications of the ACM*, 24(6):381–395, 1981.

[57] Warren J Smith. *Modern optical engineering: the design of optical systems*. McGraw-Hill Education, 2008.

[58] John Ruze. Antenna tolerance theory—a review. *Proceedings of the IEEE*, 54(4): 633–640, 1966.

[59] Germund Dahlquist and Åke Björck. *Numerical methods*. Courier Corporation, 2003.

[60] C.E. Shannon. Communication in the presence of noise. *Proceedings of the IRE*, 37 (1):10–21, 1949. doi: 10.1109/JRPROC.1949.232969.

[61] Harry Nyquist. Certain factors affecting telegraph speed. *Transactions of the American Institute of Electrical Engineers*, 43:412–422, 1924.

[62] John Macnaghten Whittaker. *Interpolatory function theory*. Number 33. Cambridge University Press, 1935.

[63] Stefano Giorgini, Lev P Pitaevskii, and Sandro Stringari. Theory of ultracold atomic fermi gases. *Reviews of Modern Physics*, 80(4):1215, 2008.

[64] DM Stamper-Kurn, H-J Miesner, S Inouye, MR Andrews, and W Ketterle. Collisionless and hydrodynamic excitations of a bose-einstein condensate. *Physical Review Letters*, 81(3):500, 1998.

[65] J Kinast, A Turlapov, and JE Thomas. Breakdown of hydrodynamics in the radial breathing mode of a strongly interacting fermi gas. *Physical Review A*, 70(5):051401, 2004.

[66] MJ Wright, S Riedl, A Altmeyer, C Kohstall, ER Sánchez Guajardo, J Hecker Denschlag, and R Grimm. Finite-temperature collective dynamics of a fermi gas in the bec-bcs crossover. *Physical review letters*, 99(15):150403, 2007.

[67] M. Holten, L. Bayha, A. C. Klein, P. A. Murthy, P. M. Preiss, and S. Jochim. Anomalous breaking of scale invariance in a two-dimensional fermi gas. *Phys. Rev. Lett.*, 121:120401, Sep 2018. doi: 10.1103/PhysRevLett.121.120401. URL https://link.aps.org/doi/10.1103/PhysRevLett.121.120401.

[68] Hauke Biss, Lennart Sobirey, Niclas Luick, Markus Bohlen, Jami J Kinnunen, Georg M Bruun, Thomas Lompe, and Henning Moritz. Excitation spectrum and superfluid gap of an ultracold fermi gas. *Physical Review Letters*, 128(10):100401, 2022.

[69] Lev Davidovich Landau and Evgenii Mikhailovich Lifshitz. *Statistical Physics: Volume 5*, volume 5. Elsevier, 2013.

[70] P Massignan, Georg Morten Bruun, and Henrik Smith. Viscous relaxation and collective oscillations in a trapped fermi gas near the unitarity limit. *Physical Review A*, 71(3):033607, 2005.

[71] S. Riedl, E. R. Sánchez Guajardo, C. Kohstall, A. Altmeyer, M. J. Wright, J. Hecker Denschlag, R. Grimm, G. M. Bruun, and H. Smith. Collective oscillations of a fermi gas in the unitarity limit: Temperature effects and the role of pair correlations. *Phys. Rev. A*, 78:053609, Nov 2008. doi: 10.1103/PhysRevA.78.053609. URL https://link.aps.org/doi/10.1103/PhysRevA.78.053609.

[72] Michael Urban, S Chiacchiera, D Davesne, T Enss, and PA Pantel. Collective modes of three-and two-dimensional trapped fermi gases in the normal phase. In *Journal of Physics: Conference Series*, volume 497, page 012028. IOP Publishing, 2014.

[73] Enrico Lipparini and Sandro Stringari. Sum rules and giant resonances in nuclei. *Physics Reports*, 175(3-4):103–261, 1989.

[74] H. Heiselberg. Collective modes of trapped gases at the bec-bcs crossover. *Phys. Rev. Lett.*, 93:040402, Jul 2004. doi: 10.1103/PhysRevLett.93.040402. URL https://link.aps.org/doi/10.1103/PhysRevLett.93.040402.

[75] Sangyong Jeon and Ulrich Heinz. Introduction to hydrodynamics. *International Journal of Modern Physics E*, 24(10):1530010, 2015.

[76] Krzysztof B Beć, Justyna Grabska, and Thomas S Hofer. Introduction to quantum vibrational spectroscopy. *Near-Infrared Spectroscopy: Theory, Spectral Analysis, Instrumentation, and Applications*, pages 83–110, 2021.

[77] Jun-Jun Liang and Chao Zhang. Two ultracold atoms in a completely anisotropic trap. *Physica Scripta*, 77(2):025302, 2008.

[78] C Menotti, P Pedri, and S Stringari. Expansion of an interacting fermi gas. *Physical review letters*, 89(25):250402, 2002.

[79] MA Baranov and DS Petrov. Low-energy collective excitations in a superfluid trapped fermi gas. *Physical Review A*, 62(4):041601, 2000.

[80] Michael Urban. Radial quadrupole and scissors modes in trapped fermi gases across the bcs phase transition. *Phys. Rev. A*, 78:053619, Nov 2008. doi: 10.1103/PhysRevA.78.053619. URL https://link.aps.org/doi/10.1103/PhysRevA.78.053619.

[81] M. Grasso, E. Khan, and M. Urban. Temperature dependence and finite-size effects in collective modes of superfluid-trapped fermi gases. *Phys. Rev. A*, 72:043617, Oct 2005. doi: 10.1103/PhysRevA.72.043617. URL https://link.aps.org/doi/10.1103/PhysRevA.72.043617.

[82] R. Combescot and X. Leyronas. Hydrodynamic modes in dense trapped ultracold gases. *Phys. Rev. Lett.*, 89:190405, Oct 2002. doi: 10.1103/PhysRevLett.89.190405. URL https://link.aps.org/doi/10.1103/PhysRevLett.89.190405.

[83] Yeong E Kim and Alexander L Zubarev. Time-dependent density-functional theory for trapped strongly interacting fermionic atoms. *Physical Review A*, 70(3):033612, 2004.

[84] Tilman Enss and Keisuke Fujii. Private communication.

[85] Georg Bruun. Private communication.

[86] Lukas Palm. Exploring fractional quantum hall physics using ultracold fermions in rotating traps. Master's thesis, 2018. URL http://ultracold.physi.uni-heidelberg.de/files/Masterarbeit_2018_Lukas.pdf.

[87] Marvin Holten. Collective modes and turbulence in two-dimensional fermi gases. Master's thesis, 2017. URL http://ultracold.physi.uni-heidelberg.de/files/Masterarbeit_2017_Marvin.pdf.

[88] Alexander L Gaunt, Tobias F Schmidutz, Igor Gotlibovych, Robert P Smith, and Zoran Hadzibabic. Bose-einstein condensation of atoms in a uniform potential. *Physical review letters*, 110(20):200406, 2013.

[89] F. Nogrette, H. Labuhn, S. Ravets, D. Barredo, L. Béguin, A. Vernier, T. Lahaye, and A. Browaeys. Single-atom trapping in holographic 2d arrays of microtraps with arbitrary geometries. *Phys. Rev. X*, 4:021034, May 2014. doi: 10.1103/PhysRevX.4.021034. URL https://link.aps.org/doi/10.1103/PhysRevX.4.021034.

[90] Kai-Niklas Schymik, Bruno Ximenez, Etienne Bloch, Davide Dreon, Adrien Signoles, Florence Nogrette, Daniel Barredo, Antoine Browaeys, and Thierry Lahaye. In situ equalization of single-atom loading in large-scale optical tweezer arrays. *Phys. Rev. A*, 106:022611, Aug 2022. doi: 10.1103/PhysRevA.106.022611. URL https://link.aps.org/doi/10.1103/PhysRevA.106.022611.

[91] KM O'hara, SL Hemmer, ME Gehm, SR Granade, and JE Thomas. Observation of a strongly interacting degenerate fermi gas of atoms. *Science*, 298(5601):2179–2182, 2002.

[92] R. Combescot, M. Yu. Kagan, and S. Stringari. Collective mode of homogeneous superfluid fermi gases in the bec-bcs crossover. *Phys. Rev. A*, 74:042717, Oct 2006. doi: 10.1103/PhysRevA.74.042717. URL https://link.aps.org/doi/10.1103/PhysRevA.74.042717.

[93] Andreas Schmitt. Introduction to superfluidity. *Lect. Notes Phys*, 888(1), 2015.

[94] Franco Dalfovo, Stefano Giorgini, Lev P Pitaevskii, and Sandro Stringari. Theory of bose-einstein condensation in trapped gases. *Reviews of modern physics*, 71(3):463, 1999.

[95] LP Pitaevskii. Phenomenological theory of mode collapse-revival in a confined bose gas. *Physics Letters A*, 229(6):406–410, 1997.

[96] F Dalfovo, C Minniti, S Stringari, and L Pitaevskii. Nonlinear dynamics of a bose condensed gas. *Physics Letters A*, 227(3-4):259–264, 1997.

[97] Markus Greiner, Olaf Mandel, Theodor W Hänsch, and Immanuel Bloch. Collapse and revival of the matter wave field of a bose–einstein condensate. *Nature*, 419(6902): 51–54, 2002.

[98] F Dalfovo, C Minniti, and LP Pitaevskii. Frequency shift and mode coupling in the nonlinear dynamics of a bose-condensed gas. *Physical Review A*, 56(6):4855, 1997.

[99] FW Cummings. Stimulated emission of radiation in a single mode. *Physical Review*, 140(4A):A1051, 1965.

[100] T Otsuka, T Abe, T Yoshida, Y Tsunoda, N Shimizu, N Itagaki, Y Utsuno, J Vary, P Maris, and H Ueno. α-clustering in atomic nuclei from first principles with statistical learning and the hoyle state character. *Nature Communications*, 13(1):2234, 2022.

[101] Peter Schuck, Yasuro Funaki, Hisashi Horiuchi, Gerd Röpke, Akihiro Tohsaki, and Taiichi Yamada. Alpha particle clusters and their condensation in nuclear systems. *Physica Scripta*, 91(12):123001, 2016.

[102] T Yamada, Y Funaki, H Horiuchi, G Röpke, P Schuck, and A Tohsaki. Nuclear alpha-particle condensates. In *Clusters in Nuclei, Vol. 2*, pages 229–298. Springer, 2012.

[103] D Guéry-Odelin and S Stringari. Scissors mode and superfluidity of a trapped bose-einstein condensed gas. *Physical review letters*, 83(22):4452, 1999.

[104] J Kinast, A Turlapov, and JE Thomas. Damping of a unitary fermi gas. *Physical review letters*, 94(17):170404, 2005.

[105] Marco Cozzini and Sandro Stringari. Fermi gases in slowly rotating traps: Superfluid versus collisional hydrodynamics. *Physical review letters*, 91(7):070401, 2003.

[106] S Stringari. Collective oscillations of a trapped superfluid fermi gas near a feshbach resonance. *Europhysics Letters*, 65(6):749, 2004.

[107] Joseph Kinast, SL Hemmer, ME Gehm, A Turlapov, and JE Thomas. Evidence for superfluidity in a resonantly interacting fermi gas. *Physical Review Letters*, 92(15): 150402, 2004.

[108] Jamil R Abo-Shaeer, Chandra Raman, Johnny M Vogels, and Wolfgang Ketterle. Observation of vortex lattices in bose-einstein condensates. *Science*, 292(5516):476–479, 2001.

[109] Martin W Zwierlein, Jamil R Abo-Shaeer, Andre Schirotzek, Christian H Schunck, and Wolfgang Ketterle. Vortices and superfluidity in a strongly interacting fermi gas. *Nature*, 435(7045):1047–1051, 2005.

[110] Kurt Roth. Fundamentals of environmental physics (lecture notes v0.4-p), 2016.

[111] Martin W Zwierlein. *High-temperature superfluidity in an ultracold Fermi gas*. PhD thesis, Massachusetts Institute of Technology, 2006.

[112] Franco Dalfovo, S Giorgini, Montserrat Guilleumas, L Pitaevskii, and S Stringari. Collective and single-particle excitations of a trapped bose gas. *Physical Review A*, 56(5):3840, 1997.

[113] Puneet A Murthy and Selim Jochim. Direct imaging of the order parameter of an atomic superfluid using matterwave optics. *arXiv preprint arXiv:1911.10824*, 2019.

[114] P. A. Murthy, D. Kedar, T. Lompe, M. Neidig, M. G. Ries, A. N. Wenz, G. Zürn, and S. Jochim. Matter-wave fourier optics with a strongly interacting two-dimensional fermi gas. *Phys. Rev. A*, 90:043611, Oct 2014. doi: 10.1103/PhysRevA.90.043611. URL https://link.aps.org/doi/10.1103/PhysRevA.90.043611.

[115] Luca Asteria, Henrik P Zahn, Marcel N Kosch, Klaus Sengstock, and Christof Weitenberg. Quantum gas magnifier for sub-lattice-resolved imaging of 3d quantum systems. *Nature*, 599(7886):571–575, 2021.

[116] Frédéric Chevy, KW Madison, and Jean Dalibard. Measurement of the angular momentum of a rotating bose-einstein condensate. *Physical Review Letters*, 85(11): 2223, 2000.

[117] Francesca Zambelli and Sandro Stringari. Quantized vortices and collective oscillations of a trapped bose-einstein condensate. *Phys. Rev. Lett.*, 81:1754–1757, Aug 1998. doi: 10.1103/PhysRevLett.81.1754. URL https://link.aps.org/doi/10.1103/PhysRevLett.81.1754.

[118] GM Bruun and L Viverit. Vortex state in superfluid trapped fermi gases at zero temperature. *Physical Review A*, 64(6):063606, 2001.

[119] A Del Campo, A Retzker, and Martin B Plenio. The inhomogeneous kibble–zurek mechanism: vortex nucleation during bose–einstein condensation. *New Journal of Physics*, 13(8):083022, 2011.

[120] Giacomo Lamporesi, Simone Donadello, Simone Serafini, Franco Dalfovo, and Gabriele Ferrari. Spontaneous creation of kibble–zurek solitons in a bose–einstein condensate. *Nature Physics*, 9(10):656–660, 2013.

[121] Zoran Hadzibabic, Peter Krüger, Marc Cheneau, Baptiste Battelier, and Jean Dalibard. Berezinskii–kosterlitz–thouless crossover in a trapped atomic gas. *Nature*, 441(7097):1118–1121, 2006.

[122] D Dagnino, N Barberán, M Lewenstein, and J Dalibard. Vortex nucleation as a case study of symmetry breaking in quantum systems. *Nature Physics*, 5(6):431–437, 2009.

[123] Lukas Palm, Fabian Grusdt, and Philipp M Preiss. Skyrmion ground states of rapidly rotating few-fermion systems. *New Journal of Physics*, 22(8):083037, 2020.

Danksagung

Zuallererst möchte ich mich bei Selim bedanken - für die hervorragende Betreuung der Masterarbeit, die zahlreichen Inspirationen und Ideen, aber auch für die vielen hilfreichen Gedankenanstöße. De plus, je tiens à remercier Lauriane pour la deuxième correction de ce travail de master.

Ein ganz besonderer Dank geht an Paul und Philipp, mit denen ich die Ehre und vor allem Freude hatte, in den letzten Monaten am *Alten Experiment* zusammenzuarbeiten. Ohne eure Unterstützung wäre dieses Projekt sicherlich nicht möglich gewesen. Nicht nur habt ihr durch die Beantwortung gefühlt hunderttausender Fragen mein Wissen erweitert, sondern vor allem auch durch eure experimentelle Erfahrung und theoretische Expertise maßgeblich zu den gewonnenen Erkenntnissen beigetragen und dieses Projekt überhaupt erst möglich gemacht. So hoffe ich, dass wir die beiden begonnenen Projekte, den PSI Algorithmus auf den Atomen und die kollektiven Moden gemeinsam zu einem schönen Abschluss führen können.

Des Weiteren möchte ich der gesamten Ultracoldgruppe für die hervorragende Gesellschaft, die kritischen Fragen an der richtigen Stelle und die inhaltliche Unterstützung danken. Ein besonderer Dank geht auch an diejenigen, die dieses Manuskript Korrektur gelesen haben.

Nichtzuletzt möchte ich meiner Familie und meinen Freunden für die immerwährende Unterstützung danken, die sie mir bei all meinen Projekten entgegenbringen.

Erklärung - Declaration of authorship

Ich versichere, dass ich diese Arbeit selbstständig verfasst habe und keine anderen, als die angegebenen Quellen und Hilfsmittel benutzt habe.

I hereby declare that the thesis submitted is my own unaided work. All direct or indirect sources used are acknowledged as references.

Heidelberg, den 28.02.2023